AN EVALUATION OF THE POTENTIAL OF COASTAL WETLANDS FOR HURRICANE SURGE AND WAVE ENERGY REDUCTION

A Thesis

by

NICHOLAS MASON LODER

Submitted to the Office of Graduate Studies of
Texas A&M University
in partial fulfillment of the requirements for the degree of

MASTER OF SCIENCE

December 2008

Major Subject: Civil Engineering

AN EVALUATION OF THE POTENTIAL OF COASTAL WETLANDS FOR HURRICANE SURGE AND WAVE ENERGY REDUCTION

A Thesis

by

NICHOLAS MASON LODER

Submitted to the Office of Graduate Studies of
Texas A&M University
in partial fulfillment of the requirements for the degree of

MASTER OF SCIENCE

Approved by:

Chair of Committee,	Jennifer L. Irish
Committee Members,	Billy L. Edge
	Alejandro H. Orsi
Head of Department,	David V. Rosowsky

December 2008

Major Subject: Civil Engineering

ABSTRACT

An Evaluation of the Potential of Coastal Wetlands for Hurricane Surge and Wave Energy Reduction. (December 2008)

Nicholas Mason Loder, B.S., Clemson University

Chair of Advisory Committee: Dr. Jennifer L. Irish

Given the past history and future risk of storm surge in the United States, alternative storm protection techniques are needed to protect vital sectors of the economy and population, particularly within southeastern Louisiana. It is widely hypothesized that coastal wetlands offer protection from storm surge and wave action, though the extent of this protection is unknown due to the complex physics behind vegetated flow dynamics. This thesis presents numerical modeling results that estimate the relative sensitivity of waves and storm surge to characteristics embodied by coastal wetlands. An idealized grid domain and 400 km^2 (20 km by 20 km) marsh feature provide a controlled environment for evaluating marsh characteristics, including bottom friction, elevation, and continuity. Marsh continuity is defined as the ratio of healthy marsh area to open water area within the total wetland area.

It is determined that increased bottom friction reduces storm surge levels and wave heights. Through the roughening of the bottom from sandy to covered with tall grass, it is estimated that waves may be dampened by up to 1.2 m at the coast, and peak surge may be reduced by as much as 35%. The lowering of marsh elevation generally

increases wave heights and decreases surge levels, as expected. A 3.5 m decrease in marsh elevation results in as much as a 2.6 m increase in wave height, and up to a 15% decrease in surge levels. Reductions in marsh continuity enhance surge conveyance into and out of the marsh. For storms of low surge potential, surge is increased by as much as 70% at the coast due to decreasing marsh continuity from 100% to 50%, while for storms of high surge potential, surge is decreased by 5%. This indicates that for storms of high surge potential, a segmented marsh may offer comparable surge protection to that of a continuous marsh. Wave heights are generally increased within the marsh due to the transmission of wave energy through marsh channels. Results presented in this thesis may assist in the justification of coastal wetland mitigation, and optimize marsh restoration in terms of providing maximum storm protection.

ACKNOWLEDGEMENTS

Above all, I extend my deepest thanks to my advisor, Dr. Jennifer Irish. From the beginning of my graduate studies, she has provided me with endless opportunities, significantly contributing to my academic and professional development. Her insight, kindness, and contagious enthusiasm have truly inspired me in a way that I will never forget. I would also like to thank my thesis committee members, Dr. Billy Edge and Dr. Alejandro Orsi, for their time and contributions in reviewing this work. I am very grateful to Ty Wamsley and the US Army Engineer Research and Development Center (ERDC) for allowing me to work on this exciting project. I would like to extend a special thanks to Mary Cialone (ERDC) for all the guidance and moral support she has given me during this project and my time in Vicksburg, MS. I would also like to thank Alison Sleath (ERDC), Dr. Jane Smith (ERDC), Tate McAlpin (ERDC), Dr. Robert Jensen (ERDC), and Al Cialone (ERDC) for their individual contributions to this research. I would like to thank Dr. Jim Kaihatu and Dr. Billy Edge for their help in my decision to attend Texas A&M University. I extend sincere thanks to the Barrett and Margaret Hindes Foundation and Mrs. Silvana Jelesnianski for their generous contributions toward my graduate education. In addition, I thank all of my fellow graduate students and friends at Texas A&M for their love and support during the past two years. Finally, I want to thank my family for all of the prayers and love they have provided for me during my life. Without you, none of this would be possible.

NOMENCLATURE

ADCIRC	Advanced Circulation Model
$\vec{B}$	Baroclinic pressure gradient
B	Dimensionless energy parameter
B_f	ADCIRC bottom friction coefficient
b_y	Y-intercept
c	Marsh continuity
C_d	Garratt's drag coefficient
C_D	Drag coefficient
CEST	Coastal and Estuarine Storm Tide Model
C_f	Dimensionless friction coefficient
C_{gr}	Group wave celerity
C_r	Wave celerity
cm	Centimeters
C_m	Mean wave celerity
C_p	Minimum central pressure
$\vec{D}$	Momentum dispersion
D	Dimensionless energy dissipation parameter
d	Stem diameter
E	Energy
EPA	Environmental Protection Agency

ERDC	US Army Engineer Research and Development Center
E_{tot}	Total energy within wave spectrum
f	Darcy-Weisbach bottom friction factor
f_c	Coriolis parameter
f_p	Spectral peak
F_{in}	Energy flux from wind to waves
FEMA	Federal Emergency Management Agency
FVCOM	Finite-volume Coastal Ocean Model
g	Gravitational acceleration
GWCE	Generalized Wave Continuity Equation
Ghz	Gigahertz
h	Total depth
H	Wave height
H_0	Incident wave height
$H_{m0,max}$	Zero-moment energy-based wave height
H_s	Significant wave height
H_{base}	Average peak significant wave height within marsh for base case
$\hat{k}$	Vertical unit vector
k	Wave number
K	Non-dimensional roughness coefficient
k_i	Exponential decay coefficient
k_p	Wave number at spectrum peak

km/h	Kilometers per hour
kts	Knots
km	Kilometers
L	Wavelength
l_s	Stem length
$\vec{M}$	Lateral stress
M	Characteristic dimensionless surge function
m	Meters
m/s	Meters per second
mb	Millibars
mm	Millimeters
MPI	Message passing interface
MPP	Massively paralleled processor
MSRC	Major Shared Resource Center
n	Manning's coefficient of friction
N	Number of vegetation elements per horizontal area
NCFS	North Carolina Forecast System
NOAA	National Oceanic and Atmospheric Administration
NWS	National Weather Service
P	Atmospheric pressure
PBL	Planetary Boundary Layer Model
R^2	Coefficient of determination

RAM	Random access memory
R_p	Pressure radius
s	Plant spacing
S	Sheltering coefficient
S_0	Slope of water surface
S_{bf}	Energy loss in wave spectrum due to bottom friction
SLOSH	Sea, Lake, and Overland Surge from Hurricane Model
SMS	Surface Water Modeling System
STWAVE	Steady State Spectral Wave Model
SWAN	Simulating Waves Nearshore Model
S_{ij}	Radiation stress tensor
t	Time
$\bar{u}$	Depth-averaged horizontal velocity
u_*	Friction velocity
U	Horizontal velocity component in x-direction
UnTrim	Unstructured Tidal, Residual, Intertidal Mudflat Model
U_R	Ursell parameter
u_{rms}	Root-mean-square of bottom velocity
USACE	United States Army Corps of Engineers
USDA	United States Department of Agriculture
USGS	United States Geological Survey
V	Horizontal velocity component in y-direction

W	Wind speed at the water surface
W_{10}	Wind speed at 10 meters above water surface
$W_{10,x}$	Wind speed at 10 meters above surface in x-direction
$W_{10,y}$	Wind speed at 10 meters above surface in y-direction
WAM	Wave Prediction Model
x	Horizontal length perpendicular to y-direction
y	Horizontal length perpendicular to x-direction
z	Marsh elevation
α	Wave direction in reference to wave crest
δ	Current direction in relation to a static reference frame
δ_v	Vegetation diameter
ε	Coefficient related to energy transfer due to wave breaking
Δp	Barometric pressure gradient
ϕ	Degrees latitude
Γ_g	Wave energy flux
γ	Specific weight of water
λ	Degrees longitude
κ	Wave breaking index
Λ	Percentage of momentum transfer from atmosphere to water
μ	Direction of wave propagation
η	Equilibrium tide potential

ρ_a	Air density
ρ_w	Water density
τ_*	Bottom friction
τ_b	Shear stress at bottom
τ_s	Shear stress at water surface
τ_w	Wave radiation stress
τ_{si}	Water surface stress tensor
ω	Angular frequency
ω_a	Angular frequency in respect to a static reference frame
ω_r	Angular frequency in respect to wave crest
ψ	Effective earth elasticity factor
ζ	Setup of water surface due to storm surge
$\bar{\varsigma}$	Mean water level
ζ_B	Setup of water surface due to barometric pressure gradient
ζ_{base}	Average peak surge within marsh for base case

TABLE OF CONTENTS

Page

LIST OF FIGURES

FIGURE Page

FIGURE Page

LIST OF TABLES

1. INTRODUCTION: STORM SURGE AND COASTAL WETLANDS

1.1 The Hazard of Hurricane Storm Surge

In terms of both life and property, hurricanes remain the dominant form of natural disaster occurring on American soil, accounting for seven of the ten deadliest natural disasters in United States history (*Tanner*, 2005). The Galveston Hurricane of 1900 was responsible for an estimated 8,000 fatalities, primarily as a result of storm surge (*Potter*, 2004). Eight hurricanes and one tropical storm are listed in the ten most costly (in terms of federal aid) forms of natural disaster to strike the US since the establishment of the Federal Emergency Management Agency in 1979 (*FEMA*, 2008). In August 2005, Hurricane Katrina became the most costly and third most deadly hurricane in US history, resulting in over 1800 deaths (*Knabb et al.*, 2005) and over $80 billion in damages along the coast of the Gulf of Mexico (*Otten et al.*, 2006).

The principal mechanisms of hazard associated with hurricanes are wind, storm surge, and extreme rainfall. Storm surge has historically been a principle danger to life and property associated with hurricanes (*US NOAA*, 2008). Ninety percent of hurricane-related deaths were caused by storm surge prior to 1970 (*Otten et al.*, 2006). Despite technological advances in early warning and forecast systems, storm surge continues to be a major player in the arsenal of hurricane-related hazards. The vast majority of fatalities incurred by Hurricane Katrina were a direct result of storm surge. Regardless of improvements in forecasting and communication, storm surge poses an unyielding

---

This thesis follows the style of the *Journal of Geophysical Research.*

threat to industry and infrastructure. Flooding due to storm surge significantly impacted the tourism industry in New Orleans in the months after Hurricane Katrina, resulting in lost jobs and severely diminished tax revenues. Across the United States, the oil and gas industry was impacted by Hurricane Katrina, as storm surge waters damaged numerous oil refineries along the coast of Louisiana, Mississippi, and Alabama (*Knabb et al*., 2005).

Coastal areas of the United States particularly prone to hurricane storm surge are located along the Gulf of Mexico and Atlantic Ocean. A mildly sloping continental shelf elevates the risk due to storm surge. Approaching hurricanes tend to raise water levels through decreased atmospheric pressure and powerful sustained winds. The magnitude of surge is inversely related to local water depth, via the momentum balance. For this reason, storm surge levels along the coast are dependent upon the characteristics of local bathymetry, with areas of steeply sloping bathymetry less prone to surge than areas of mildly sloping bathymetry.

1.2 Potential Benefit of Wetlands for Surge and Wave Energy Reduction

From a coastal engineering perspective, little can be done to completely eliminate storm surge as a coastal hazard. Recent history has proven that despite even the most complex system of levees and hydraulic structures, storm surge will relentlessly sustain damage upon coastal properties. With 43% of the US population living in coastal areas (*Martinez et al.*, 2007), it is worthwhile to investigate alternative methods to accompany hard structures as a form of storm surge protection. Coastal wetlands, referred to by some as “horizontal levees” (*Houck*, 2006), may be a promising form of

hazard mitigation to alleviate storm surge levels placed on coastal structures. Other sources state that while wetlands may slow the propagation of surge to an inland area, their relative efficiency at reducing storm surge levels is dependent upon the characteristics of the incident storm (*Resio and Westerink*, 2008).

It is of general belief that coastal wetlands have the ability to reduce storm damage through wave dissipation and increased drag due to vegetation. While there exists a moderate body of literature regarding the reduction of hurricane wave heights due to vegetation, there is a comparatively limited number of publications regarding the ability of a coastal wetland to reduce storm surge propagation on a large-scale. Due to global sea level rise, erosion, land subsidence, and human activities, coastal wetlands have become increasingly exploited. A 33 mm decrease in marsh elevation was observed as a result of the compression forces induced by storm surge waters from Hurricane Andrew on certain salt marshes in Louisiana (*Cahoon et al.*, 2006). Within Louisiana, an estimated 64 km^2 of wetlands is lost each year, a rate that will expose key hurricane protection levees and oil industry infrastructure to open-water conditions by the year 2050 (*Otten*, 2006). In order to evaluate coastal wetlands in terms of storm protection, this thesis presents the use of numerical modeling to estimate the storm surge reduction capabilities associated with characteristic qualities of coastal marsh.

1.3 Thesis Content

This thesis is comprised of five sections. Section 1 identifies the threat imposed by storm surge on an increasingly dense US coastal population, and suggests the soft engineering technique of marsh restoration as a coastal protection measure utilized in

conjunction with hard engineering structures. The second section presents an overview of the existing body of research relating to the use of coastal wetlands for the purpose of reducing storm surge, as well as a review of literature relating to storm surge modeling, wetland loss, and marsh restoration techniques. The third section details the numerical simulation methods used in this study, along with the numerical model setup of each scenario of varying bottom friction, seabed elevation, and marsh continuity. Section 4 discusses the results of the wave and surge simulations focusing on bottom friction, elevation, and marsh continuity. Conclusions and recommendations for further research are included in Section 5.

2. BACKGROUND AND LITERATURE REVIEW

2.1 Introduction

Flow resistance imparted by vegetation is three-dimensional, and governed by more complex processes than that arising from the bottom boundary layer (*Reid and Whitaker*, 1976; *Kouwen et al*., 1981; *Kadlec*, 1990; *Peterson et al.*, 2004; *Green*, 2005;). *Green* (2005) categorizes vegetative resistance into 1) energy loss at the bottom of the water column due to bottom friction and 2) drag throughout the water column. Drag is dominant in the case of vegetative flow, as the velocities within a vegetated canopy are greatly reduced and flow tends to be diverted around areas of dense growth (*Green*, 2005). *Peterson et al.* (2004) found through laboratory measurements that the velocities within a vegetative canopy are inversely proportional the square root of vegetation density. *Danard and Murty* (1994) considered the flow regime to be dependent upon plant height and depth of flow. Despite these findings that vegetated flow is a three-dimensional problem, impacts of vegetation on flow are often limited to the use of a bottom friction term, as the case in this research study.

To provide a basis for investigating coastal wetlands with respect to storm protection, coastal wetlands, storm surge, and gravity water waves are examined in this section. The discussion begins with an overview of the physics and pertinent governing equations behind storm surge (Section 2.2) and water waves (Section 2.3). As this thesis relies heavily on numerical model results, Section 2.4 provides an overview of storm surge models currently in use. Relevant to modeling flow through wetlands is vegetated flow dynamics. This is discussed in Section 2.5 with respect to empirical equations

derived to describe open channel flow, followed by a survey of how vegetated drag is included in various storm surge models. Mechanisms potentially providing wave energy and storm surge attenuation in coastal wetlands are presented in Section 2.6. An overview of coastal wetlands in terms of benefits, wetland loss, and restoration is provided through Sections 2.7, 2.8, and 2.9. Section 2.10 provides a summary of reviewed literature and background information in context to the research presented in this thesis.

2.2 Governing Equations for Storm Surge

Before wetland parameters that reduce storm surge may be investigated, it is necessary to outline the equations governing equations driving nearshore circulation. As stated in Section 2.1, vegetated flow is a three-dimensional problem, often approximated by two-dimensional models. Further approximations are induced through the assumption of a constant-density fluid. In this study, vegetation is accounted for in increased bottom friction, and flow is approximated through a two-dimensional model. Therefore, this section describes the two-dimensional governing equations for storm surge. Conservation of mass yields

$$\frac{\partial h}{\partial t} + \nabla_h (h\vec{u}) = 0 \tag{2.1}$$

where h is total depth, and $\vec{u}$ is the depth-averaged horizontal velocity. Taking into account the forces associated with storm surge, two-dimensional depth-averaged conservation of momentum is dictated by:

$$\frac{\partial \vec{u}}{\partial t} + (\vec{u} \cdot \nabla_h)\vec{u} = -g\nabla_h(\zeta + \frac{P}{g\rho_w} - \psi\eta) + f_c \hat{k} \times \vec{u} + \frac{\tau_s}{h\rho_w} - \frac{\tau_b}{h\rho_w} + \frac{\tau_w}{h\rho_w} + \frac{\vec{M}}{h} - \frac{\vec{D}}{h} - \frac{\vec{B}}{h} \tag{2.2}$$

where g is gravitational acceleration, P is atmospheric pressure, ρ_w is water density, ψ is the effective earth elasticity factor, η is equilibrium tide potential, f_c is the Coriolis parameter, $\hat{k}$ represents the vertical unit vector, τ_s is the free-surface stress imposed by wind forcing, τ_b is bottom stress, τ_w is wave radiation stress, $\vec{M}$ is lateral stress, $\vec{D}$ is momentum dispersion, and $\vec{B}$ is the baroclinic pressure gradient. The lateral stress, momentum dispersion, and baroclinic pressure are added for numerical averaging in space and time. Neglecting tidal forces, variations in fluid density, and reducing the momentum conservation to the dominant forces in storm surge, Equation 2.2 becomes:

$$\frac{\partial \vec{u}}{\partial t} + (\vec{u} \cdot \nabla_h)\vec{u} = -g\nabla_h(\zeta + \frac{P}{g\rho_w}) + f\hat{k} \times \vec{u} + \frac{\tau_s}{h\rho_w} - \frac{\tau_b}{h\rho_w} + \frac{\vec{M}}{h} - \frac{\vec{D}}{h} \qquad (2.3)$$

Factors dominating the displacement of the free-surface may therefore be identified as wind stress, atmospheric pressure gradient, Coriolis force, bottom stress, and momentum dispersion.

The dominant factor governing the setup of water levels in hurricane conditions is the forcing imparted by wind, or wind stress. Wind stress is a function of air density, wind speed, and a surface friction coefficient, and is empirically defined as

$$\tau_s = \rho_a C_f W^2 \qquad (2.4)$$

where C_f is a dimensionless friction coefficient, and W is wind speed at the water surface (*Dean and Dalyrmple*, 2002). As wind speed is increased, the water surface forms an upward slope in the direction of the wind. This results in a greater hydrostatic force along the downwind side of the water column than the upwind side, resulting in a

return flow at the bottom. Governed in part by bottom friction, the return flow is reduced, resulting in a buildup of water along the downwind side of the water column.

Hurricanes and extratropical storms tend to be characterized by a sharp barometric pressure gradient. This gradient, when imposed on a large body of water, may induce a setup of water focused in areas of extreme low atmospheric pressure. This mechanism is a secondary component of storm surge. Typically, barometric setup is on the scale of less than a meter, considerably less than the setup induced by wind stress. The barometric pressure component of storm surge may be estimated by

$$\zeta_B = \frac{\Delta p}{\gamma} \tag{2.5}$$

where ζ_B is the setup due to barometric pressure gradient, Δp is the pressure deficit, and γ is the specific weight of water. In short, the setup due to barometric pressure gradient may be estimated by

$$\zeta_B = 1.04\Delta p \tag{2.6}$$

where ζ_B is measured in centimeters, and Δp is measured in millibars (*Dean and Dalyrmple*, 2002).

A more subtle component affecting the total storm surge setup is the Coriolis setup. Longshore currents are induced by cyclonic winds traversing about a low pressure system in a counterclockwise fashion. As currents flow over long distances in the Northern hemisphere, the Coriolis acceleration will result in a right-hand deflection. At the onset of the storm, as currents traverse along the shoreline with land situated to the right, a coastal setup of water will be observed as these currents are deflected

landward due to Coriolis acceleration. This component of storm surge may similarly decrease shoreward water levels when currents are flowing in the opposite direction, after a storm makes landfall.

2.3 Governing Equations for Waves

Assuming a fluid of constant density, a derivation of the governing equations of linear water waves begins with the continuity equation, as shown in Equation 2.1. Assuming a linear wave, the water surface position (ζ) is dependent upon wave height (*H*), angular frequency (ω), wave number (*k*) and time (*t*):

$$\zeta = \frac{H}{2}\cos\theta \qquad \theta = kx - \omega t \tag{2.7}$$

Kinetic wave energy per unit width along a wave crest (*E*) is given:

$$E = \frac{1}{16}\rho_w g H^2 \tag{2.8}$$

The energy balance for waves is given (*Svendsen*, 2006):

$$\frac{\partial H}{\partial x} + \left(\frac{1}{c}\frac{\partial c}{\partial x} + \frac{1}{B}\frac{\partial B}{\partial x}\right)\frac{H}{2} = \frac{D}{8hLB}H^2 \tag{2.9}$$

where *c* is wave celerity, *B* is a dimensionless energy parameter, *D* is a dimensionless energy dissipation parameter, and *L* is wavelength. Cross-shore momentum (x-direction) balance is given:

$$0 = -\rho_w g h\frac{\partial \zeta}{\partial x} + \frac{\partial}{\partial x}\left(-S_{xx} + \overline{\int_{-h}^{\zeta}\tau_{xx}\partial z}\right) - \tau_{bx} \tag{2.10}$$

where S_{xx} is radiation stress, τ_{xx} is normal stress on the vertical surfaces, and τ_{bx} is bottom stress. As waves propagate, wave energy is conserved assuming no energy loss

occurs due to effects such as vegetation. In this study, vegetation effects will be included in the bottom friction term. As waves propagate from deep water to shallow water, several transformations may occur, including wave refraction and shoaling. Conservation of energy leads to wave height increases with decreasing wave celerity (shoaling). Further, as waves converge (decreased width between wave rays), an increase in wave height is expected (refraction).

A setup in the still water surface due to wave breaking is known as wave setup. This effect occurs within the surf zone, as breaking waves transfer momentum to the water column. Wave setup is dependent upon both breaking wave height and bottom slope, and is at a maximum along the coast. A force balance, assuming no variations in the longshore direction and shore-normal waves, yields

$$\frac{\partial \bar{\zeta}}{\partial x} = -\frac{1}{\rho_w g(h+\bar{\zeta})}\frac{\partial S_{xx}}{\partial x} \tag{2.11}$$

where $\bar{\zeta}$ is the mean water level. For linear waves in shallow water, radiation stress may be defined as

$$S_{xx} = \frac{3}{16}\rho_w g \kappa^2 (h+\bar{\zeta})^2 \tag{2.12}$$

where κ is the breaking index. Wave setup is accompanied by wave setdown in areas seaward of wave breaking, as the slope of the water surface counteracts the energy flux due to wave dissipation.

2.4 Modeling Storm Surge

Several numerical models have been constructed for the forecast and risk assessment of hurricane storm surge. In the 1980's, the US National Weather Service

(NWS) developed the Sea, Lake, and Overland Surge from Hurricane (SLOSH) model for the purpose of forecasting hurricane storm surge in advance of approaching tropical storms (*Zhang et al.*, 2008; *Jelesnianski et al*., 1992). While forecasting for emergency response in the U.S. is primarily done by the SLOSH model, numerous other hydrodynamic models exist for the local risk analysis of hurricane storm surge. Among these are the Advanced Circulation Model (ADCIRC), Delft3D model, Coastal and Estuarine Storm Tide model (CEST), Finite-volume Coastal Ocean Model (FVCOM), Unstructured Tidal, Residual, Intertidal Mudflat (UnTRIM) Model, and the MIKE 21 model. These models generally provide a higher spatial resolution and include more of the relevant physics than previous models. ADCIRC is currently utilized by the US Army Corps of Engineers and FEMA in the analysis of hurricane storm surge risk and analysis of proposed storm protection plans across the nation. In this form of analysis, the ADCIRC model is implemented as a two-dimensional, depth-integrated hydrodynamic model that solves the momentum and mass conservation equations in spherical coordinates (latitude/longitude). The model may be forced by wind and pressure fields, tidal constituents, wave radiation stress (as output from a wave model), and user-specified boundary conditions (such as river inputs and overtopping levees). A spatially detailed grid is utilized by USACE in the assessment of hurricane surge for risk analysis. Validation studies indicate that in the hindcasting of Hurricanes Betsy (1965) and Andrew (1992), the ADCIRC model is capable of computing peak surge elevations to a mean error of +/-0.3 m (*Westerink et al*., 2008). The ADCIRC model is also utilized at the state level. For example, the State of North Carolina forecasts hurricane storm

surge levels for the purpose of emergency management, evacuation planning, and resource deployment using ADCIRC (*Mattocks and Forbes*, 2008). As implemented in the North Carolina Forecast System (NCFS), peak water elevation results from the ADCIRC model were compared with NOAA tidal stations. This analysis indicated that ADCIRC was able to hindcast peak water levels to an accuracy of between -4% and -16% (*Mattocks and Forbes*, 2008). In low-resolution areas of the finite-element grid mesh, greater fractional errors were indicated (*Mattocks and Forbes*, 2008). A key advantage of the ADCIRC model is the ability to couple storm surge computations with breaking wave radiation stress forcing calculated through a numerical wave model such as SWAN (*Holthuijsen et al.*, 1993; *Ris*, 1997) or STWAVE (*Smith et al.*, 2001). The accuracy of coupled ADCIRC and STWAVE simulations was investigated in a validation study using observed water levels during Hurricane Katrina (*Ebersole et al*., 2007). In this study, peak water levels were computed within 0.3 to 0.5 m absolute errors (*Ebersole et al.*, 2007).

A common feature exists throughout the array of numerical models available for hurricane storm surge computation. While these models differ in their computation methods and assumptions, they each implement some form of the conservation of mass and momentum equation as depicted in Equations 2.1 and 2.2. *Thomas and Nisbet* (2007) recognize a main factor limiting model performance as the lack of reliable topographic data, including information regarding vegetation height and type. However, even with the inclusion of highly resolved and spatially varying vegetation

characteristics, the physical accuracy of a model is limited to the validity of its representation of flow through vegetation.

2.5 Approximating Flow Resistance due to Vegetation

As stated in Section 2.1, flow through vegetation is often approximated through the use of a bottom friction term. Empirical equations describing open channel flow offer widely used and verified values for condensing vegetation effects to a bottom friction term. The Manning equation is one of the most widely used empirical equations approximating the hydraulics of vegetated flow (*Akan*, 2006). In SI units, the Manning equation for gravity-driven, steady open channel flow is:

$$\bar{u} = \frac{1}{n} R_h^{2/3} S_0^{1/2} \tag{2.13}$$

where $\bar{u}$ is the average flow velocity, n is the Manning's roughness coefficient, R_h is hydraulic radius, and S_0 is the water surface slope. Flow within a pipe is frequently described by the Darcy-Weisbach equation:

$$\bar{u}^2 = \frac{8gR_hS_0}{f} \tag{2.14}$$

where f is a dimensionless friction factor. While both the Manning and Darcy-Weisbach equations estimate flow through a conduit, the Manning formula is only valid for turbulent flow. The Darcy-Weisbach formula is more theoretically based and applicable to both turbulent and laminar flow regimes. However, deriving the Darcy-Weisbach friction factor (f) for an open channel involves an iterative procedure based on Reynold's number and depth. For this reason, the Manning's equation is more widely used to describe open channel flow than the Darcy-Weisbach equation (*Akan*, 2006). In

deriving a friction factor to relate vegetation to wave dissipation, *Augustin et al.* (in press) approximated the Darcy-Weisbach friction factor to be equivalent to a bulk drag coefficient (C_D'):

$$f = 8g\left(\frac{n}{h^{1/6}}\right)^2 \approx C_D' = C_D\left(\frac{l_s d}{sh}\right) \tag{2.15}$$

where C_D is the drag coefficient for individual stems, l_s is the stem length, d is the stem diameter, and s is the spacing between stems. Figure 1 provides a definition sketch for both submerged and emergent vegetation. *Augustin et al.* (in press) implemented the friction factor given in Equation 2.15 to calibrate a numerical model given laboratory measurements of flow through artificial, flexible vegetation.

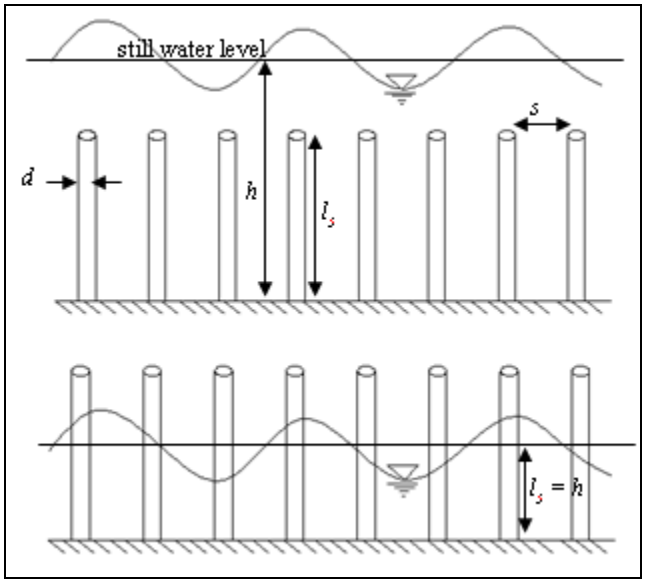

Figure 1. Definition sketch showing both submerged (top view) and emergent vegetation. Modified from *Augustin et al.* (in press).

Inclusion of vegetative drag in storm surge and wave modeling presents challenges that are currently addressed through simplifications and assumptions absorbed in the bottom stress term. Many studies develop an artificially high Manning friction coefficient (*n*) to take into account both bottom friction and vegetative drag (*Thomas and Nisbet*, 2007).

Two-dimensional surge models also approximate frictional effects arising from submerged vegetation into a single parameter, such as Manning's *n*, Darcy-Weisbach friction coefficient, or a quadratic friction coefficient. Some models, including the ADCIRC finite-element model, allow for the implementation of a depth-dependent friction coefficient (*Luettich and Westerink*, 1999). Nevertheless, the actual physics of vegetated fluid flow are substantially approximated within storm surge models. While improvements are being made to implement a more detailed representation of vegetation in numerical storm surge models, bottom friction tends be a tuning factor in model calibration. In fact, bottom friction, wind reduction at the surface, and eddy viscosity are all factors that are modified to calibrate the SLOSH model according to observational records (*Zhang et al*., 2008).

2.6 Attenuation of Storm Surge and Waves through Coastal Wetlands

Coastal wetlands have the potential to reduce surge levels and waves through several mechanisms, including vegetative drag within the water column, reduction in wave height and setup, and reduction in surface wind speed. In this study, the vegetative drag and wave dissipation effects are modeled. Reduction in surface wind speed is only discussed in this section, but should be a consideration when evaluating the full storm

protection potential of a wetland. Fluid flow through vegetation is different than flow through a clean open channel or unobstructed floodplain. *Kadlec* (1990) attributed vegetative drag and slight topographical variations to the velocity reductions encountered when flow is directed through a wetland. Though the body of research characterizing storm surge propagation within marsh and wetlands is limited, it is generally accepted that storm surge levels would be at least slightly reduced due to vegetative drag. *Walton and Christensen* (1980) recognized the inappropriate assumptions involved in modeling storm surge propagation through rigid wetland plants, and developed a modified Darcy-Weisbach friction factor describing friction through obstructed and unobstructed areas. These expressions were applied to a two-dimensional, depth-integrated surge model, in which the effects of bottom friction are investigated. For unobstructed flow, *Walton and Christensen's* friction factor is based on Nikuradse's equivalent sand roughness and depth of flow. For obstructed flow, the head loss due to trees and plants is considered, parameterized by the density of vegetation coverage, vegetation diameter, and spacing between plants. For a standard project hurricane (940 mb central pressure, 20.4 km radius of maximum winds, 20.4 km/h forward speed) making landfall along the Gulf coast north of Tampa, FL, surge levels were simulated for both a smooth and vegetated bottom. Results indicate that through the implementation of a vegetation-dependent friction factor, peak surge is both reduced and delayed with respect to a constant bottom friction factor that neglects vegetative drag. *Walton and Christensen* (1980) documented inland peak surge levels decreasing by as much as 0.5 m (1.5 ft), accompanied by a 30 minute delay in peak

surge response. In practice, inclusion of such detailed parameters describing vegetation is difficult, as compiling detailed dimensions of vegetation is tedious over the vast land area required by a storm surge model.

Though not specifically addressed in this study, vegetation associated with coastal wetlands also has an effect on wind velocities at the surface. *Reid and Whitaker* (1976) considered the wind stress ($\vec{\tau}_s$) at the water surface to be altered by a sheltering coefficient, S:

$$\vec{\tau}_s = \rho_a KS\left|\vec{W}\right|\vec{W} \tag{2.16}$$

where ρ_a is air density, *K* is a non-dimensional surface drag coefficient, and $\vec{W}$ is the standard anemometer-height (10 m) wind velocity. *Reid and Whitaker* established the sheltering coefficient (*S*) to be dependent on non-dimensional drag coefficients, number of vegetation elements per horizontal area, width of canopy elements, and exposed height of the canopy. Water surface profiles were computed for wind driven flow in a channel as measured in laboratory experiments by *Tickner* (1957), which proved to predict the measurements taken by *Tickner* with considerable accuracy. With a calibrated model for wind-driven flow through emergent vegetation, simulations were carried out to investigate the effects of a vegetative canopy within an enclosed basin. The basin consisted of a 3700 m by 6500 m area of 1.2 m depth. Half of the basin area was covered in vegetation, having an elemental width of 6.3 mm and a density of 6190 elements per square meter. Non-dimensional drag coefficients were adopted from the calibrated model that successfully predicted *Tickner's* (1957) laboratory results. Two

scenarios of vegetation height were simulated, one with the canopy fully submerged, and another with the canopy emerging approximately 0.07 m from the water surface, as depicted in Figure 2.

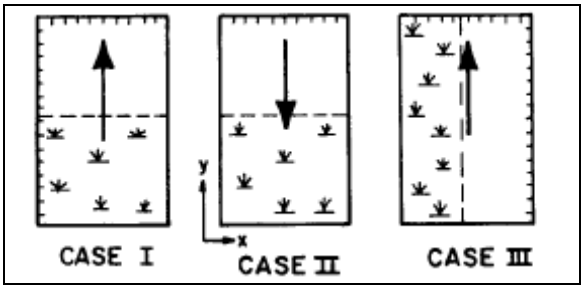

Figure 2. Vegetation distribution as investigated by *Reid and Whitaker* (1976) (From *Reid and Whitaker*, 1976).

Simulation results indicate that when wind is flowing from vegetation to open water (Case I) along the basin length (approximately 6500 m), the water surface elevation is unaffected by vegetation height above surface. However, when wind is directed toward vegetation as shown in Case II, water surface elevation is reduced by 0.2 m as canopy height is raised from 0.07 m under the water surface to 0.07 m above the water surface. *Reid and Whitaker's* analysis was revisited by *Danard and Murty* (1994), who conclude that the reduction of surface wind speeds through vegetation results in a dissipation of horizontal water velocities.

In addition to wind and water velocity reduction, coastal wetlands have the potential to significantly reduce wave heights. *Dean* (1978) suggested that a dense area of vegetation would have a damping effect on wave height, and *Dalyrmple*, *et al.* (1984) offer a method for calculating wave dissipation based on fixed cylinders. Laboratory

measurements obtained by *Asano et al.* (1988) depict wave heights decreasing by as much as 40% due to artificial seaweed constructed from polypropylene strips (25 cm in length, 5.2 cm wide, and .03 mm thick). *Asano et al.* (1992) and *Kobayashi et al.* (1993) revealed from these laboratory measurements that attenuation of small amplitude, monochromatic wave height through artificial vegetation follows an exponential decay:

$$H = H_o \exp(-k_i x) \tag{2.17}$$

where H_o is incident wave height, k_i is an exponential decay coefficient. *Mendez et al.* (1999) extended a wave dissipation solution to both monochromatic and irregular waves, dependent upon vegetation height, thickness, width, and flexibility. Computations by Mendez *et al*. (1999) are validated by laboratory experiments carried out by *Dubi* (1995). *Mendez et al.* (1999) found that wave dissipation is enhanced by increased vegetation height and density. However, up to a certain density (between 100 and 5000 vegetation units per square meter), the vegetation behaves as an impermeable step, resulting in an increase in wave height. *Dean and Bender* (2006) relate wave damping due to vegetation to a reduction in static wave setup of the water surface. *Augustin et al*. (in press) measured a significant reduction in wave energy through laboratory measurements. For waves propagating through 6 meters of artificial flexible vegetation stems, wave heights were reduced by between 20 and 41% (*Augustin et al*., in press).

Field measurements are difficult to obtain during a hurricane surge event. As a result, most of the literature supporting reduction of storm surge by wetlands refers to high water marks. In 1961, the US Army Corps of Engineers released a study that relates verified storm surge heights induced by several hurricanes to a reduction due to

coastal wetlands. In this study, peak surge heights are compiled for various sites located along the Louisiana coast. The relationship between peak surge height and distance from the coast is analyzed. A linear fit estimates that for every linear 4.4 km (2.75 miles) of wetland, average peak surge is decreased by approximately 0.3 m (one foot). The report states that while insufficient data is available to depict time lags of peak surge between coastal and inland stations, the relationship between surge reduction and inland distance is independent of hurricane forward speed, wind speed, and wind direction. Further, the 0.3 m reduction of storm surge levels for every 4.4 km is consistent for areas along both western and eastern Louisiana, where topography and land cover may vary between flat marshland and densely wooded ridges (*USACE*, 1961). Field reconnaissance of storm surge levels after Hurricane Katrina taken by *Fritz et al*. (2008) indicates that uprooted trees and storm surge damage decreases rapidly within the first 100 m of shoreline. Houses strategically located within several hundred meters of forest and marshlands to the south and east (upwind and upstream of the most significant hurricane wind and surge velocities) suffered less damage than structures located in the same region, showcasing the ability of coastal forests in reducing wind speeds, wave heights, water velocities, and ultimately peak surge levels.

2.7 Additional Benefits of Coastal Wetlands

Aside from storm surge and wave attenuation, coastal wetlands offer an array of environmental, social, and economic benefits. Wetlands are considered to have a high environmental value as a diverse population of plants, animals, and microbes rely on the wetland ecosystem for food, water, and shelter (*US EPA*, 2008a). It is becoming

understood that though the processes occurring in wetlands due to these life forms, wetlands may store carbon within the soil rather than releasing it as carbon dioxide, possibly tempering the causes of global climate change (*Choi and Wang*, 2004). In southeastern Louisiana, for example, the coastal wetlands at the Mississippi River Delta constitute the US's largest continuous coastal ecosystem, and act as the catch basin for a watershed the size of 40% of the lower 48 US states. Known as a robust natural wastewater treatment system, wetlands have been proven effective at removing biological and chemical pollution from water (*Reed*, 1991; *Kazmierczak*, 2001; *Rodgers and Castle*, 2008). In coastal Louisiana, wetlands are vital in the filtration of storm water and prevention of saltwater intrusion into drinking water sources (*Laska et al.*, 2005), valued at as much as $12,355 per hectare-year (*Kazmierczak*, 2001). Ninety percent of the Gulf of Mexico's freshwater input is filtered through the biologically rich wetlands surrounding the Mississippi River Delta (*Day et al*., 2005). With an estimated annual value of several billion dollars, coastal wetlands in Louisiana provide an assortment of natural resources. These activities include both the commercial and recreational harvest of fish, alligators, and fur mammals (*Day et al*., 2005). An estimated 25-35% of the United States' national fishery catch is landed in coastal Louisiana (*Otten et al.*, 2006). In 1997, 2.0 million individuals were part of the culturally diverse population of coastal Louisiana, including people of French, Spanish, African, Portuguese, German, Caribbean, Croatian, English, Italian, and Native American descent (Louisiana Coastal Wetlands Conservation and Restoration Task

Force, 1998). For hundreds of years, coastal inhabitants of Louisiana have taken part in a tradition of hunting, fishing, and trapping activities within wetlands.

2.8 Wetland Loss

Wetland losses in the United States are greatest in the northern Gulf of Mexico, where 80% of the nation's wetland losses occur (*Turner*, 1990). Between 1956 and 2004, an estimated 3541 km^2 of wetlands has been lost in Louisiana (*USGS*, 2006), an area larger than the state of Rhode Island. In this region, the conversion of wetlands to open water is a result of a number of factors, many of which are related to human impacts. Factors relating to wetland loss include land subsidence, global sea level rise, alterations in sediment and hydrologic exchange due to hydraulic structures, and storm erosion.

Day et al. (2000) conclude that a major factor contributing to land loss in Louisiana is the diversion of sediment, nutrients, and freshwater from the Mississippi River. Such diversions are a result of constructed levees and dams. The creation of a network of drainage and navigation canals along the Louisiana coast is identified as another major cause in wetland loss. Presently, approximately 15,000 km of canals exist within the Mississippi River Delta, adding up to an estimated 10% of the surface area of the Louisiana coastal marsh (*Turner et al*., 1982; Day *et al*., 2005; *Baustian and Turner*, 2006;). *Baustian and Turner* (2006) estimate the conversion of marsh to canals in the Louisiana coastal marsh is responsible for 22% of the total wetland losses between the 1930's and 1990. Even greater than the estimated effect of direct conversion of marsh to canal is the effect of dredged-material banks associated with constructed canals

(*Baustian and Turner*, 2006). There is evidence that the dredged sediment produced in the drilling of such canals interrupts hydrological processes, resulting in waterlogged marshland areas (*Day et al.*, 2000; *Baustian and Turner*, 2006;). This factor, combined with the increased residence time of saline waters flowing inland through deep manmade canals, ultimately results in the deterioration of coastal wetlands (*Day et al*., 2005).

Land subsidence is identified as a notable cause resulting in the loss of coastal wetlands. Subsidence is the result of the slumping of land due to the underground extraction of water or petroleum. The connection between petroleum extraction and land subsidence has been established through measurements in many parts of the world, including along the Louisiana coast (*Morton et al*., 2006). *Morton et al.* (2006) draw a correlation between increased hydrocarbon extractions in the 1960's to an accelerated wetland loss rate in coastal Louisiana. As hydrocarbon and water extraction declined in the 1980's, the wetland loss rate also declined. Stratigraphic marker studies by *Morton et al.* (2003) separate the effects of land subsidence from natural wave erosion. From these measurements, a subsidence rate of 2.3 cm per year is estimated in areas of extreme wetland loss.

Saltwater intrusion, increased erosion, and soil compaction are mechanisms in which hurricanes can cause coastal wetland loss. *Guidroz et al*. (2006) observe extensive vegetation losses within inland marshes after Hurricane Rita, a result of saltwater intrusion from the storm's nearly 6.0 m of surge. *Hackney and Bishop* (1981) describe the transport of debris from a salt marsh as a result of Hurricane Bob. The weak hurricane made landfall along the coasts of Louisiana and Mississippi, inducing a

1.0 to 1.5 m peak storm surge east of St. Louis Bay. In a small area of approximately 0.96 km^2, it was estimated through field measurements that 218,000 kg of debris was transferred away from the marsh, or approximately 16.7% of the annual plant production (*Hackney and Bishop*, 1981). After the 2005 hurricane season, the United States Geological Survey (USGS) estimates that approximately 562 km^2 of land was lost. This loss accounts for nearly 19% of the total land loss between the years 1956 and 2001, illustrating the potential a hurricane has in converting wetland to open water (Barras, 2006). Figure 3 details the effects of the 2005 hurricane season on Upper Breton Sound, approximately 40 km southeast of the city of New Orleans. The decrease in vegetative growth (as indicated by red shading) and increase in open water is visible within the marsh.

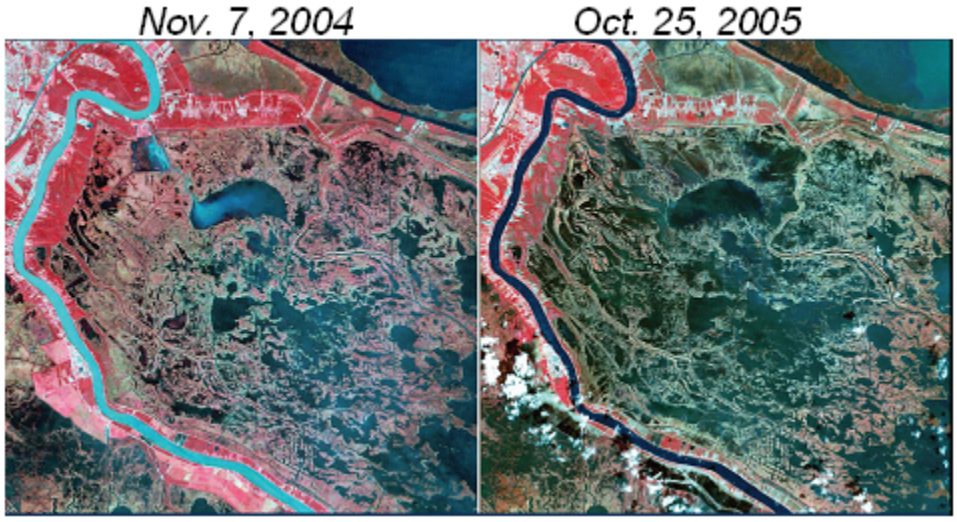

Figure 3. Satellite imagery depicting wetland losses after Hurricane Katrina (From *Barras*, 2006).

The hydrostatic pressure of hurricane storm surge is a component in the reduction of coastal wetlands due to storm events (*Stone et al*., 1997). After Hurricane Andrew, salt marshes were compressed in Louisiana by as much as 33 mm, not returning to original levels until 8 years later (*Cahoon et al*., 2006). A similar effect was noted in North Carolina, where soil was compressed by 20 mm by surge induced by two tropical storms (*Cahoon et al*., 2006).

Global sea level rise presents an obvious threat to coastal wetlands. A rising sea level inundates low-lying areas and alters soil properties, resulting in an inhospitable environment for certain wetland plant growth (*Donnelly and Bertness*, 2001). Historical measurements estimate global sea level rise to be 10 to 15 cm per century (*US EPA*, 1987). The Intergovernmental Panel on Climate Change (IPCC) estimates that the global sea level will rise between 18 to 59 cm by the year 2100 due to the expansion of the ocean waters and ice cap melting (*Solomon et al.*, 2007). A degree of uncertainty

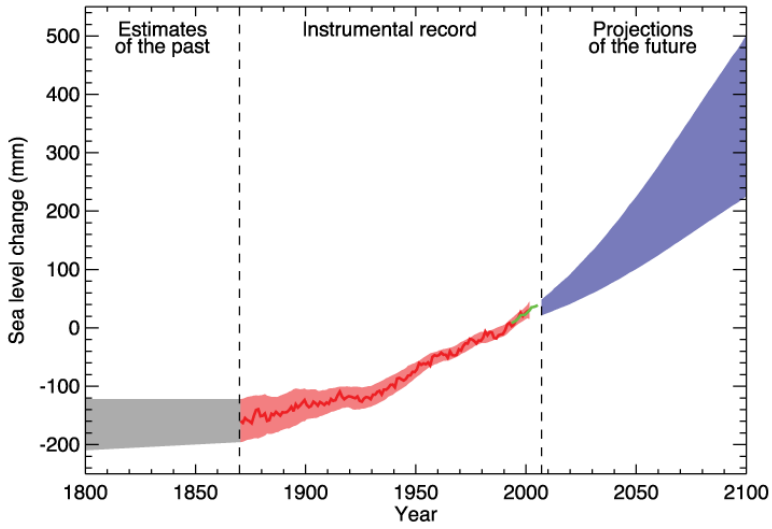

Figure 4. Historical and projected changes in global sea level (From *US EPA*, 2008b).

remains in the prediction of sea level rise and other effects related to climate change, though sufficient evidence exists so that such threats must not be disregarded. Figure 4 depicts historical and predicted trends in sea level rise.

2.9 Restoration of Coastal Wetlands

Marsh restoration, barrier island nourishment, canal backfilling, and hydraulic structures may dampen the effects of wetland loss. While these strategies have a limited value when applied individually, a large-scale effort of both ecological and engineering approaches is expected to have the greatest potential to restore areas of mass wetland loss, such as the Mississippi Deltaic Plain (*Day et al*., 2007).

Long-term marsh management techniques including the construction and operation of levees, weirs, pumps, and culverts have been applied to almost 20% of the Louisiana wetlands with very limited success (*Boyer*, 1997). Success is often tainted by the motivations of entities in charge, which may clash in a given region (*Boyer*, 1997).

For example, a management program with the goal of reducing land loss through the exclusion of certain species may conflict a bordering land governed by a management program with the goal of harvesting wildlife (*Boyer*, 1997). Aerial photographs were used by *Boyer* (1997) to correlate land loss reductions to management programs at 13 sites along the Louisiana coast. A statistical evaluation deduced that only three of the 13 sites had evidences of reduced land loss as a result of the management plan. *Boyer* (1997) concluded that, while the management programs may have been successful in terms of their individual and varying goals, such programs were not successful in terms of reducing wetland loss.

The rebuilding of eroded barrier islands is thought by some to be a promising element in the efforts to reduce wetland loss. Barrier islands reduce storm surge levels and wave heights, thereby reducing the storm-induced erosion and wetland loss (*Otten et al.*, 2006; *Day et al*., 2007). Nourishment and re-creation of barrier islands entails a major dredging and placement operation, thus requiring extensive funding which is subject to rising energy costs (*Day et al.*, 2005). *Otten et al*. (2006) investigated the cost and storm surge reducing properties of a proposed barrier island project along Terrebonne Bay, a 65 km stretch of coastline in southeastern Louisiana. The hypothetical project involved the raising of barrier islands by 5.0 m at a cost of $560 million. A surge reduction of 1.0 m in the event of a 5-meter surge was estimated as a result of the project (*Otten et al*., 2006).

Canal backfilling is another promising form of wetland loss abatement. As previously stated, construction of canals to support navigation and oil exploration

operations has contributed to a noteworthy portion of land loss within the Louisiana coastal wetlands. During construction, dredged material displaced by the canal is placed along the newly formed canal bank. Canal backfilling involves the return of this area of dredged material to the canal. Several studies are optimistic about such restoration efforts (*Neill and Turner*, 1987; *Baustian and Turner*, 2006; *Day et al*., 2007). *Baustian and Turner* (2006) surveyed the majority of backfilling projects along the Louisiana coast (30 separate sites), and found that an average of 58% of backfilled areas (formerly open water) were covered with vegetation.

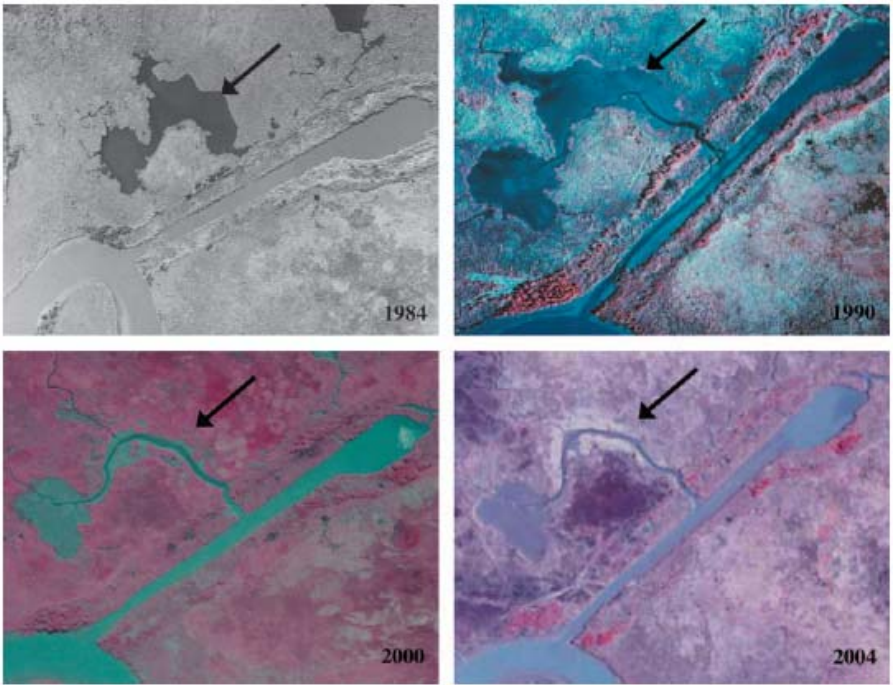

Figure 5. Effects of canal backfilling along the Vermilion River after 20 years. Arrow points to the same location in all snapshots (From *Baustian and Turner*, 2006).

It was also shown that plant communities living on areas once covered with dredged material resembled communities in the surrounding marshes untouched by canal effects (*Baustian and Turner*, 2006). Figure 5 depicts the conversion of open water to marsh in the years after a backfilling operation at the Vermilion River in south-central Louisiana.

Marshes may also be restored in more broad areas, involving the import of dredged material to create segments of marsh in areas otherwise covered by open water. An investigation of salt marshes in the Sabine National Wildlife Refuge in Louisiana indicates that after a few years, plant species of a restored marsh will resemble the species composition of surrounding natural marshes (*Edwards and Proffitt*, 2003). *Streever* (2000) concluded that restored marshes replicate many of the ecological functions, and provide a suitable habitat for smooth cordgrass (*Spartina alterniflora)*, the principal plant species native to salt marshes in the US (*USDA*, 2008). Wetland restoration costs are widely ranging, dependent upon energy prices and proximity to fill material sources. Of the restored marshes in Galveston, TX studied by *Rozas et al*. (2005), costs ranged between $28,523 and $60,344 and averaged $43,709 per hectare of added wetland (not including open water enclosed within marsh).

An estimated one billion dollars per year may be provided to Gulf coast states for the purpose of coastal restoration during the next 30 years as part of the Gulf of Mexico Energy Security Act (*Day et al.*, 2007). Each technique mentioned in this section has some degree of potential to reverse wetland loss. To optimize the restoration on a regional scale, a coalescence of both engineering and ecological efforts must be

employed. *Day*, *et al.*, 2007 underscored the need for restoration efforts to rely on natural forces. At the Mississippi Delta, the total reliance on natural, deltaic processes to restore wetland is unrealistic due to the complications already induced by human intervention. *Day et al*. (2007) punctuated four pillars of restoration that should be harmoniously employed in the Mississippi Delta Plain, including 1) cutting of crevasses along the natural bank of the Mississippi to nourish sediment-starved areas, 2) restoration through dredged material, 3) restoration of barrier islands, and 4) backfilling of canals. *Day et al*. (2007) also recognized that the southeastern Louisiana is a hub for commercial and industrial activity, and a restoration plan must be one that works with, not against, entities working and living on the Mississippi Delta.

2.10 Summary of Background with Respect to Research Objective

Background information included in this literature review is wide-ranging, though each topic is uniquely related to the potential reduction of storm damage through coastal wetlands. Governing equations are pertinent in terms of identifying the dominant factors affecting storm surge and wave energy impact due to hurricanes. From the governing equations, it is shown that the dominant factors affecting setup of the water surface during a hurricane are the still water depth, wind speed, atmospheric pressure gradient, and bottom friction, which here incorporate vegetated drag within the water column. Background information regarding the dynamics of waves and storm surge is essential in interpreting results presented in this thesis. Of the storm surge models discussed in the background review, ADCIRC is among the models having reliability in terms of representation of bottom friction and relative accuracy of predicting storm surge

along the US coast, particularly within the Gulf of Mexico. This provides the basis for using ADCIRC as the numerical model of choice in this study, as well as the STWAVE model, as it derives wave parameters and radiation stress through coupling with ADCIRC. As discussed in the previous sections, the physics of flow resistance and wave attenuation due to wetland vegetation is complex, with much research needing to be carried out before an accurate analytical scheme may be developed. However, empirical equations do exist (such as the Manning's equation for open channel flow) that may provide an estimation of the reduction of storm surge and wave energy until such complex physics are resolved. While the focus of this thesis is the reduction of storm surge and wave energy through parameters acting within the water column, information presented in this literature review regarding the reduction of surface wind stress should be considered for a wetland of emergent vegetation.

The value of a coastal wetland extends beyond the potential to reduce hurricane impacts. Due to the significant rate of wetland loss, marsh restoration is well documented as an effort to restore the cultural, environmental, and economical benefits imposed by coastal wetlands. Results presented in this thesis relate to the sensitivity of storm impacts to bottom friction, elevation, and continuity (degree of segmentation, defined by area of marsh delineated by channels within a total marsh system) of a coastal wetland. It is hoped that this information may be used to optimize wetland restoration efforts in terms of maximizing storm protection potential.

3. MODELS AND METHODS

3.1 Introduction

This thesis presents findings derived purely from numerical model results. The principle models applied in this study (ADCIRC and STWAVE) are described herein, along with the techniques used to couple both models to integrate storm surge levels with wave energy, and vice versa. ADCIRC is a hydrodynamic model describing coastal circulation and storm surge, solving the momentum balance and conservation of mass equations on a finite-element grid, while STWAVE is a model capable of describing the nearshore transformations of gravity water waves. Section 3.2 describes this coupled execution of ADCIRC and STWAVE. To obtain the wind and pressure fields required by ADCIRC and STWAVE, two models were used (WAM and PBL), as briefly described in Sections 3.3 and 3.4. The ADCIRC and STWAVE models are described in Sections 3.5 and 3.6, respectively. With the framework of the numerical modeling methodology described, Sections 3.8 through 3.10 detail the specifics on how wetland parameters are investigated in terms of wave and surge sensitivity. Section 3.11 provides an overview of the meteorological characteristics of the storms simulated in this study.

3.2 Execution of ADCIRC and STWAVE

To couple the effects of wave radiation stress and storm-driven flow, the ADCIRC and STWAVE models are coupled. Three simulations are required for each storm event: 1) ADCIRC forced with wind and pressure, 2) STWAVE forced with offshore wave spectra, wind, and surge levels, and 3) ADCIRC forced with wind,

pressure, and wave radiation stress. With the wind and pressure files obtained through the PBL model, the first run of ADCIRC provides a global surge output. This provides some data for preliminary analysis, though neglects wave radiation stress. To include the effects of wave setup and setdown, the STWAVE model is executed, driven by wind, surge previously computed by ADCIRC, and wave spectra calculated for the open-water boundary using WAM. With this step complete, significant wave height, wave period, and wave direction may be analyzed. ADCIRC is subsequently re-executed, forced by wind and pressure provided by the PBL model, and radiation stress provided by the STWAVE model. This yields surge results that not only take into account wind and pressure forces, but also the effects of wave setup and setdown. These are the surge results discussed in this thesis. Figure 6 depicts the basic process used in modeling the results presented in this thesis.

ADCIRC and STWAVE were executed using the Cray XT3 massively parallel processor (MPP) supercomputer provided by the US Army Engineer Research and Development Center (ERDC) Major Shared Resource Center (MSRC). The system is comprised of 4160 dual-core processors (2.6 Ghz AMD Opteron, 64-bit), physically located at the US Army Engineer Research and Development Center headquarters in Vicksburg, Mississippi.

In this study, ADCIRC simulations were executed in parallel using 24 processors, for a computation time of approximately 75 minutes per simulation. The execution of ADCIRC along a parallel platform results in lower computation time due to partitioning the grid domain over the 24 individual processors. The processors

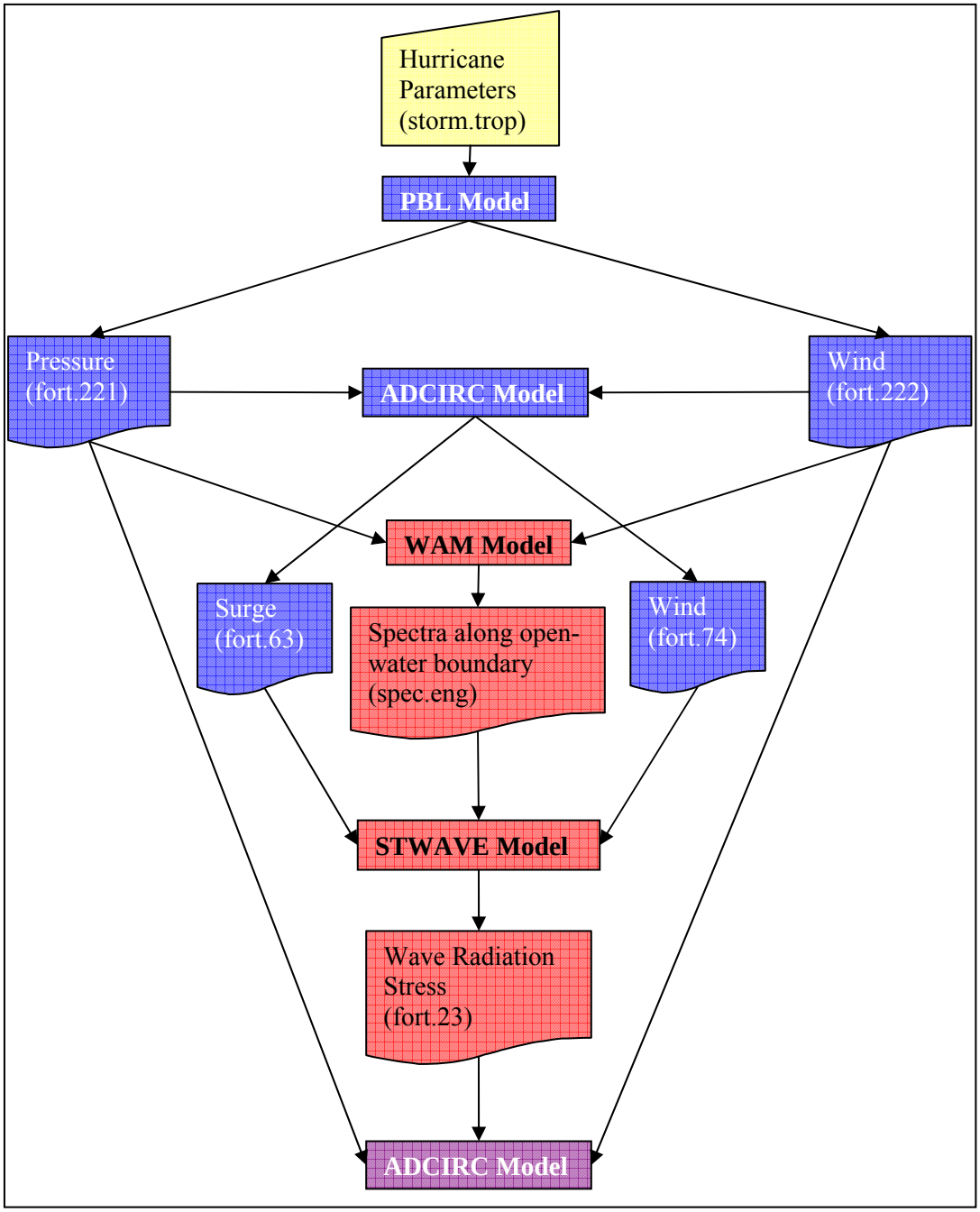

Figure 6. Overview of the modeling process.

coordinate computations through a message passing interface (MPI) protocol (*Westerink et al*., 2008). STWAVE was executed using 93 processors, with a run time of approximately 15 minutes per simulation.

3.3 Planetary Boundary Layer Model (PBL)

Pressure and wind forcing is derived from the planetary boundary layer (PBL) model developed by *Cardone et al.* (1992). The PBL model develops atmospheric forcing inputs for ADCIRC at each time interval, based on a simple input of hourly hurricane parameters. These parameters include storm size, minimum central pressure, eye position, and forward velocity. The PBL model translates this information into a wind file and pressure file, which is used as forcing files in ADCIRC (see Section 3.5) and STWAVE (see Section 3.6). The model is based on the assumption that the parameters of a hurricane will remain relatively constant over short durations (in this case, one hour), and that a translating storm may be estimated using a moving coordinate system. To optimize computing efficiency, wind and pressure fields are formatted in a nested grid with the origin coinciding with the eye of the storm. In this way, wind and pressure fields are depicted at a high resolution near the eye, and a low resolution far away from the storm. This nested grid format is translated with the speed and direction of the hurricane, so that the eye is constantly affixed at the origin (*Thompson and Cardone*, 1996).

3.4 Wave Prediction Model (WAM)

To provide offshore conditions to drive the STWAVE model, wind fields taken from the output of the PBL model were used to drive the Third Generation Ocean Wave

Prediction Model, known as the WAM (Wave Prediction Model) program. The WAM model is based in spherical coordinates (latitude and longitude), and solves the spectral transport equation for deep water. The ocean wave spectrum in terms of frequency and direction is evolved within the deep water, taking into account white capping, nonlinear energy transfer, and wind-wave growth. The model extends to the shallow water through solving the wave dispersion relation. Calibrated against wave growth data based on fetch-limited wind, the WAM model was verified through hindcasting various North Atlantic storms and Gulf of Mexico hurricanes (*WAMDI Group*, 1988). In this study, WAM output (*R.E. Jensen*, personal communication) was produced by the Coastal and Hydraulics Laboratory (CHL) of the US Army Engineer Research and Development Center (ERDC).

3.5 Advanced Circulation (ADCIRC) Finite Element Model

The Advanced Circulation Model (ADCIRC) is a finite element model capable of resolving water surface elevations and velocities based on atmospheric, wave, and tidal forcing. A grid structure of triangular elements defined by nodes provides the framework for computations in a spherical coordinate system. At each node, physical parameters are associated with a latitude and longitude, providing a mapping of elevation, bottom friction, and wind reduction due to vegetative drag. Boundary conditions may be specified along node strings. Tidal conditions, overtopping and non-overtopping levees, and river inflow may be emulated through the specification of boundary conditions. These boundary conditions may be specified both within and surrounding the grid.

The model is executed in either three dimensional or two dimensional (depth integrated) form. All results presented in this thesis involve the two-dimensional, depth-integrated form, referred to as ADCIRC-2DDI (Version 46.57). The two-dimensional version of ADCIRC is the standard model used in risk analysis by the US Army Corps of Engineers and FEMA. For this version, the continuity (Equation 2.1) and momentum equations (Equation 2.2) are solved for each elemental area in spherical coordinates (*Westerink et al.*, 2008). During execution, the Generalized Wave Continuity Equation (GWCE) is produced through the substitution of the momentum equation into the continuity equation (*Luettich and Westerink*, 2004). This equation is solved, yielding the instantaneous free surface elevation and velocity field. The calculation scheme featuring the GWCE formulation is advantageous over other models, as it provides a more stable representation of the water surface that is less prone to numerical instability.

ADCIRC resolves varying bottom friction through a nonlinear bottom friction coefficient (B_f) found in the expression for bottom friction term (*Westerink et al.*, 2008):

$$\tau_* = B_f \left[\frac{\sqrt{U^2 + V^2}}{h} \right] \tag{3.1}$$

The bottom friction coefficient (B_f) may be hinged upon one of a selection of friction factors, including Manning's *n*, Chezy friction coefficient, or a Darcy-Weisbach friction coefficient. To provide a well-recognized and industry-standard friction specification, all bottom stress in this study is formulated around the coefficient used in the Manning equation for open-channel flow (*n*). For this configuration, ADCIRC relates Manning's *n* to the nonlinear bottom friction coefficient (*Luettich et al.*, 2004):

$$B_f = \frac{gn^2}{h^{1/3}} \tag{3.2}$$

ADCIRC reads in the forcings from the PBL model as 1) Two-component wind velocity and 2) atmospheric pressure. The wind velocity is converted to surface stress (*Westerink et al*., 2008):

$$\tau_{sx} = C_d \rho_a \left|\vec{W}_{10}\right| W_{10,x} \tag{3.3}$$

$$\tau_{sy} = C_d \rho_a \left|\vec{W}_{10}\right| W_{10,y} \tag{3.4}$$

where C_d is *Garratt's* (1977) drag coefficient, ρ_a is air density, and W_{10} is wind speed at a 10 m height. Garratt's drag coefficient is defined by:

$$C_d = (0.75 + 0.067 W_{10}) \times 10^{-3} \tag{3.5}$$

where W_{10} is in units of m/s.

ADCIRC has the capability of adjusting applied wind stress for canopy drag due to trees and structures. Canopy drag effects are not analyzed in this thesis, and will therefore not be discussed in this section. Tidal forcing was also neglected in this study to provide a controlled environment, free of extraneous effects. While ADCIRC has the ability to precisely drive flow and surface elevation through tidal forcing, the formulations and theory behind these effects are not discussed in this section.

3.6 Steady State Spectral Wave (STWAVE) Model

The Steady-State Spectral Wave Model (STWAVE) is a finite-difference model, capable of resolving nearshore wave processes including refraction, shoaling, steepness-limited breaking, diffraction, wave generation due to wind, wave-wave interaction, and energy transformation due to whitecapping. The model domain is provided by a Cartesian grid based on a local coordinate system. Open or closed boundaries contain the grid, representative of open-water or land, respectively. Grid cells are square and equal in size, defined by an area small enough to resolve bathymetric features of interest. STWAVE may be driven by wind, fluctuating water levels, currents, and wave spectra specified along an open-water boundary. The offshore boundary condition is specified through wave spectra that capture the offshore wave climate, thus providing a starting point for nearshore (depths less than 40 m) wave transformation and generation. In this study, the WAM model (*WAMDI Group*, 1988) was used to convert wind fields applied over a large scale domain into wave spectra at the offshore boundary of the STWAVE grid. The WAM inputs were provided by the study sponsor (*R.E. Jensen*, personal communication, February 29, 2008). STWAVE accounts for currents, wave refraction, and shoaling through energy conservation in the direction of wave propagation, μ:

$$\mu = \tan^{-1}\left(\frac{C_{gr}\sin\alpha + U\sin\delta}{C_{gr}\cos\alpha + U\cos\delta}\right) \tag{3.6}$$

where C_{gr} is the group celerity relative to the current speed. Group wave celerity and wave celerity (C_r) is provided by a solution expressed:

$$C_r = \frac{\omega_r}{k} \tag{3.7}$$

$$C_{gr} = 0.5C_r\left(1 + \frac{2kh}{\sinh 2kh}\right) \tag{3.8}$$

Diffraction is modeled through the spreading of energy in frequency and direction bands:

$$E_j(\omega_a, \alpha) = 0.55E_j(\omega_a, \alpha) + 0.225\left[E_{j+1}(\omega_a, \alpha) + E_{j-1}(\omega_a, \alpha)\right] \tag{3.9}$$

where E is energy density within a frequency band, ω_a is angular wave frequency within a static frame of reference, α is wave direction reference to the wave crest, and the subscript j denotes the index of the grid cell in the alongshore position. Breaking within the surf-zone is specified by the *Miche* (1944) criterion:

$$H_{m0,\max} = 0.1L\tanh(kh) \tag{3.10}$$

where $H_{m0,\,max}$ is the zero-moment, energy-based wave height, L is wavelength, and k is wave number. Wind energy is transformed into wave energy through the energy flux F_{in}:

$$F_{in} = \Lambda\frac{\rho_a}{\rho_w}0.85C_m\frac{u_*^{\,2}}{g} \tag{3.11}$$

Where F_{in} is the wind to wave energy flux, Λ is a coefficient dictating the percentage of momentum transferred to the water from the atmosphere (0.75), C_m is the mean wave celerity, and u_* is the friction velocity, which is dependent on wind speed and drag coefficient. Wave interaction is taken into account by a nonlinear distribution of energy

from the peak frequency to lower and higher frequencies. Increases in wind fetch result in an increase in the spectral peak, f_p:

$$(f_p)_{i+1} = \left[(f_p)_i^{7/3} - \frac{9}{5}\varsigma\left(\frac{u_*}{g}\right)^{4/3} \Delta t \right]^{-3/7} \tag{3.12}$$

where the subscript i is the grid column index, ς is a dimensionless coefficient, and Δt is the time for a wave to travel across a grid cell. Whitecapping, wave breaking, and turbulence results in a transfer of energy from low to high frequencies. This results in a dissipation of wave energy, given by the energy flux Γ_E :

$$\Gamma_E = \frac{\varepsilon g^{1/2} E_{tot}^{\ 3} k_p^{\ 9/2}}{\tanh^{3/4}(k_p h)} \tag{3.13}$$

where ε equals 30, E_{tot} is the sum of spectrum energy divided by $\rho_w g$, and k_p is wave number at the spectrum peak.

Recent versions (*Smith*, 2007) of STWAVE allow bottom friction to be imposed during wave simulations. Similarly to ADCIRC, STWAVE allows the user to specify bottom friction using the Manning's *n* coefficient of bottom roughness. The effects of bottom friction are imparted through an energy loss (S_{bf}) in the wave spectrum:

$$S_{bf} = \frac{-1}{g}\left(\frac{gn^2}{h^{1/3}}\right)\frac{\omega^2}{\sinh^3(kh)} E(f,\alpha) u_{rms} \tag{3.14}$$

where u_{rms} is root-mean-square of the bottom velocity and ω is angular wave frequency.

Radiation stress calculated through STWAVE is required by ADCIRC to include the effects of wave set-up and set-down. Radiation stress tensors (S_{xx}, S_{xy}, S_{yy}) are based on linear wave theory, calculated as:

$$S_{xx} = \rho_w g \iint E(f,\alpha)\left[0.5\left(1+\frac{2kh}{\sinh 2kh}\right)\left(\cos^2\alpha+1\right)-0.5\right]dfd\alpha \tag{3.15}$$

$$S_{xy} = \rho_w g \iint \frac{E(f,\alpha)}{2}\left[0.5\left(1+\frac{2kh}{\sinh 2kh}\right)\sin 2\alpha\right]dfd\alpha \tag{3.16}$$

$$S_{xx} = \rho_w g \iint E(f,\alpha)\left[0.5\left(1+\frac{2kh}{\sinh 2kh}\right)\left(\sin^2\alpha+1\right)-0.5\right]dfd\alpha \tag{3.17}$$

Radiation force is output as τ_x / ρ_w and τ_y / ρ_w, where:

$$\tau_x = -\frac{\partial S_{xx}}{\partial x} - \frac{\partial S_{xy}}{\partial y} \tag{3.18}$$

$$\tau_y = -\frac{\partial S_{xy}}{\partial x} - \frac{\partial S_{yy}}{\partial y} \tag{3.19}$$

STWAVE operates under the assumption that waves are constantly fully developed by wind conditions. In other words, STWAVE neglects the time in which wind is applied to the water surface. Reflection and nonlinear components of refraction are neglected, and the bottom slope is considered to be mild. Results presented in this thesis are derived from a half-plane version of the STWAVE model, meaning wind and waves traversing in the seaward direction (away from land) are neglected. This is suitable in the simulation of hurricane effects, as shoreward propagating waves are dominant in magnitude and relevance.

3.7 Idealized Grid Setup

To provide a basis for general application along a number of coastlines, an idealized grid (*Irish et al.* 2008) having a constant continental shelf slope and smooth

bathymetry is selected. Several profiles offshore of southeastern Louisiana (Figure 7) are analyzed to assist in the selection of a bottom slope.

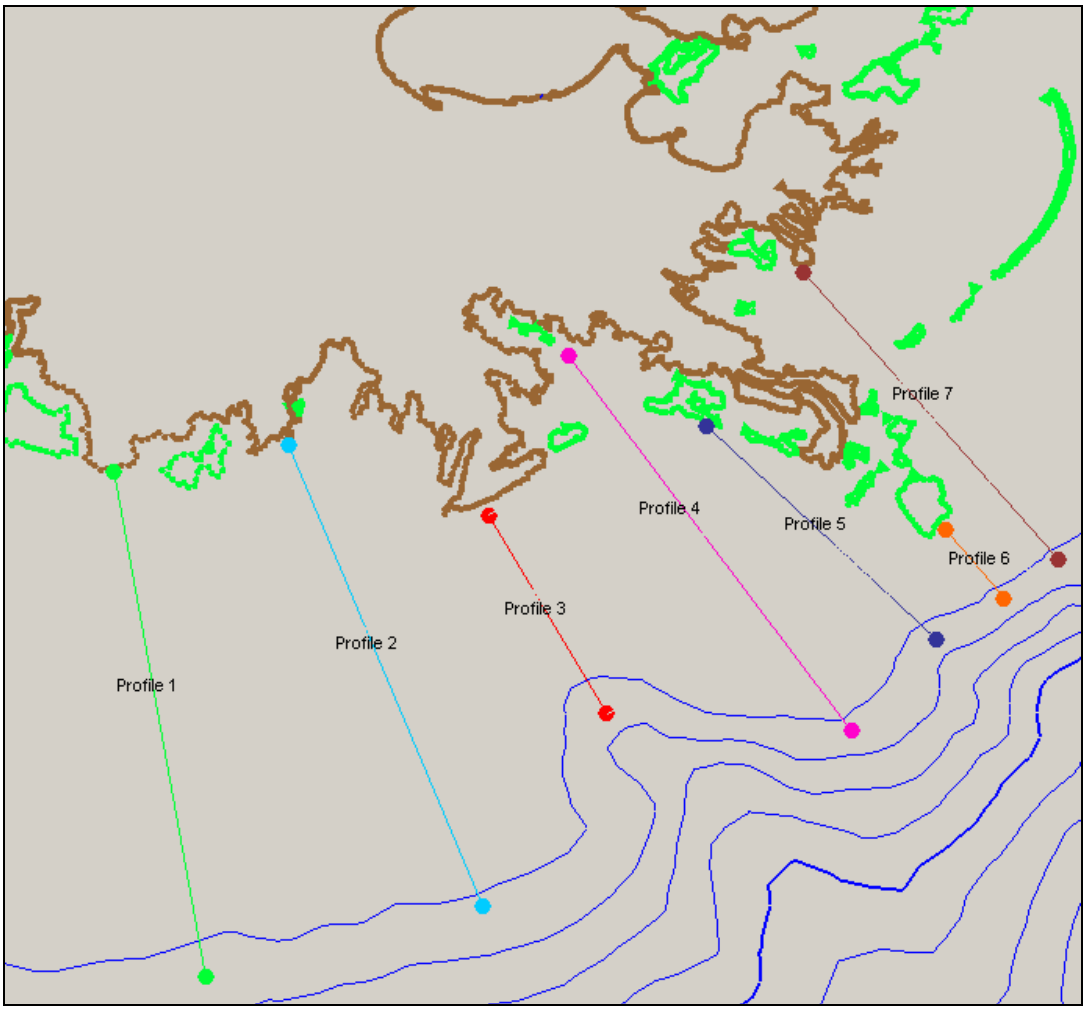

Figure 7. Existing bathymetric profiles surveyed for bottom slope selection in idealized grid. Brown indicates land boundaries, green indicates island boundaries, and blue contours indicate bathymetry, at 200-m intervals. Grid data is provided by US Army Corps of Engineers (2008).

After the analysis these bathymetry profiles, it is determined that a 1:1000 continental shelf slope will approximately represent the bathymetry surrounding southeastern Louisiana. A bottom slope of 1:250 is used to transition between the marsh

and surrounding bathymetry. Figure 8 depicts the idealized profile leading between the land boundary and the continental shelf. The zero-slope area between 0 and 20000 m represents the marsh extending 20 km seaward.

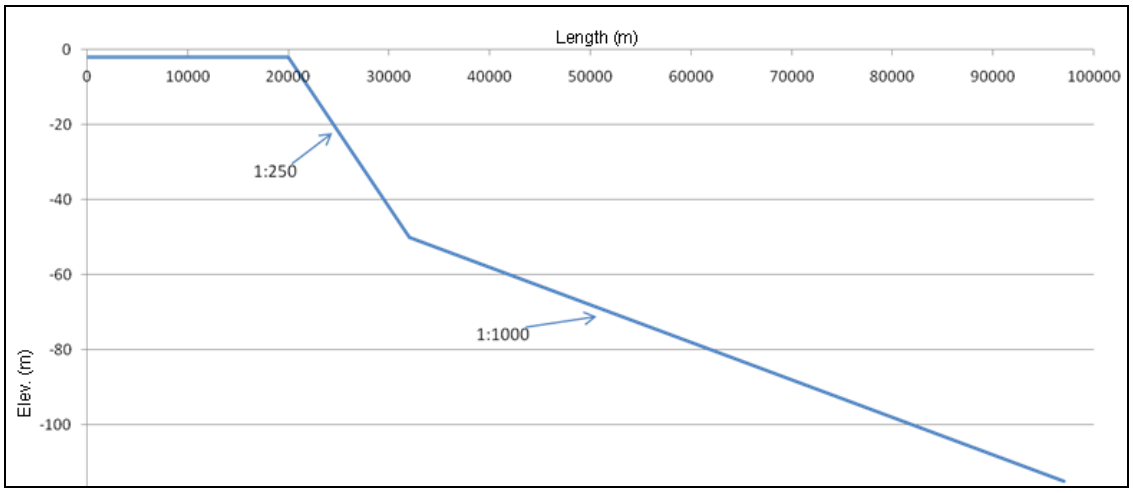

Figure 8. Bottom slope configuration chosen for this study.

With bottom slopes selected, an idealized grid featuring a simple 1:1000 sloping continental shelf is edited to feature a 20 km by 20 km perturbation representative of a 400 km^2 marsh. To provide a computationally stable and adequately detailed representation of the marsh feature, the grid is highly resolved around the marsh with an average grid spacing of 200 m. Figure 9 shows the overall domain of the grid, and Figure 10 shows the location of the idealized marsh in respect to the existing shoreline of the northern Gulf of Mexico. The Surface Water Modelling System (*SMS*, 2002) is used in grid editing. Aside from the idealized marsh perturbation, bottom friction is held constant throughout the grid domain, at a Manning's *n* value of 0.020, representative of a sandy surface (*Chow*, 1959).

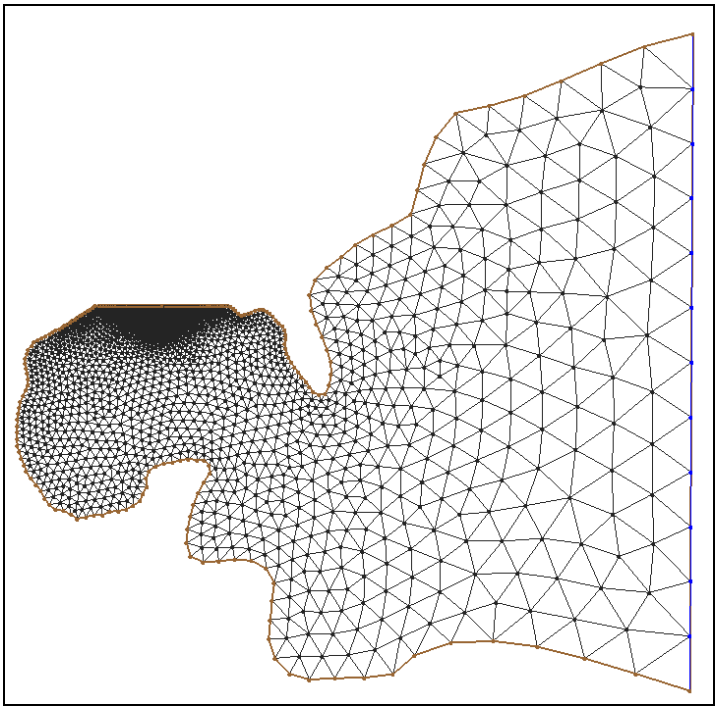

Figure 9. ADCIRC domain used in this study. Blue lines indicate open-water boundary condition, while brown lines indicate land boundaries.

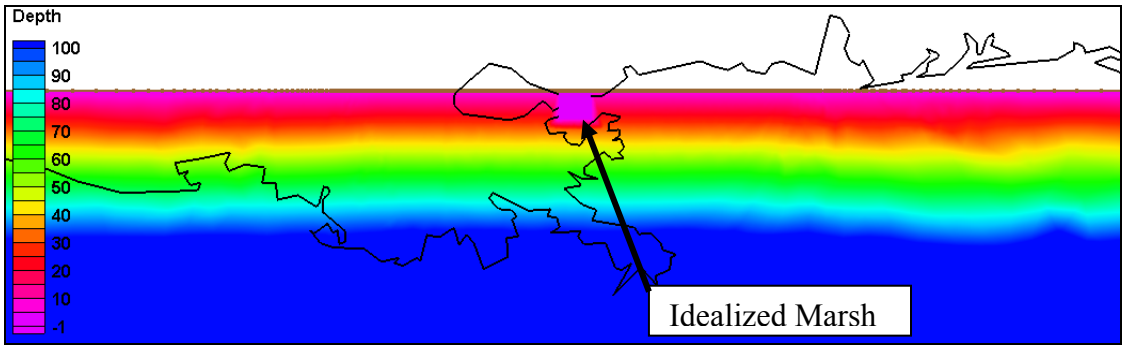

Figure 10. Location of idealized marsh in respect to the coastline of the Gulf of Mexico near New Orleans, Louisiana. Color contours indicate depth of idealized grid. Black lines overlay the actual land/water boundary of the northern Gulf of Mexico.

3.8 Model Setup for Investigation of Bottom Friction Effects

A set of five grids is developed to model surge over a marsh-like feature of increased bottom friction. Marsh elevation is held constant at 0.5 m above mean sea level for each idealized grid, representing a high-water marsh (Figure 11). Bottom friction is implemented using a Manning's *n* applied over the 20 km by 20 km marsh area.

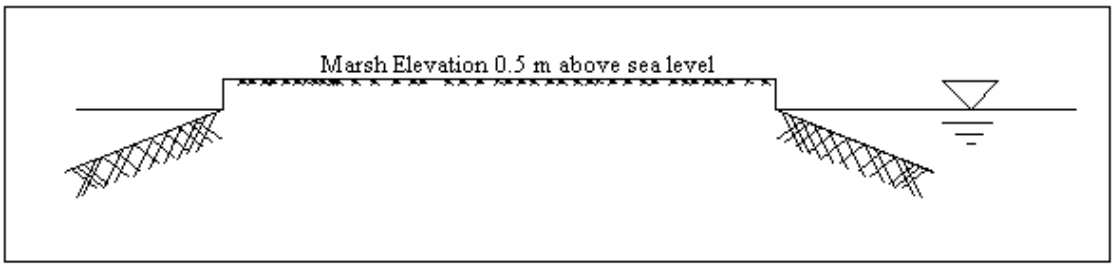

Figure 11 Cross section of idealized marsh used in the investigation of bottom friction effects.

Five Manning's *n* values are selected, ranging between 0.020 and 0.300, as shown in Table 1. Surfaces represented by the Manning's *n* values in this study range from sandy (as implemented elsewhere in the grid) to unrealistically rough (to provide an upper bound in model simulations).

Table 1. Manning's *n* values used in bottom friction simulations.

Grid	Elevation (m)	Manning's *n*	Representative of: (Chow, 1959)
MAN1	0.5	0.020	Sandy surface
BASE	0.5	0.035	High grass
MAN2	0.5	0.050	Scattered brush
MAN3	0.5	0.075	Dense brush
MAN4	0.5	0.150	Dense woods
MAN5	0.5	0.300	Unrealistic

3.9 Model Setup for Investigation of Elevation Effects

Surge response due to changes in marsh elevation is investigated through four grids featuring a marsh feature of varying elevation. To eliminate the effects of bottom friction, Manning's *n* across the idealized feature is held constant at 0.020 for all grids analyzing marsh elevation (representing a sandy bottom). Marsh elevations are chosen to represent a degrading marsh, from 0.5 m above sea level (MAN1) to 3.0 m below sea level (ELV4), but also represent various tidal marshes found in the Gulf of Mexico. The marsh at 0.5 m above sea level is representative of a high water tidal marsh (inundated only at high tide), while the marsh at 0.6 m below sea level is representative of a low tidal marsh. The configuration featuring a marsh at 0.2 m below sea level represents a mid level tidal marsh (*LaSalle*, 2008). Figure 12 provides a cross section of the idealized marshes detailing the effects of marsh elevation.

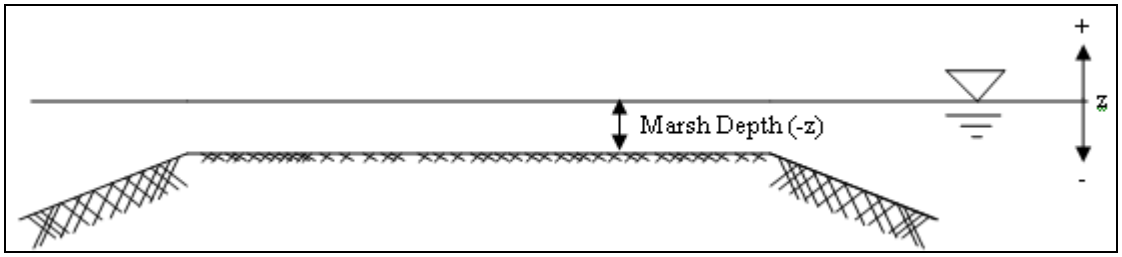

Figure 12. Cross section of idealized feature used in the investigation of marsh elevation.

Table 2 presents the characteristics of the grids for investigating elevation effects. The MAN1 grid used in the bottom friction analysis is a part of this suite, as it features the same bottom friction (n = 0.020) as the other elevation grids.

Table 2. Elevation values used in simulations investigating marsh elevation.

Grid	Elevation, z (m)	Manning's n
MAN1	0.5	0.020
ELV1	-0.2	0.020
ELV2	-0.6	0.020
ELV3	-1.8	0.020
ELV4	-3.0	0.020

3.10 Model Setup for Investigation of Marsh Continuity Effects

Marsh continuity is defined as the degree of segmentation, equal to the area of marsh at an elevation of 0.5 m above sea level divided by the total area of the marsh

system (400 km^2). To achieve a non-continuous marsh, channels are introduced, dividing the 20 km by 20 km square marsh feature into 16 squares of equal area, elevation, and bottom friction, as shown in Figure 13.

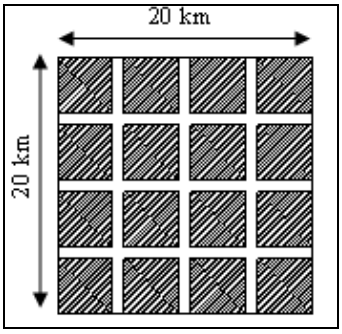

Figure 13. Plan view of non-continuous marsh. Shaded areas indicate regions of increased bottom friction and elevation.

The small marsh segments feature an elevation of 0.5 m and bottom friction of n = 0.035 (tall grass). Channels delineating the marsh segments feature a 2.0 m depth and a bottom friction of n = 0.020 (sandy bottom). Figure 14 shows the marsh cross section.

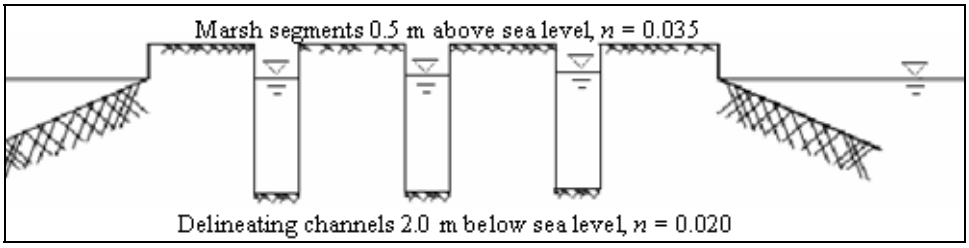

Figure 14. Alongshore cross section of non-continuous idealized marsh.

In this study, two non-continuous marshes were evaluated, having continuities of 75% and 50%, as depicted in Table 3. The 75% continuous marsh features 900 m wide channels, while the 50% continuous marsh features channels that are 2000 m wide.

Table 3. Continuity values used in simulations investigating marsh segmentation.

Grid	Continuity	Channel Width (m)
BASE	100%	0
CON1	75%	900
CON2	50%	2000

3.11 Storm Selection

To provide a wide range of surge and wave conditions, a suite of storms with varying hurricane sizes and minimum pressures is selected for this study. Six storms are chosen, having minimum central pressures between 900 and 975 mb, and scale pressure radii between 20.4 and 74.1 km. Forward speed is held constant for all storms at 5.6 m/s (10.9 kts). The use of multiple storms having varying characteristics provides insight into a marsh's storm protection value during a wide range of storm conditions. Table 4 lists the properties of the storms used in the ADCIRC and STWAVE simulations, along with associated peak surge and wave characteristics as simulated for the MAN1 grid.

To provide maximum surge levels at the marsh, storm tracks were shifted so that the marsh was located to the east of the storm at landfall. Each storm was shifted by a distance equal to the pressure radius. A trial run of ADCIRC simulations proved this to be an adequate method in allowing the peak surge to impact the marsh. Figure 15 depicts a representative storm track used in this study.

Table 4. Suite of storms used in idealized simulations.

Storm	Landfall Minimum Central Pressure (mb)	Landfall Pressure Radius (km)	Forward speed (m/s)	Peak Incident Wave Height (m)	Peak Incident Wave Period (s)	Peak Surge over MAN1 grid (m)
Storm 1	900	20.4	5.6	7.0	9.6	6.5
Storm 2	900	38.9	5.6	8.5	11.4	7.1
Storm 3	900	74.1	5.6	10.3	12.7	7.5
Storm 4	941	38.9	5.6	6.6	10.3	4.8
Storm 5	975	20.4	5.6	4.0	7.7	2.8
Storm 6	975	38.9	5.6	4.8	9.1	3.1

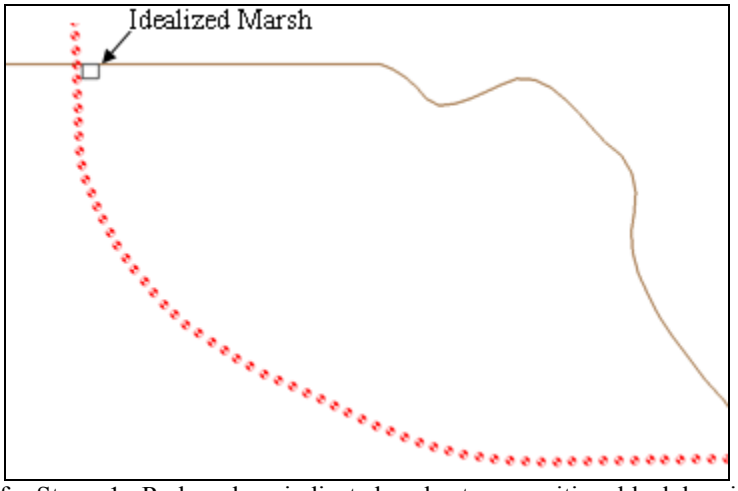

Figure 15. Track for Storm 1. Red markers indicate hourly storm position, black box indicates idealized marsh, and brown lines represent idealized coastline.

3.12 Conclusions

Detailed in this section are the numerical models and methods used to investigate the effects of certain physical wetland properties on hurricane storm surge. The primary models used in this study are the ADCIRC and STWAVE models, which provide descriptions of hydrodynamic and wave effects, respectively. These models are supported by the WAM and PBL models, which provide input used in the ADCIRC and STWAVE simulations. To provide a controlled environment and for investigating wave and surge sensitivity to marsh properties, an idealized grid is modified. A bottom slope resembling that of the northern Gulf of Mexico coast is used, yet the bathymetry remains appropriately generic so that study results may be applied to locations elsewhere. Various grid configurations in terms of bottom friction and bathymetry are fashioned to investigate wave and surge sensitivity to bottom friction, elevation, and continuity (degree of segmentation) of an idealized 20km by 20km marsh. Six storms of varying central pressure and size are chosen to provide a range of wave and surge conditions, ranging from 4.0 to 10.0 m incident wave height and 2.8 to 7.5 m of surge for the MAN1 grid. It should be noted that storms of increasing incident wave height correspond to storms of increasing surge potential throughout this study. Grid suites described in the previous sections provide a controlled environment in which each wetland characteristics of interest may be investigated in solidarity. Results of simulations over these grid suites are discussed in the next section (Section 4).

4. EXPERIMENTAL RESULTS

4.1 Introduction

Presented in this section are the ADCIRC and STWAVE numerical model results investigating wave and surge sensitivity of bottom friction, elevation, and continuity of an idealized 20 km by 20 km wetland feature. Each section begins with a discussion on wave impacts, followed by analysis of surge impacts. Changes in wave height are described in terms of changes in meters, while surge sensitivity is referenced in terms of percent difference. Percent differences are advantageous as they provide insight into the sensitivity of storm surge levels relative to the total surge. When applied to wave height sensitivity, percent differences proved to be cumbersome, with some percent changes on the order of thousands of percent. Therefore, changes in wave heights are referenced as numerical changes throughout this section.

4.2 Sensitivity to Bottom Friction

Changes in wave heights due to increased bottom friction are shown in Figure 16. Within the marsh, wave heights are reduced for all configurations of increased bottom friction. Incoming peak wave periods ranged between 8 and 13 seconds, and peak incident wave heights ranged between 4.0 and 10.3 m (as shown in Table 4). As provided for peak surge, a metric was established to classify storms according to their wave action. This was established as wave potential (H_{base}), determined by calculating

the average peak significant wave height within the 400 km^2 marsh area for the base scenario. It should be noted that due to breaking and bottom friction dissipation, this wave potential is substantially lower than the incident wave height (see Table 4). Through this parameter, results are ordered in Figure 16 in a way that depicts the effects of increasing average wave heights within the marsh. This also coincides with the sequence of storms in terms of incident wave heights (ranging from 4.0 m to 10.3 m) entering the marsh. This illustrates that reductions in wave heights are most evident for storms of high wave height potential. For the three storms of lowest wave height potential (H_{base} = 0.2, 0.6, and 1.4 m), wave height reductions range between 0.1 and 0.8 m for bottom friction of n = 0.035. With increasing wave potential, these reductions become more dramatic. For example, the bottom friction of n = 0.035 incurs a minimum 1.2 m decrease in wave heights for the three storms of high wave potential (H_{base} = 2.0, 2.6. and 3.0 m). For all cases, changes in significant peak wave height outside the limits of the marsh are negligible (less than 0.2 m).

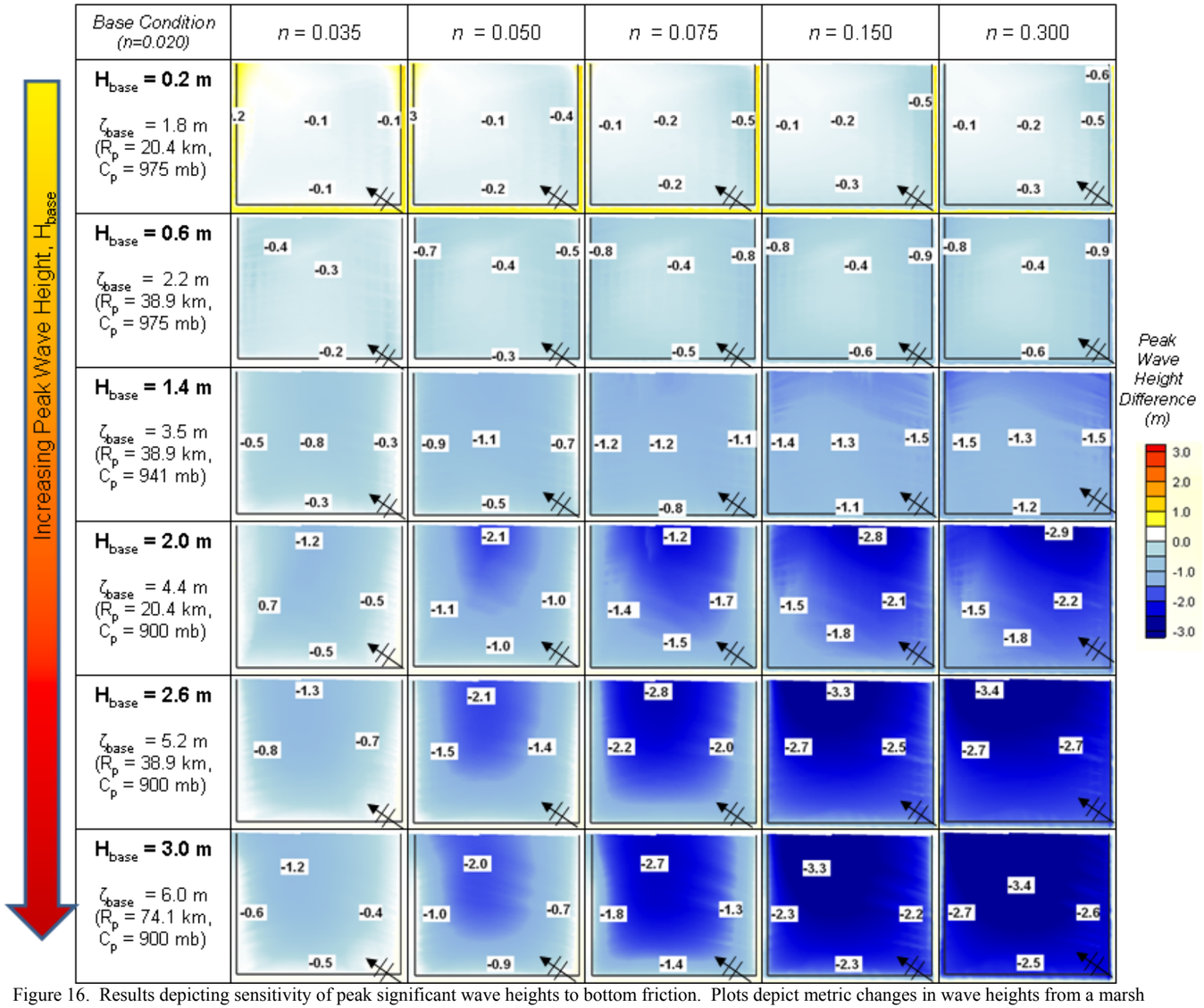

Figure 16. Results depicting sensitivity of peak significant wave heights to bottom friction. Plots depict metric changes in wave heights from a marsh characterized by a Manning'*n* of 0.020. Black lines represent marsh boundaries, with the coastline oriented at the top of each plot. Hot colors indicate wave height increases while cool colors indicate wave height decreases. Rows represent each storm condition, increasing in wave potential from top to bottom. Arrows indicate dominant wave direction.

To gain insight into the effects of wave setup and set-down, ADCIRC results for setup induced by wave radiation stress were analyzed. These results indicate that waves are breaking on the seaward marsh boundary, inducing relatively small wave heights within the marsh, as depicted in Figure 17. A setdown of peak water levels is noted prior to the breaking point, slightly seaward of the marsh. A setup of the peak water surface elevation exists landward of this breaking point, within the marsh. Peak water levels for the bottom friction base case configuration (Manning's *n* of 0.020, marsh elevation at +0.5 m) are increased by approximately 0.4 m due to wave setup, and 0.1 m due to wave set-down. Additionally, adjacent to the grid boundary exists a narrow band of wave setup, arising from wave breakage in the nearshore region at the coastline.

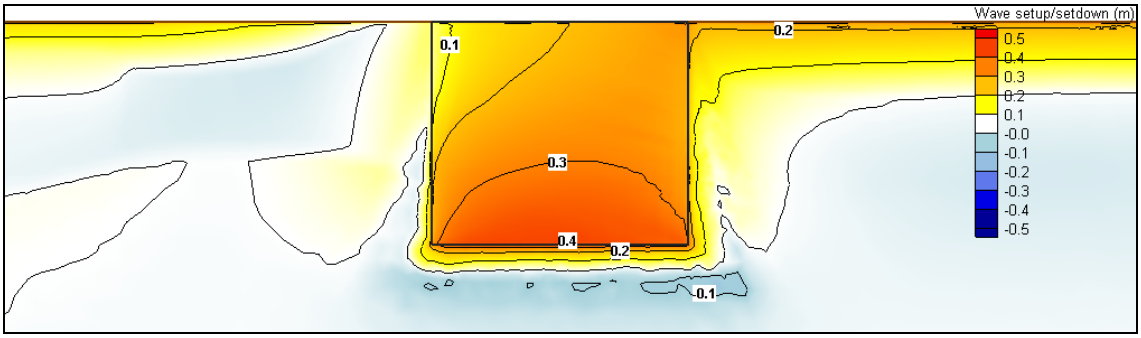

Figure 17. Representative wave setup/setdown, as calculated for Storm 3 over grid MAN1. Hot colors indicate areas of wave setup while cool colors indicate wave setdown.

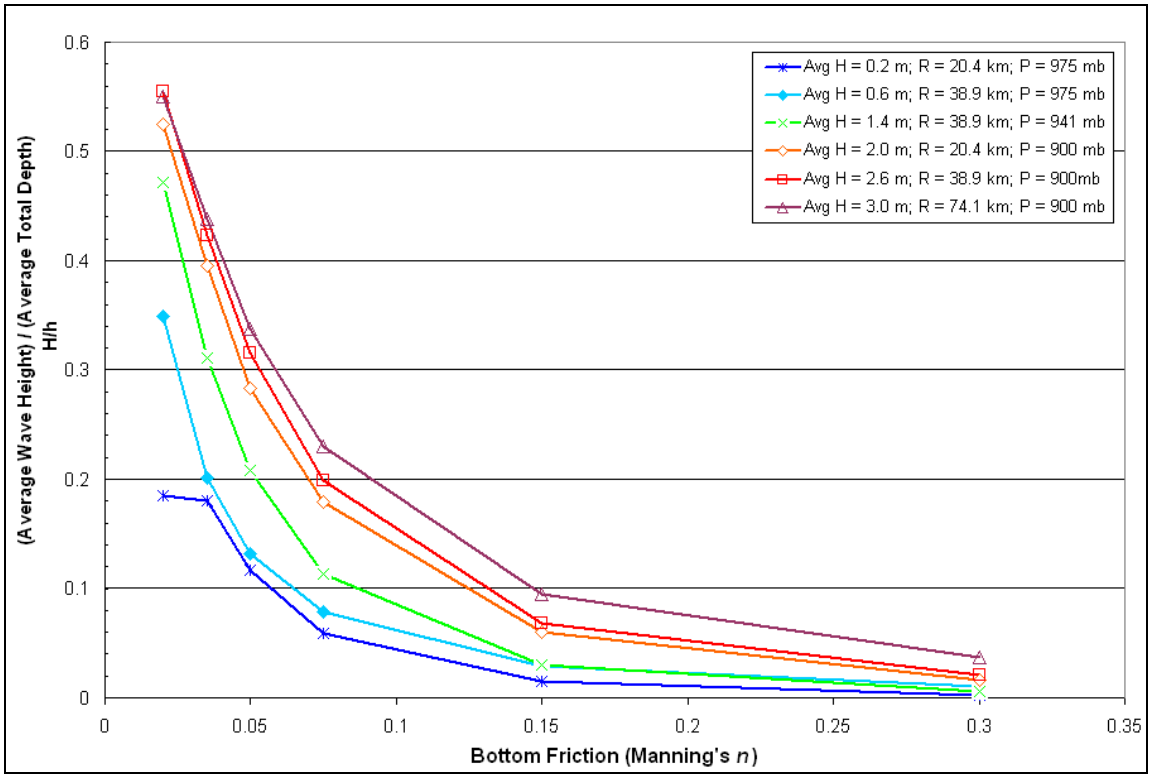

Figure 18. Ratio of peak wave height to total average depth as a function of bottom friction.

Figure 18 illustrates the relationship between the ratio of average peak significant wave height within the marsh to total water depth (H_{base}/h) as a function of bottom friction (Manning's n). This plot indicates that as bottom friction increases, wave height becomes smaller in comparison to total depth. As expected, wave heights are being reduced significantly due to increased bottom friction, following an exponential decay. As bottom friction increase to the maximum value of $n = 0.300$, a common value of H_{base}/h is approached, representing a point of maximum wave height reduction due to bottom friction.

The relationship between Ursell parameter for peak significant incident wave height and bottom friction is depicted in Figure 19. The Ursell parameter is given by:

$$U_R = \frac{HL^2}{h^3} \tag{4.1}$$

Through the calculation of Ursell parameter based on peak incident wavelength, average wave height within the marsh, and average depth within the marsh, a convergence is observed in Figure 19 based on the Manning's *n* value of the marsh.

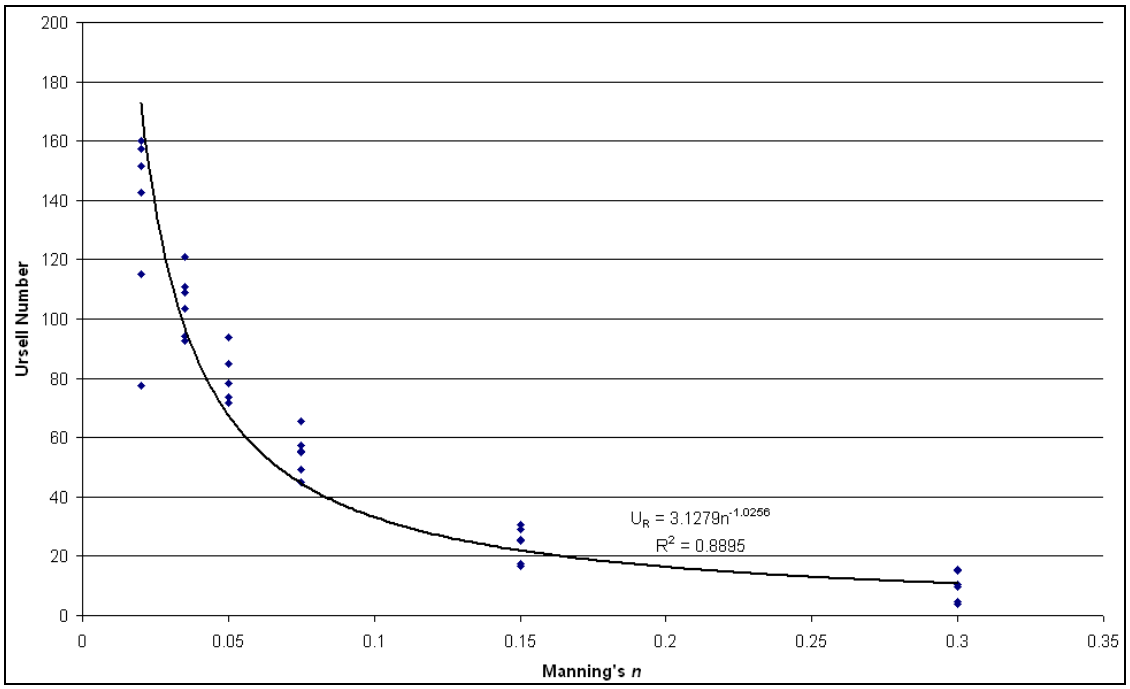

Figure 19. Manning's *n* versus Ursell parameter.

A best-fit line is derived to predict average wave height within the marsh based on the relationship between the Ursell parameter and the Manning's *n* factor. Applying this best-fit equation and solving for H, Equation 4.2 provides a formula for predicting average wave height within the marsh based on Manning's *n*, incident wavelength (m), and flow depth:

$$H = 3.1279 n^{-1.0256} \frac{h^3}{L^2} \tag{4.2}$$

The accuracy of this relationship is presented in Figure 20, with an R^2 and root mean square error of 0.93 and 0.26 m, respectively.

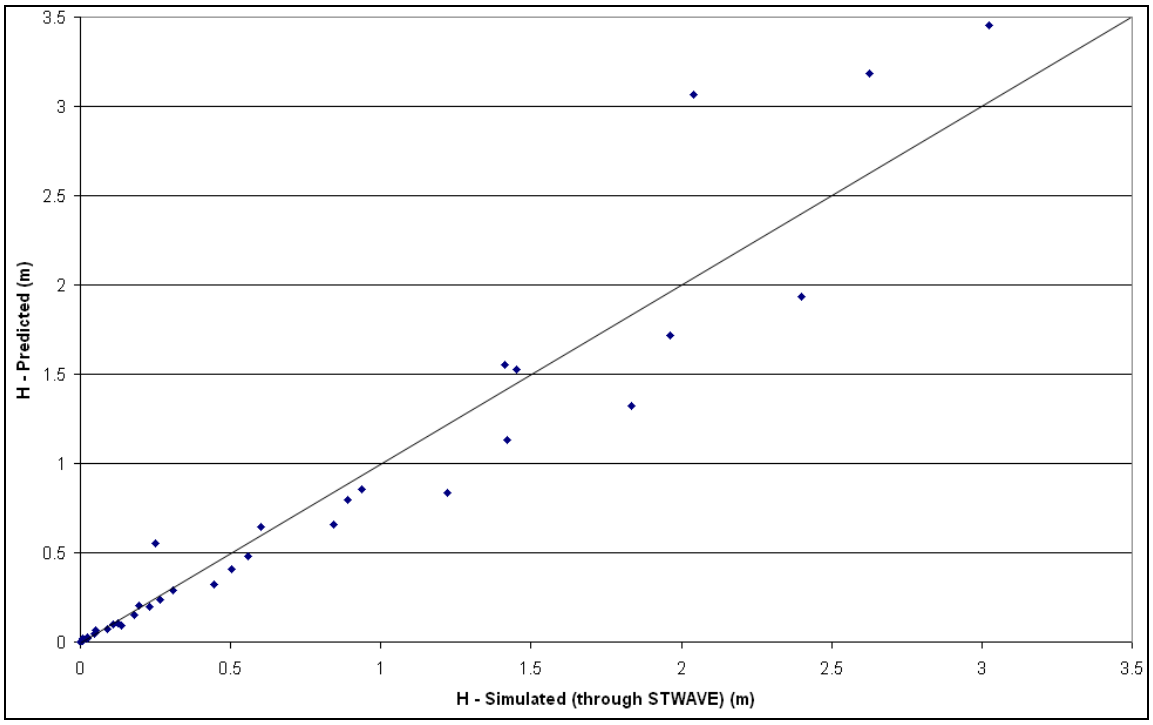

Figure 20. Predicting average wave height within the marsh based on Equation 4.2.

As expected, total surge levels (induced by wind stress and barometric pressure gradient) are generally decreased with increasing bottom friction. Figure 21 provides percent difference plots with respect to case MAN1, relating surge response to changes in bottom friction. Results are presented in order of increasing surge potential. Surge potential refers to the average peak surge within the square marsh feature, and provides a metric to classify storms according to the amount of surge they induce. In this thesis,

surge potential refers to the surge levels within the base case grid for a given marsh parameter of interest (bottom friction, elevation, or continuity). For the simulations investigating bottom friction, the base case (MAN1) is selected as the configuration with lowest bottom friction (n = 0.020). The base case surge potential (ζ_{base}) for these grids ranges between 1.8 and 6.0 m. As shown in Figure 21, when Manning's n is increased from 0.020 to 0.035, a decrease in peak surge levels of 35% is observed for the storm of lowest surge potential (ζ_{base} = 1.8 m). For the same storm (indicated on the first line of Figure 21), surge levels are further decreased, reaching a 50% surge decrease for a Manning's n of 0.050, ultimately reaching a 70% surge decrease for the upper bound value of Manning's friction coefficient (n = 0.300). As storm potential increases, bottom friction generally has less of an impact on peak surge levels. Figure 21 shows this effect, as surge decreases for a given Manning's n become less pronounced in the results presented at the bottom of the table. There is, however, one exception to this generalization. When comparing the storms of 3.5 and 4.4 m surge potential (third and fourth lines of Figure 21), it is evident that the storm of higher surge potential has a greater reduction in peak surge levels. This is a deviation from the overall increased sensitivity to changes in bottom friction due to decreased surge potential (as noted in all other results presented in Figure 21). For example, the 4.4 m surge potential event results in surge decreases of 10%, 25%, and 50% for a Manning's n of 0.035, 0.050, and 0.075, respectively. The storm of next-lowest surge potential (ζ_{base} = 3.5 m) results in 5%, 15%, and 40% decreases in surge for these same respective Manning's n cases. The

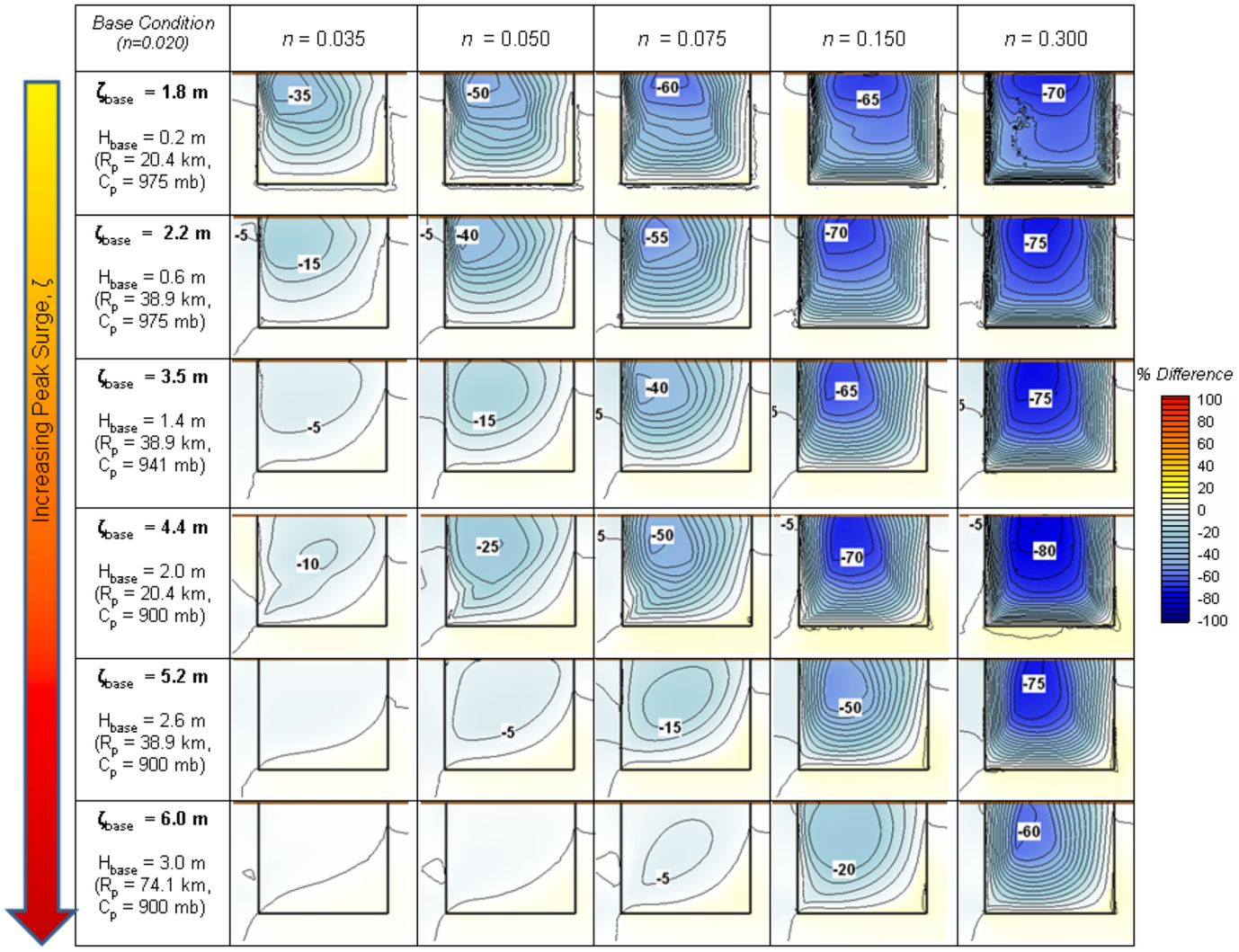

Figure 21. Results depicting sensitivity of surge levels to bottom friction. Plots depict percent changes in surge from a marsh characterized by a Manning's *n* of 0.020. Black lines represent marsh boundaries, with the coastline oriented at the top of each plot. Hot colors indicate surge increases while cool colors indicate surge decreases. Rows represent each storm condition, increasing in storm surge potential from top to bottom.

storm of 4.4 m surge potential features a pressure radius of 20.4 km and a minimum pressure of 900 mb, while the storm of 3.5 m has a pressure radius of 38.9 km, and minimum pressure of 941. This suggests that storm size is a secondary factor contributing to the marsh's ability to reduce storm surge, as the larger, weaker storm produces a surge less influenced by bottom friction than the stronger, smaller storm. Therefore, surge sensitivity to bottom friction (in terms of percent differences) is primarily affected by total water depth (surge potential), and secondarily affected by the extent of the alongshore distribution of surge. This is graphically depicted in Figure 22.

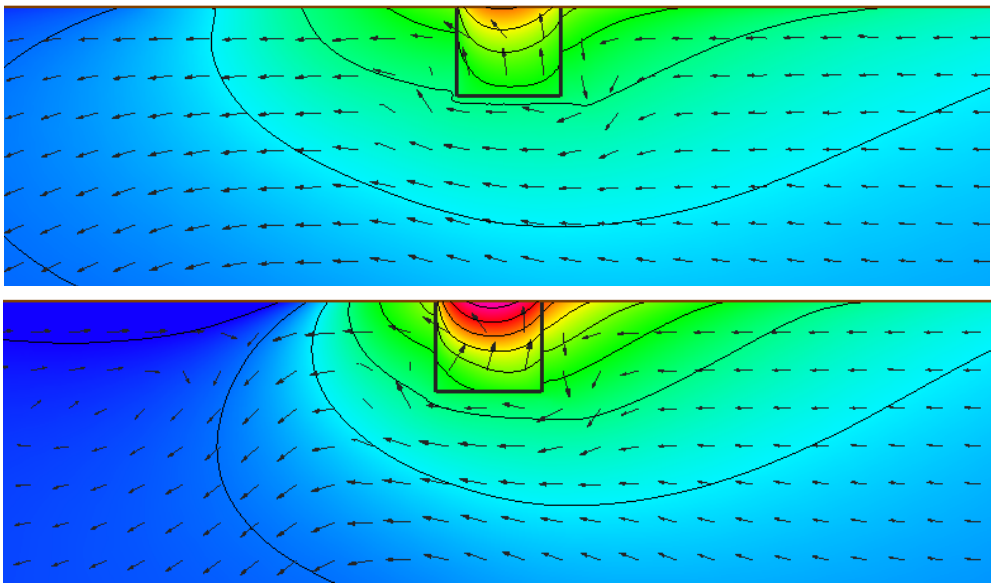

Figure 22. Instantaneous surge levels and velocity vectors at peak of the storms producing ζ_{base} of 3.5 m (Storm 4, top) and 4.4 m (Storm 1, bottom).

In areas outside of the marsh, (where bottom friction is held constant at $n = 0.020$ for all conditions), percent changes in surge are limited to +/- 10%. At each simulated hurricane landfall, velocities are predominantly oriented at a direction flowing from east

to west (due to the counterclockwise winds flowing around the core of the storm). As surge propagating in this direction experiences frictional resistance within the marsh, velocities are slowed, and a slight buildup of water levels (with respect to the base condition) is noted along the eastern edge of the marsh. Accompanying the increase in surge east of the marsh is a decrease in surge to the west of the marsh, also caused by the decreased velocities within the marsh. In this way, the marsh is a shoreline protrusion causing shadowing to the west and a buildup to the east at the landfall of a hurricane. As the hurricane moves northward, winds transition from easterly to westerly. Velocities react accordingly with a change in direction from westward flowing to eastward flowing. This reverses the previously mentioned buildup and shadowing effect. Therefore, as the hurricane is positioned landward of the marsh (to the north), there is an increase of water levels to the west and a decrease in water levels to the east. This translates to changes in the peak water levels (maximum water surface elevation observed at each node point at any given time step). The peak elevation percent difference plots (Figure 21) capture these effects. In all cases, peak water levels are increased southeast of the marsh by no more than 5%. Decreases in peak surge of 10% and less are noted to the west of the marsh for most of the results.

Figure 23 presents the most extreme percent surge reductions along the coast due to increased bottom friction for all six storm events. As shown in the lower lines in Figure 23 (blue and cyan lines), up to a Manning's *n* of 0.075 storms of low surge potential are associated with the greatest reductions in coastal surge levels. As surge potential increases, storms of moderate surge potential result in the greatest decreases

due to bottom friction (orange and green lines). Storms of greatest surge potential (red and purple lines) reveal a relationship between maximum surge reduction and bottom friction that has a relatively constant slope.

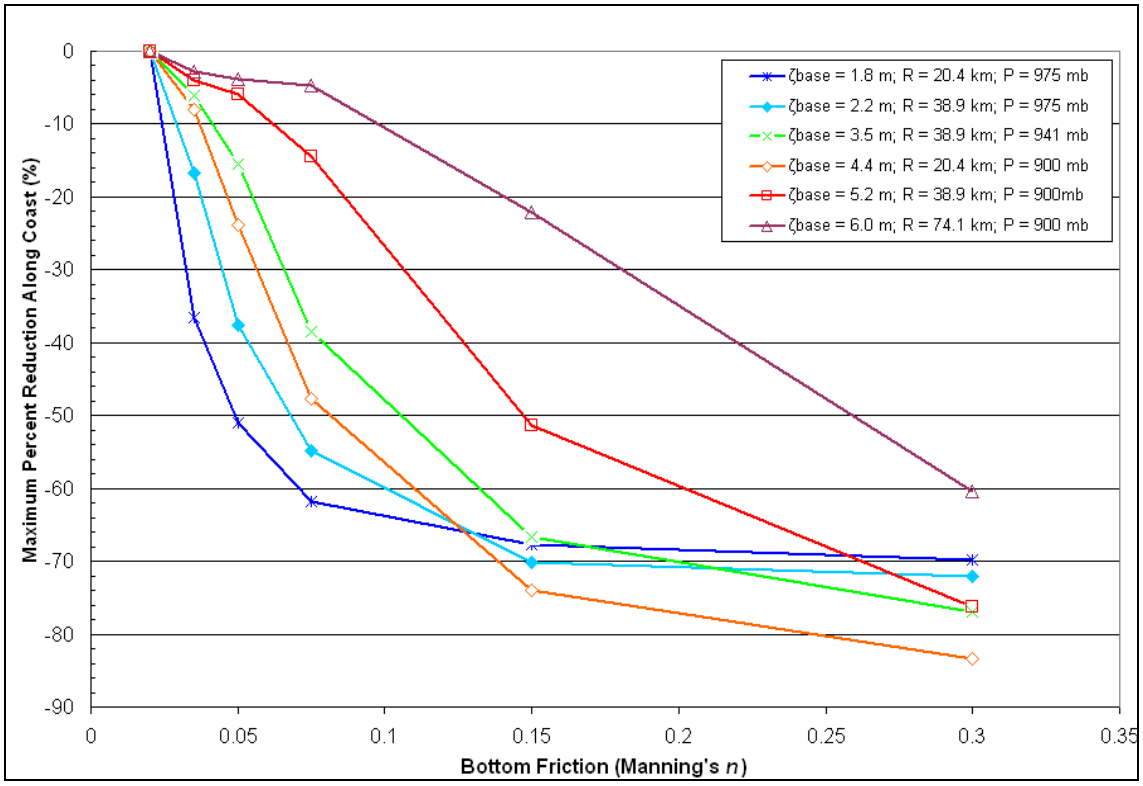

Figure 23. Relationship between minimum surge reduction along the coast and bottom friction.

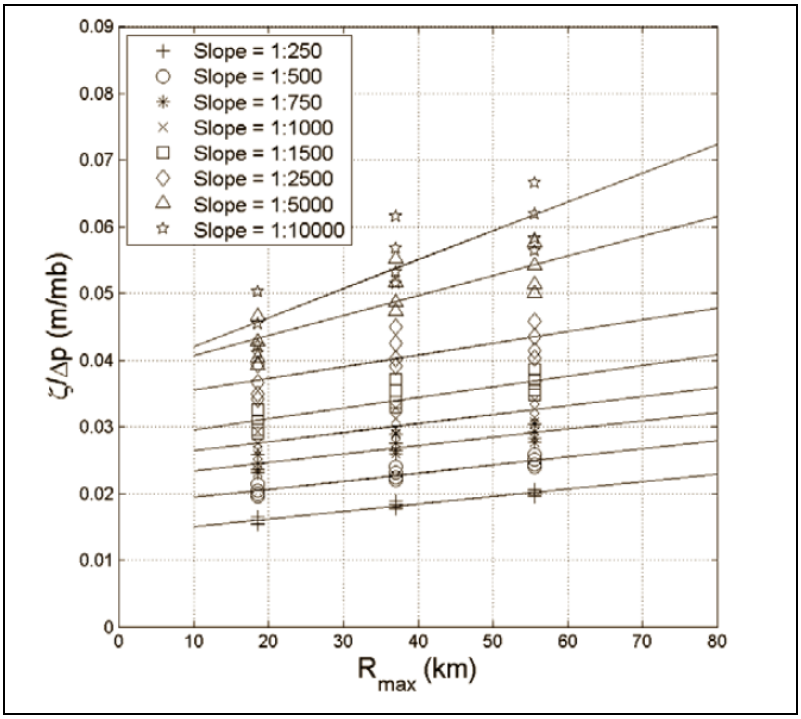

Figure 24. Linear relationships between peak surge at shoreline, pressure deficit, and storm pressure radius as determined by Irish *et al.*, 2008. (From *Irish et al.*, 2008).

To derive an equation based on Manning's *n* and storm parameters, peak depths based on ADCIRC simulation results were plotted based on the linear relationship between $(\zeta / \Delta p)$ and R_{max} as presented in *Irish et al*. (2008), as shown in Figure 24. This was achieved by taking the slope ($m_s = 1.34 \times 10^{-4}$) and y-intercept ($b_y = 0.02511$) of the best fit line for a bathymetry slope of 1:1000, and developing a characteristic dimensionless surge function, given by:

$$M = \frac{h/\Delta p}{m_s R_p + b_y} \tag{4.3}$$

In this equation, total depth (h) replaces the peak surge (ζ) used by *Irish et al*. (2008) in deriving linear relationships presented in Figure 24. This substitution is justified, as

peak surge referenced by *Irish et al.* (2008) is based on peak surge at the coastline of an idealized grid, where the total depth equals peak surge ($h = \zeta$). Figure 25 presents this parameter as a function of Manning's *n*.

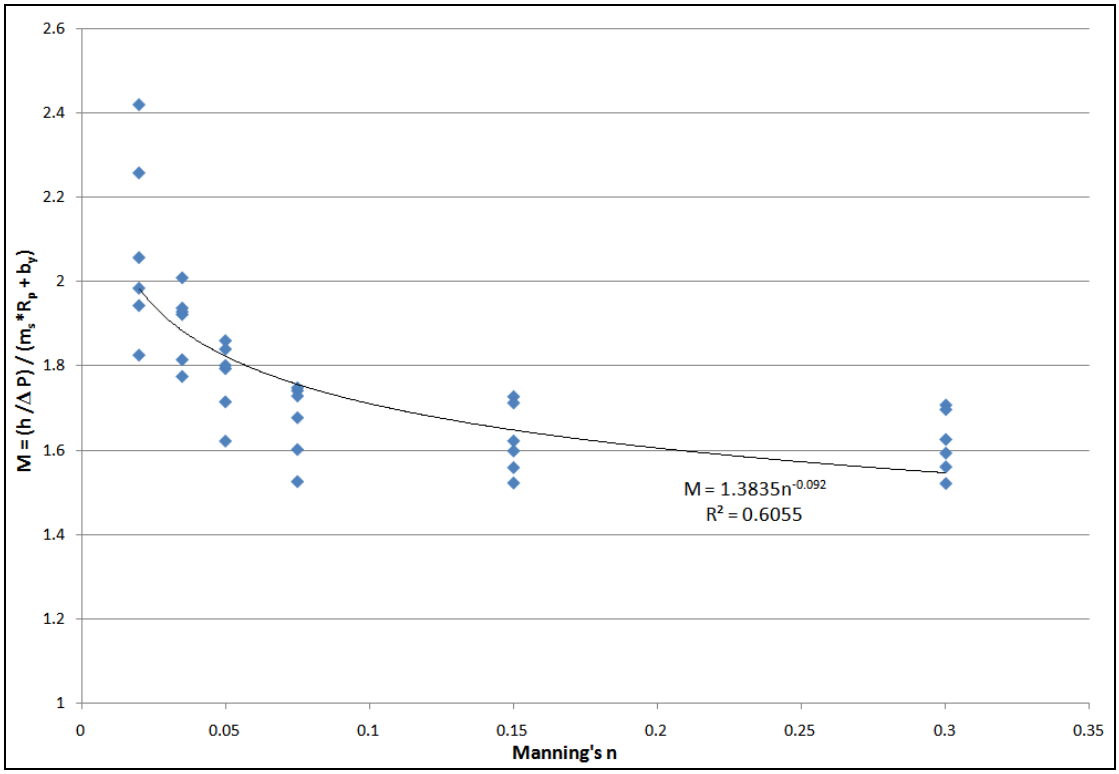

Figure 25. Relationship between *M* and Manning's *n*, with exponential best fit equation.

The best-fit equation presented in Figure 25 may be solved for h, yielding an equation for peak water depth within the marsh as a function of marsh Manning's *n* and storm parameters (Δp and R_p):

$$h = 1.3835 n^{-0.092} \Delta p (m_s R_p + b_y) \tag{4.4}$$

Figure 26 depicts peak water depths observed through ADCIRC simulations compared with peak water depths calculated through Equation 4.4. Surge predicted by Equation 4.4 has an R^2 value of 0.96 and a root mean square error of 0.27 m.

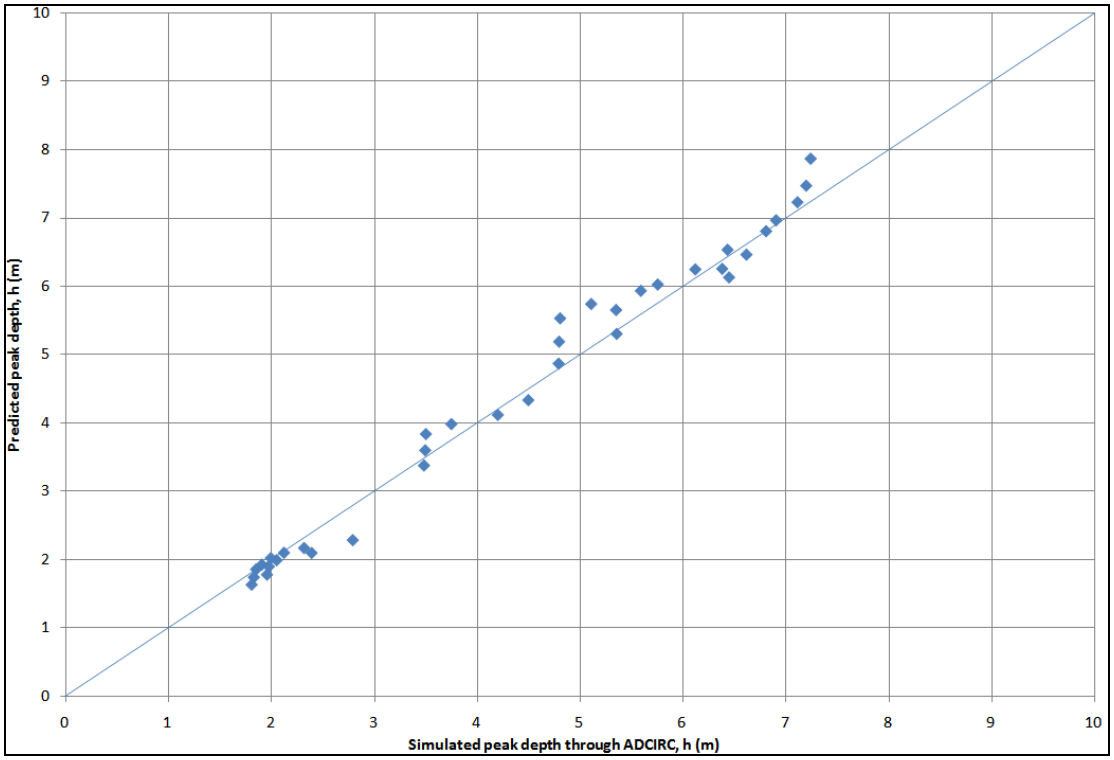

Figure 26. Predicted values of peak water depth based on Equation 4.4 as compared with observed peak water depths through ADCIRC.

4.3 Sensitivity to Marsh Elevation

Decreased marsh elevation results in increased wave heights, as shown in Figure 27. A uniform response is revealed in this figure for storms of varying potential. In this figure, peak significant wave height changes are depicted in meters, with storm-induced wave potential becoming increasingly large from top to bottom. The uniform increase in peak significant wave heights is a product of the depth-dependency of the waves

propagating through the marsh. Depth-limited, deep-water waves approaching the marsh become dependent upon the Miche criterion (Equation 3.10) for breaking as they transition to the shallow water within the marsh. For the storm of greatest wave potential, wave heights are increased by between 0.4 and 0.5 m for a marsh at 0.2 m below sea level. As the marsh is degraded to 3.0 m below sea level, peak significant wave heights induced by this storm are more substantially increased, by between 1.9 and 2.1 m.

Figure 28 graphically illustrates changes in the ratio of wave height to total depth as the seabed is lowered. As shown in the lower lines of Figure 28, storms of low wave height potential induce small wave heights compared to total depth. A constant H_{base}/h is approached as the seabed deepens, representing the depth-dependency of the wave heights. Storms of moderate to extreme wave potential, shown by the upper lines in Figure 28, result in a consistent H_{base}/h value over varying seabed conditions, illustrating that for these storms, wave height is limited by depth for all marsh configurations.

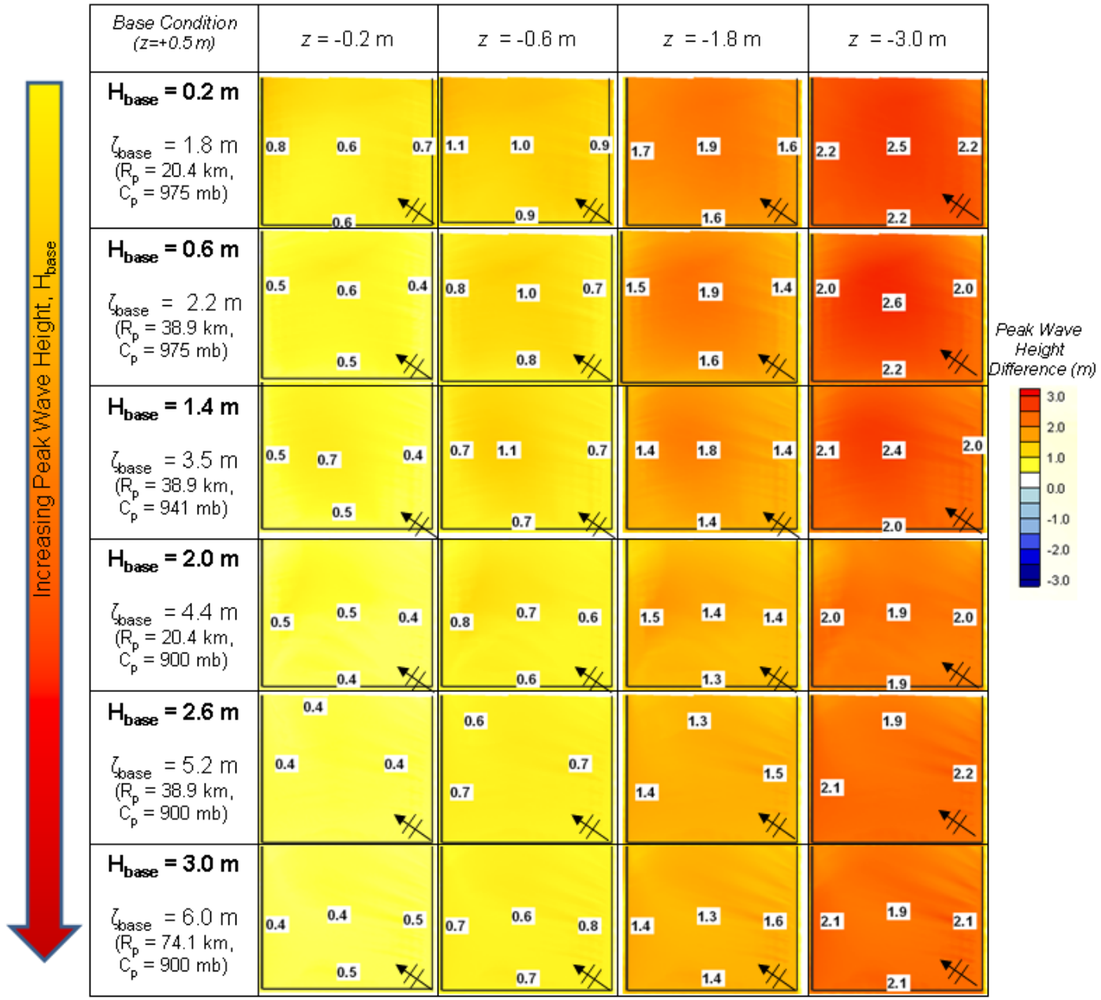

Figure 27. Results depicting sensitivity of peak significant wave heights to marsh elevation. Plots depict metric changes in wave heights from a marsh positioned at 0.5 m above sea level. Black lines represent marsh boundaries, with the coastline oriented at the top of each plot. Hot colors indicate wave height increases while cool colors indicate wave height decreases. Rows represent each storm condition, increasing in wave potential from top to bottom. Arrows indicate dominant wave direction.

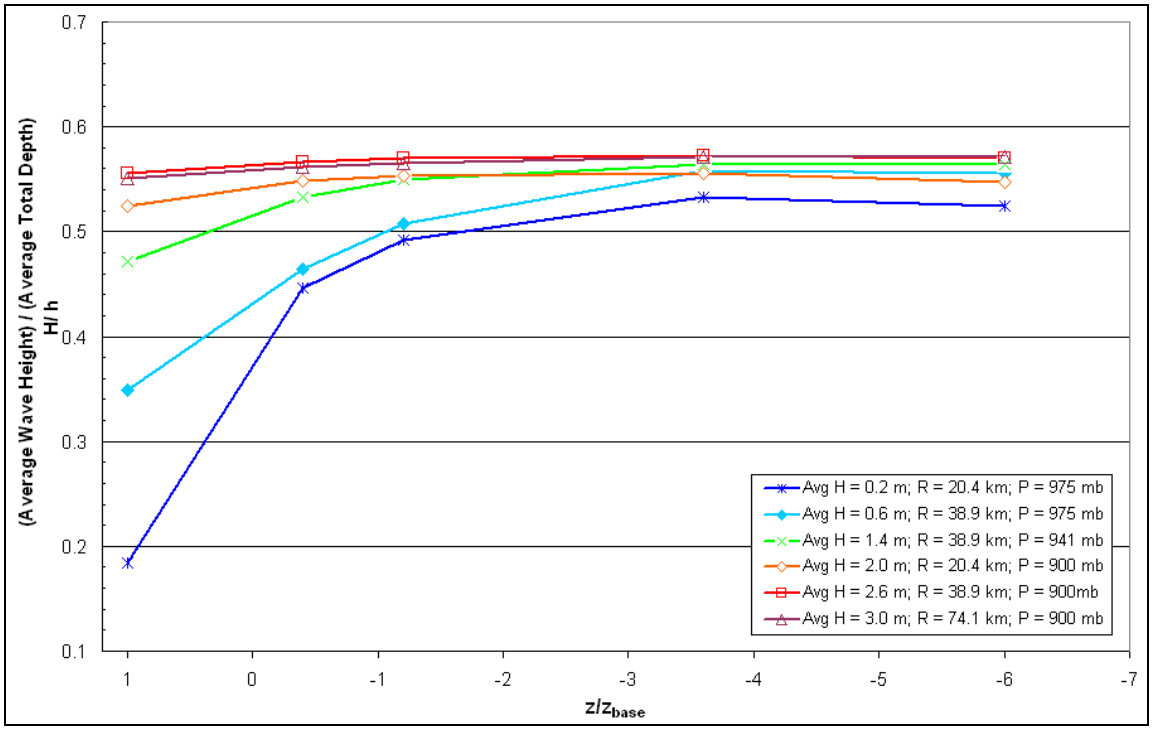

Figure 28. Ratio of seabed elevation (z) to base case elevation (z_{base}) versus ratio of average peak significant wave height to total depth within the marsh (H_{base}/h).

In general, modeling results show that decreases in marsh elevation result in decreases in surge. This is due to the inversely proportional relationship between surge and total water depth, as shown in the momentum balance (Equation 2.2). Figure 29 depicts the surge response to increasing depths in terms of percent differences. Storms of high surge potential are shown in the lower lines of the figure, while storms of low surge potential are depicted in the upper lines. These plots depict percent changes in peak surge levels from a base condition of marsh elevation at 0.5 m above mean sea level. Seabed lowering induces an overall reduction in peak surge level for most storm scenarios. An exception to this is the storm of lowest surge potential (ζ_{base} = 1.8 m),

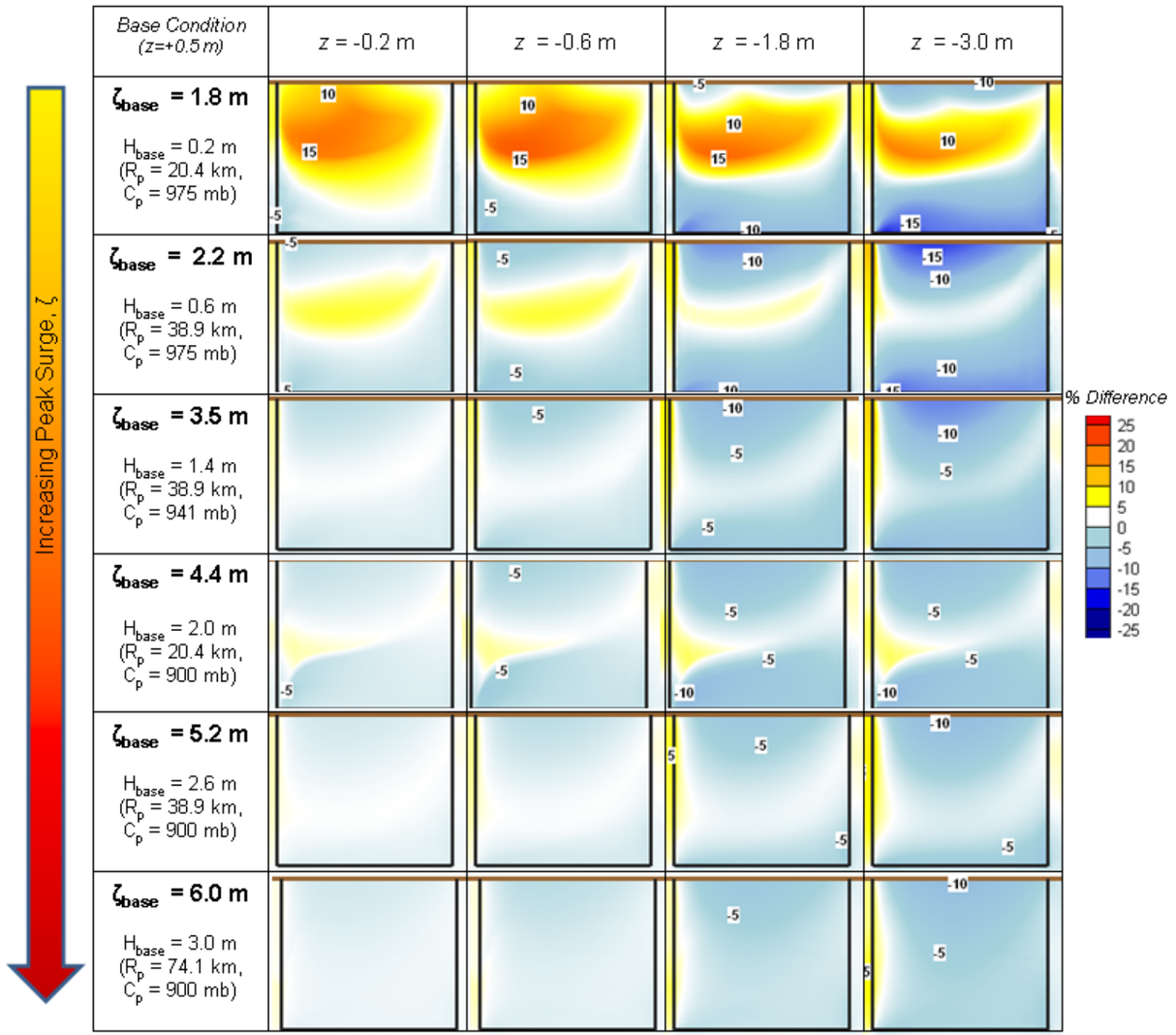

Figure 29. Results depicting sensitivity of surge levels to marsh elevation. Plots depict percent changes in surge from a marsh at 0.5 m above sea level. Black lines represent marsh boundaries, with the coastline oriented at the top of each plot. Hot colors indicate surge increases while cool colors indicate surge decreases. Rows represent each storm condition, increasing in storm surge potential from top to bottom.

shown on the first line of Figure 29. For example, an increase of 15% is noted within the marsh feature as it is lowered to 0.2 m below sea level. The increases in peak surge associated with increased depth are a result of bottom friction effects in the base case scenario. The base case marsh (at 0.5 m above sea level) remains dry until surrounding levels of surge reach 0.5 m. As surge inundates the marsh, it is greatly influenced by bottom friction due to the low total depth across the marsh. In the experimental cases (marsh elevation at 0.2, 0.6, 1.8, and 3.0 m below mean sea level), the marsh is fully inundated before storm landfall. Surge propagating across this area is unconstrained by a land feature, and ultimately less influenced by bottom friction due to a greater total depth. Therefore, for low surge potential events, surge is increased as the seabed is lowered because bottom friction plays a smaller role in a water column of greater depth. This effect dissipates as total depth is increased with increasing surge potential. Areas of slight surge increases (less than 5%) are visible in the storm of second-lowest surge potential, but for most other storms, a uniform decrease in surge is noted within the marsh. Surge at the coast is increased by no more than 10% for the marsh elevations of 0.2 and 0.6 m below sea level. As seabed elevation is further lowered to 1.8 and 3.0 m below sea level, decreases along the coast by as much as 10% are observed. Decreases in coastal surge levels are most substantial for the storm of second lowest surge potential (ζ_{base} = 2.2 m). Associated with this storm are coastal decreases in surge of as much as 15% for a marsh lowered to a depth of 3.0 m.

A three-part effect is notable within the marsh due to lowered marsh elevation. In most of the results (particularly those of moderate to low surge potential), surge is lowered along the coast, raised within the marsh, and decreased along the seaward edge of the marsh. Areas of lowered peak surge along the landward and seaward edge of the marsh are a result of the inverse relationship between surge and depth. The increased peak surge within areas central to the marsh is a result of increased conveyance of water across the marsh boundary due to lowered marsh elevation. This three-part effect is most dramatic in storms of low surge potential. For example, from the coastline to the edge of the marsh, surge is decreased by 10%, increased by 10%, and once again decreased by 15% due to a lowered seabed to 3.0 m below sea level in the case of the storm of lowest surge potential (ζ_{base} = 1.8 m). Surge levels become less sensitive to lowered bathymetry as surge potential increases. This is depicted in Figure 30, which relates the percent change in maximum peak surge along the coast to marsh elevation. The relationship between coastal surge sensitivity and marsh elevation approaches a constant slope as surge potential is increased. As shown by the red and purple lines in Figure 30, a nearly linear relationship exists between maximum percent change along the coast and marsh elevation for all but the lowest wave potential cases.

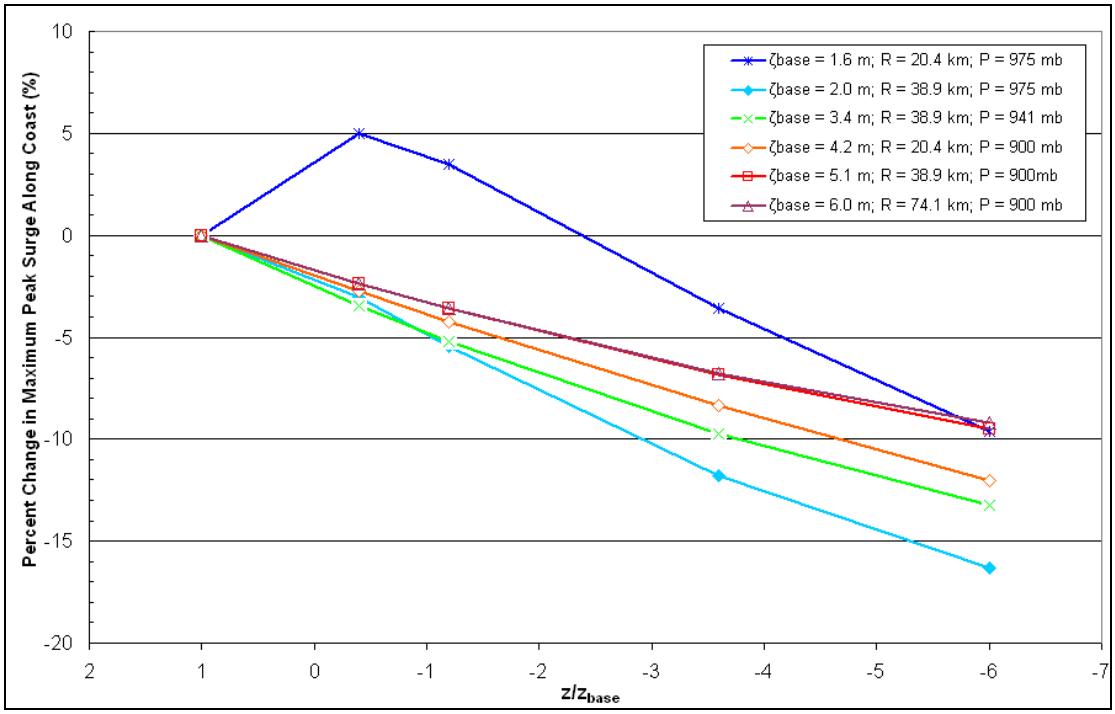

Figure 30. Percent changes in coastal peak surge due to seabed lowering.

Data presented by *Irish et al*. (2008) is used to determine an equation for use in predicting surge over the 20km by 20km seabed feature, given seabed elevation (z) and storm parameters (R_p and Δp). Equation 4.3 is revisited to collapse ADCIRC results on a best-fit line through the use of the M parameter (Equation 4.3). Figure 31 presents these results, as similarly done for the bottom friction results in Figure 25.

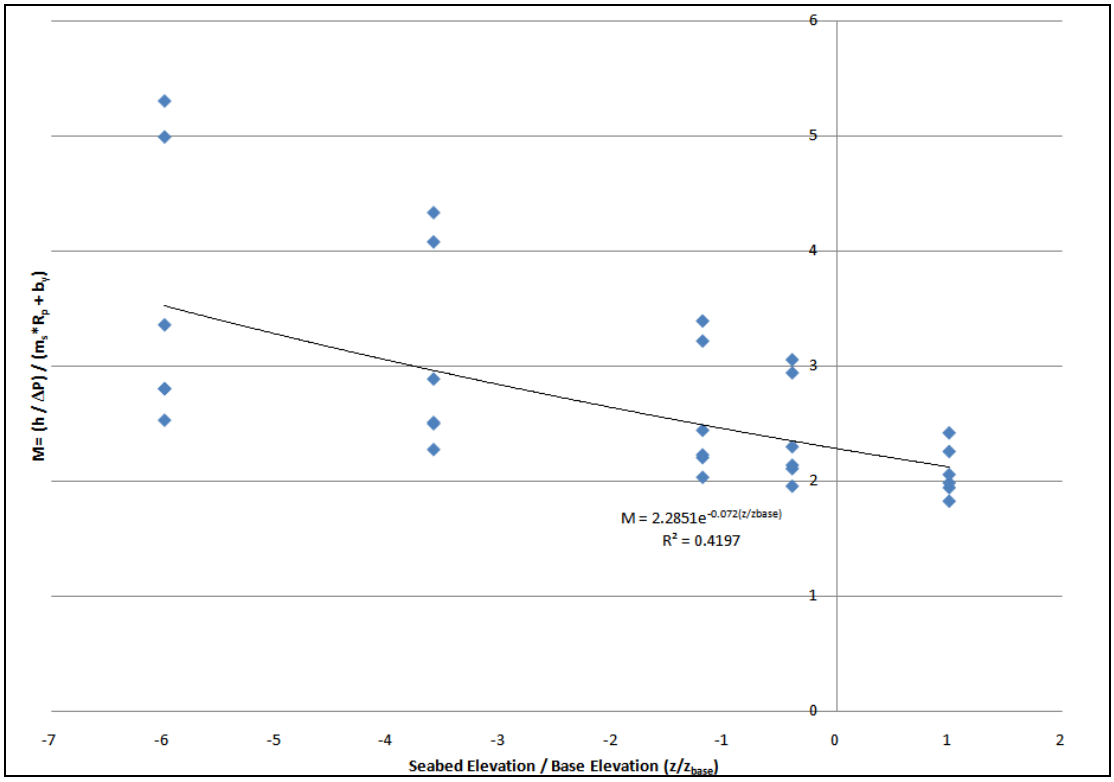

Figure 31. Relationship between *M* and sea bed elevation (*z*), with exponential best fit equation.

Solving the best fit equation shown in Figure 31 yields a relationship between peak surge (at the coast), storm parameters, and seabed elevation:

$$h = 2.2851e^{0.144z}(mR_p + b_y)\Delta p \tag{4.5}$$

The accuracy of this equation in predicting peak surge as simulated by ADCIRC is shown in Figure 32. The comparison has an R^2 value of 0.94 and a root mean square error of 1.4 m.

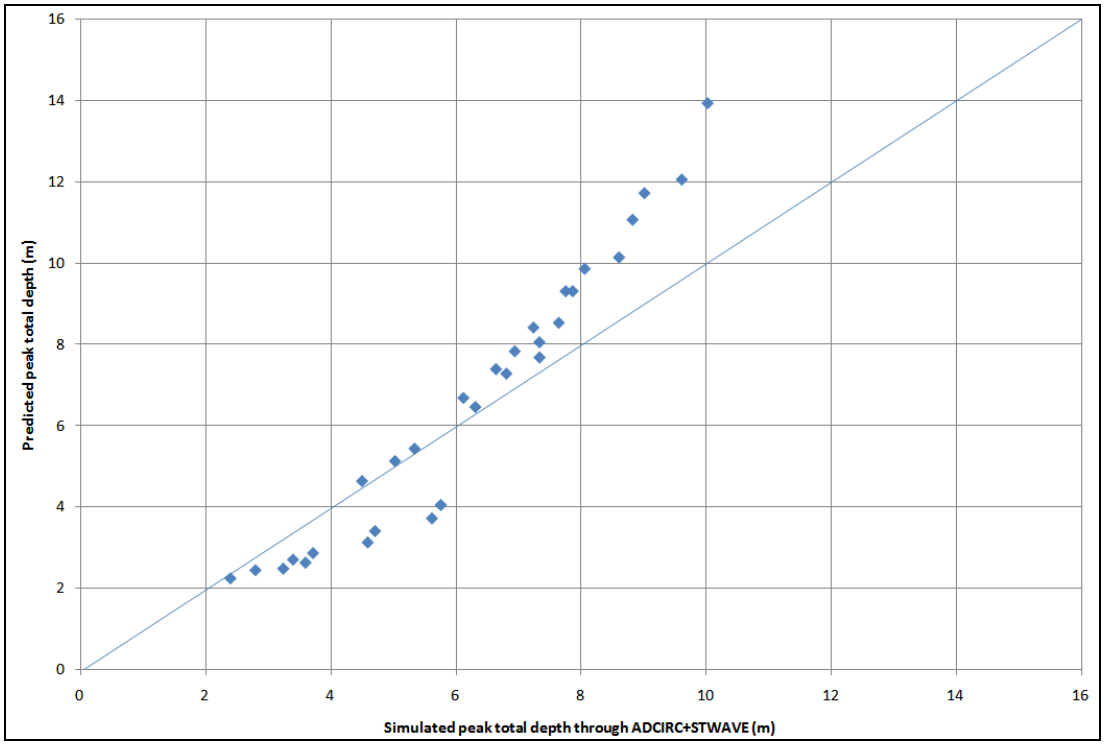

Figure 32. Predicted values of peak surge based on Equation 4.5 as compared with peak surge observed through ADCIRC.

4.4 Sensitivity to Marsh Continuity

In the analysis of wave and surge sensitivity to marsh continuity, results from grids having continuity of 50% (CON2) and 75% (CON1) are compared with a grid having a continuity of 100% (BASE). Each of the CON1, CON2, and BASE grids feature a marsh Manning's *n* of 0.035 (tall grass) and an open-water Manning's *n* of 0.020 (sand). The CON1-2 and BASE grids are identical with the exception of the channels providing a non-continuous marsh in the CON1-2 grids. In essence, this

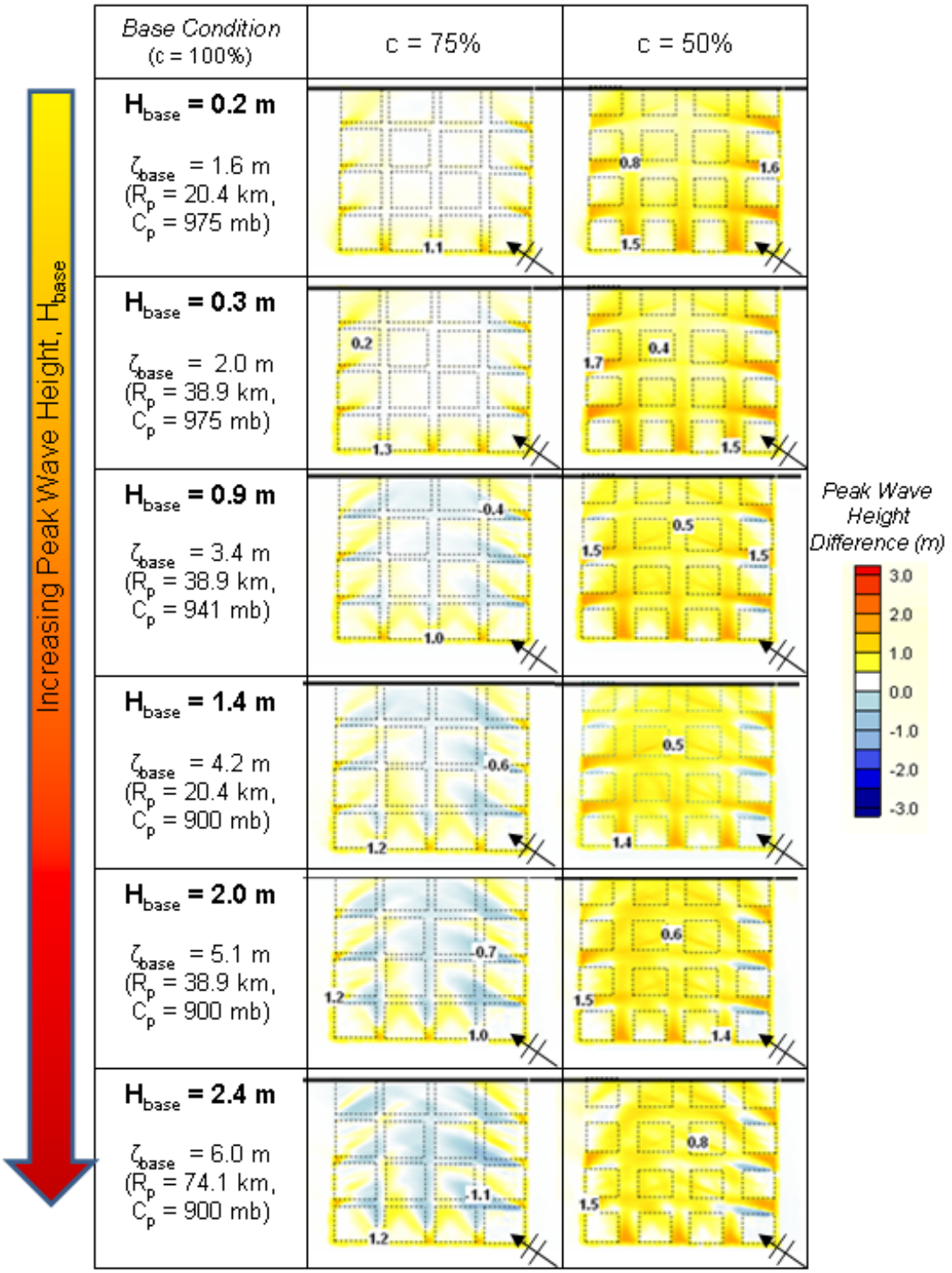

Figure 33. Results depicting sensitivity of peak significant wave heights to marsh continuity. Plots depict metric changes in wave heights from a marsh of c = 100% continuity. Black lines represent marsh boundaries, with the coastline oriented at the top of each plot. Hot colors indicate wave height increases while cool colors indicate wave height decreases. Rows represent each storm condition, increasing in wave potential from top to bottom. Arrows indicate dominant wave direction.

comparison focuses on the surge and wave sensitivity to channels delineating a marsh into smaller segments. As shown in Figure 33, sharp increases in peak significant wave heights are observed within the marsh channels of the non continuous marsh configurations. These wave height increases range between 0.2 and 1.7 m, becoming more noticeable in the marsh of 50% continuity. Increases in wave height are due to the deeper depths within the channels, allowing waves to propagate into the marsh with less energy loss by breaking and bottom friction damping.

Associated with the increases in peak significant wave height are small pockets of localized decreases in wave height within the channels. These decreases in wave height are most noticeable for the 75% continuous marsh during the three storms of greatest wave potential (H_{base} = 1.4, 2.0, and 2.4 m). These decreases in wave heights are a result of refraction and shadowing as waves travel around the internal corners of the marsh segments. Such refraction and shadowing effects are less noticeable in the 50% configuration, as the wider channels allow more wave energy to enter the marsh, resulting in a wave climate less prone to wave transformation. Figure 34 depicts these effects graphically.

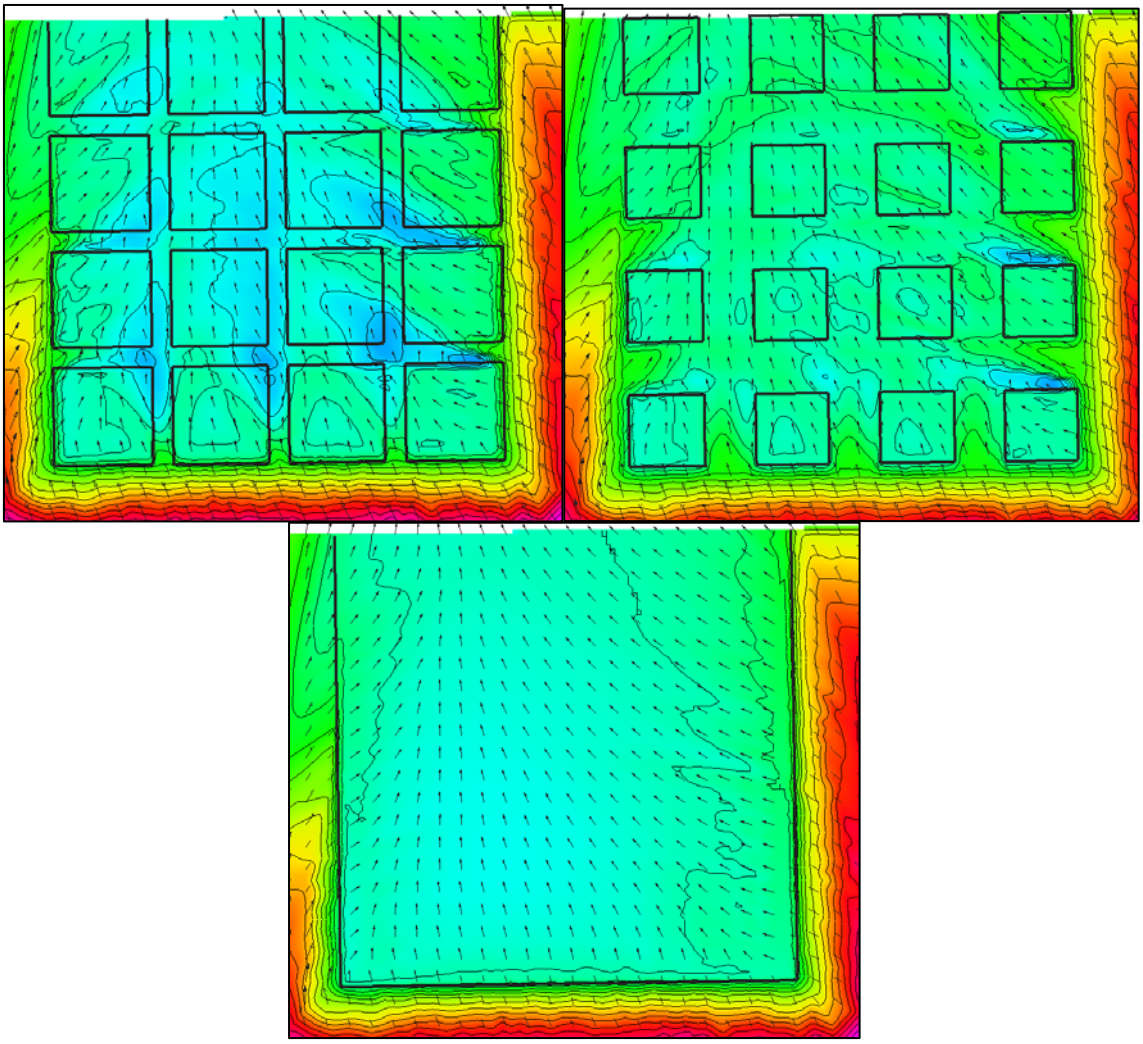

Figure 34. Wave rays and peak significant wave height within the marsh of 75% (top left), 50% (top right), and 100% (bottom) continuity for the storm of greatest surge and wave potential (Storm 3).

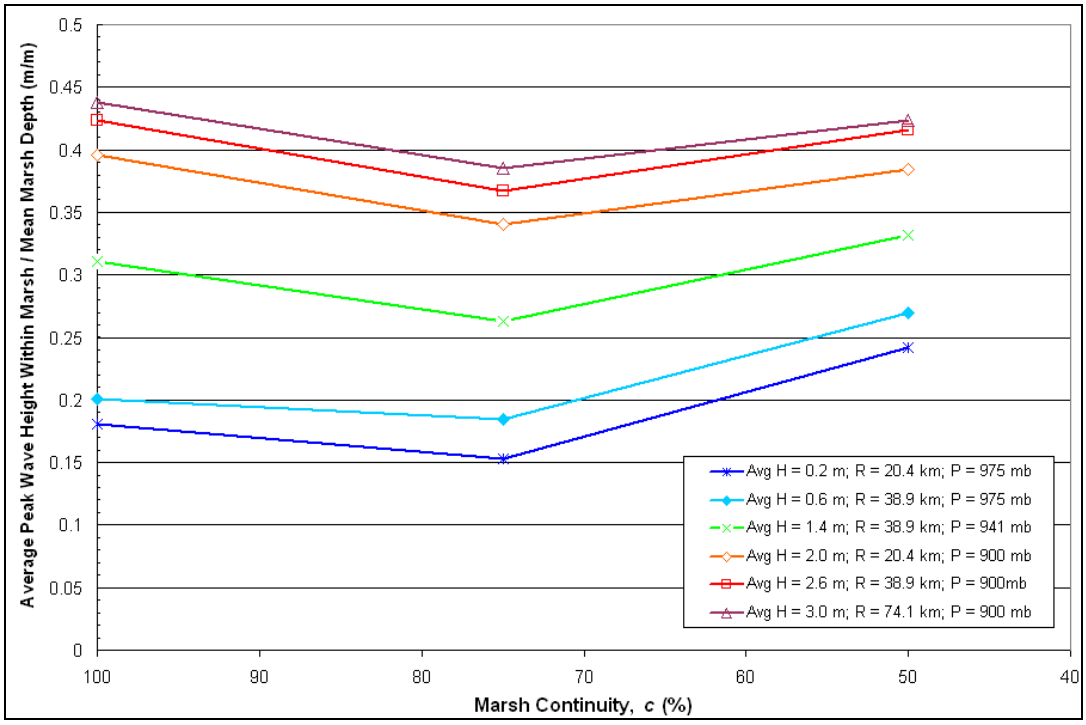

Figure 35. Ratio of average peak significant wave height to mean depth within the marsh due to decreases in marsh continuity.

Figure 35 shows the relationship between the ratio of average peak significant wave height to depth, and marsh continuity. Average wave heights within the marsh are slightly decreased in comparison with depth as continuity is decreased from 100% to 75%. However, as continuity is further decreased to 50%, average peak wave heights are once again increased in comparison with depth, as a result of transmission through the widened marsh channels. For the storms of lowest surge potential (blue, cyan, and green lines) the wave height to water depth ratio for 50% continuity is increased to levels that are greater than that associated with 100% continuity. This indicates that the increased wave transmission through the channels is dominating for storms of low wave potential. However, for the storms of large wave potential, wave height to water depth

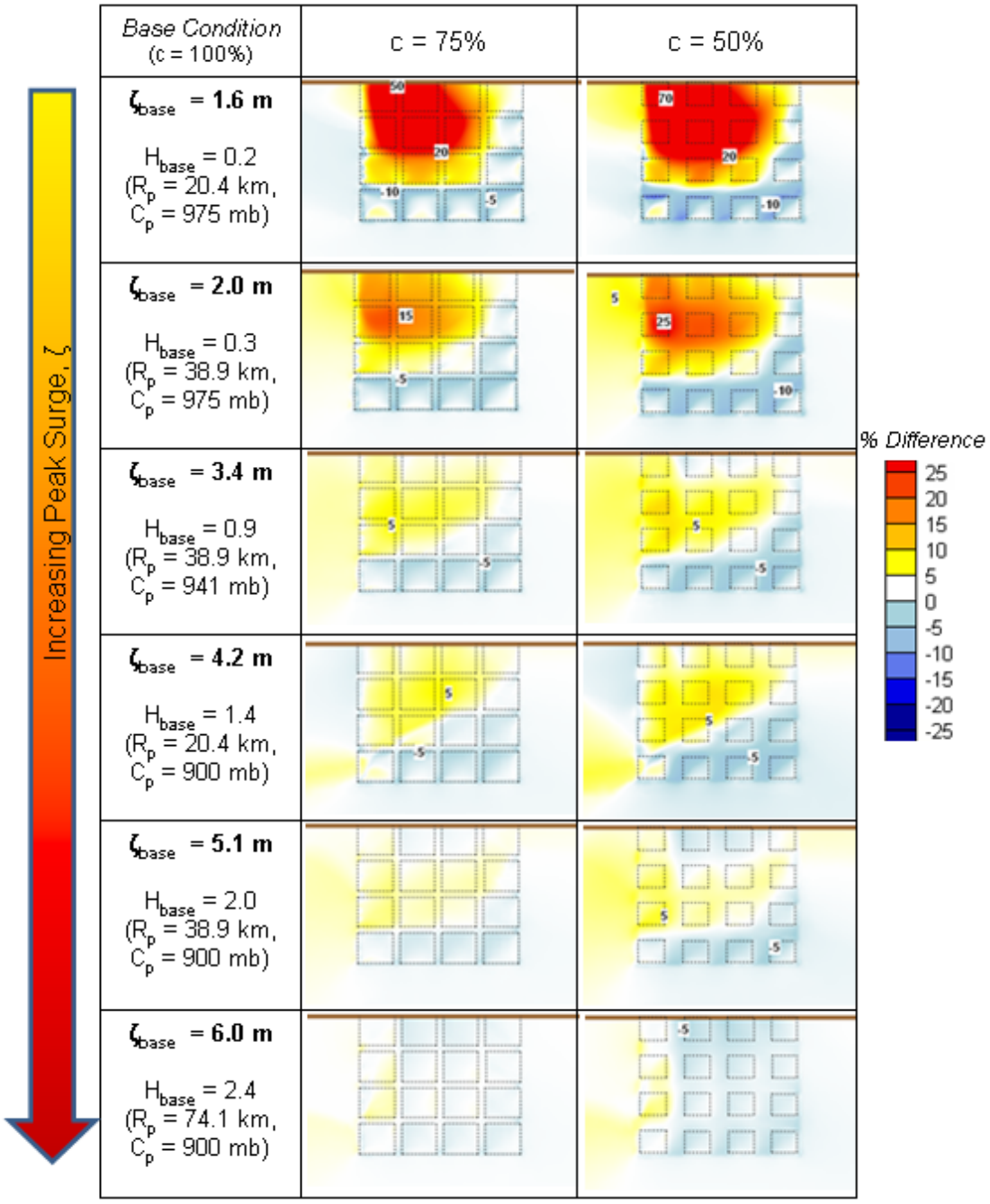

Figure 36. Results depicting sensitivity of surge levels to marsh continuity. Plots depict percent changes in surge from a marsh having a continuity of *c* = 100%. Black lines represent marsh boundaries, with the coastline oriented at the top of each plot. Hot colors indicate surge increases while cool colors indicate surge decreases. Rows represent each storm condition, increasing in storm surge potential from top to bottom.

ratio remains lower than observed for 100% continuity, indicating that refraction effects are dominating for these storms.

Percent changes in surge due to increased marsh continuity are dominated by conveyance of water into and out of the marsh, as shown in Figure 36. Due to decreased marsh continuity of c = 75%, coastal surge is increased by as much as 50% in the case of the storm of lowest surge potential (ζ_{base} = 1.6 m). A further reduction in continuity to c = 50% results in a 70% increase in coastal peak surge. Increases in peak surge along the coast are a result of the transmission of water through the marsh channels. As continuity is further decreased, marsh channel width accordingly increases, resulting in greater conveyance of water into the coastal boundary of the marsh. Velocity vectors depicting this effect are presented in the upper pane of Figure 37. Increasingly wide channels within the marsh also usher in the opportunity for water to flow out of certain areas within the marsh, as depicted in the lower portion of Figure 37. In comparing the upper and lower pane of Figure 37, it is shown that while the storm is approaching (upper pane of Figure 37), water is being conveyed through the marsh, from east to west. After storm landfall, outward flow is observed, diverging from the marsh's center to the east and west. This is also evidenced in the peak surge decreases along the seaward edge of the marsh, especially prominent in the storm of lowest surge potential (first line of Figure 36). In this scenario, a 5 to 10% decrease in surge is noted within the marsh channels due to the shifting of surge water from the seaward marsh boundary to the coastal marsh boundary. As surge potential increases, these decreases become less pronounced.

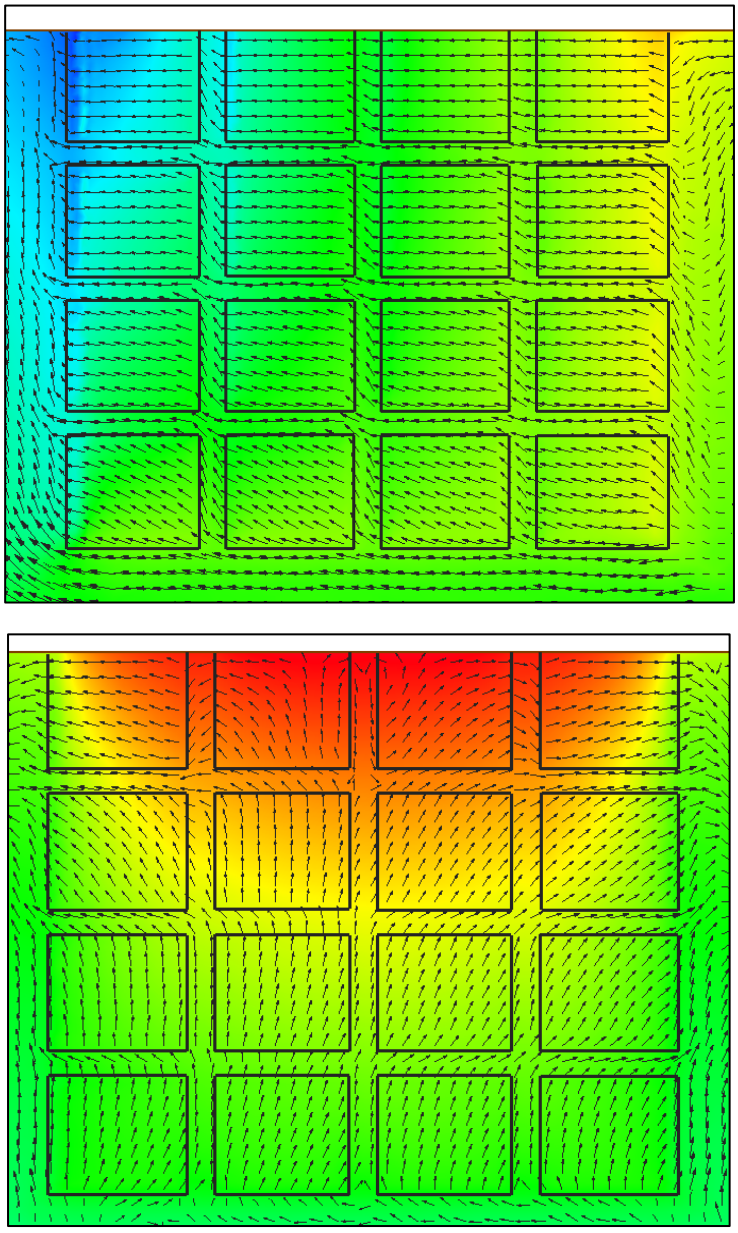

Figure 37. Instantaneous water surface elevation and velocity vectors for 2.5 h before (top) and 1.25 h after (bottom) hurricane landfall (Storm 1).

While storms of low surge potential induce an increase in coastal surge levels due to decreased marsh continuity, an opposite effect is associated with the storms of high surge potential. In these cases, surge is decreased at the coast by as much as 5% in the case of c = 50% continuity for the storm of highest surge potential (ζ_{base} = 6.0 m). This is a result of increased conveyance within the marsh allowing an outflow of surge waters from the marsh during times of peak surge. Nevertheless, increases in peak surge are still noted within the marsh due to channeling from the seaward to central areas of the marsh.

The relationship between marsh continuity and volume of surge (total volume of water stored within the marsh due to peak water levels) within the marsh is depicted in Figure 38. A drastic increase in surge volume is noted for the storm of lowest surge potential. However, with increasing surge potential, it becomes evident that marsh continuity has a much more slight effect on surge volume. Given the storm of highest surge potential (purple line in Figure 38), surge volume within the marsh is decreased with decreasing marsh continuity, indicating an outward flow dominating at times of peak surge.

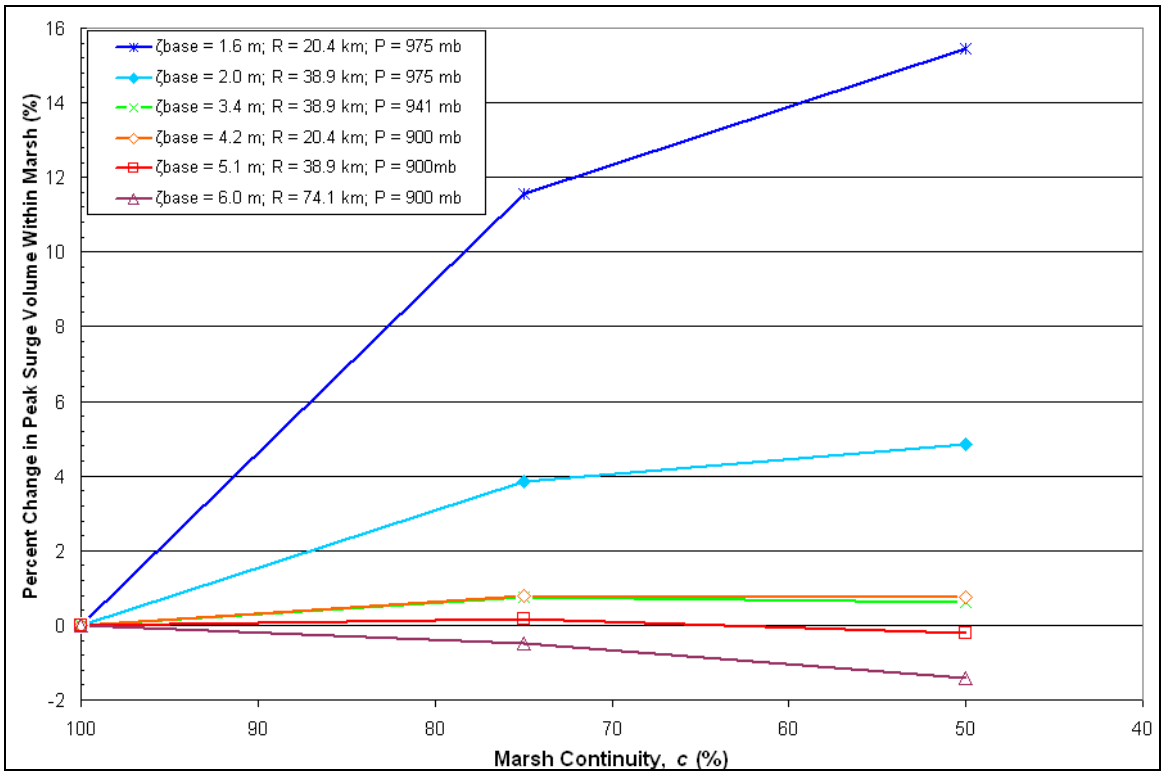

Figure 38. Changes in peak surge volume within the marsh due to decreased marsh continuity.

A similar effect is noted for coastal peak changes in surge due to decreased marsh continuity. As presented in Figure 39, peak surge at the coast is substantially increased with decreasing marsh continuity for the low potential storms (as indicated by the blue and cyan lines). However, as surge potential increases, increases in surge at the coastline due to decreased marsh continuity become more subtle, transitioning to a decrease in peak surge for the storms of high surge potential (red and purple lines). This suggests that for storms of greater surge potential, a non-continuous marsh may provide a level of storm protection comparable to that of a fully continuous marsh.

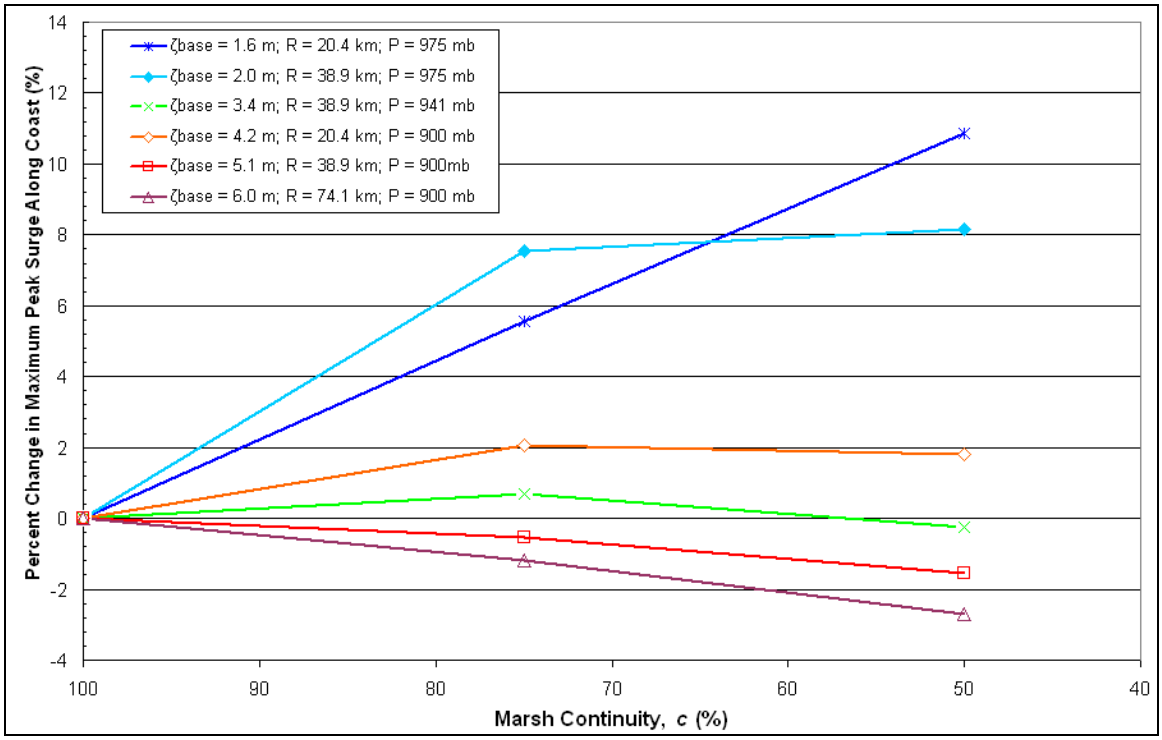

Figure 39. Coastal surge response to decreased marsh continuity.

As done for the results investigating the effects of marsh bottom friction and elevation, data by *Irish et al*. (2008) is used to determine an equation for use in predicting surge over the 20km by 20km non-continuous marsh based on storm parameters and continuity. Figure 40 presents a best-fit relation that approximates the *M* parameter based on continuity. Solving this equation yields the following relationship for peak water depth based on storm parameters and marsh continuity:

$$h = 3.508e^{-0.006c}(m_s R_p + b_y)\Delta p \tag{4.6}$$

The accuracy of this relationship is illustrated in Figure 41, with an R^2 of 0.93 and a root mean square error of 0.8 m.

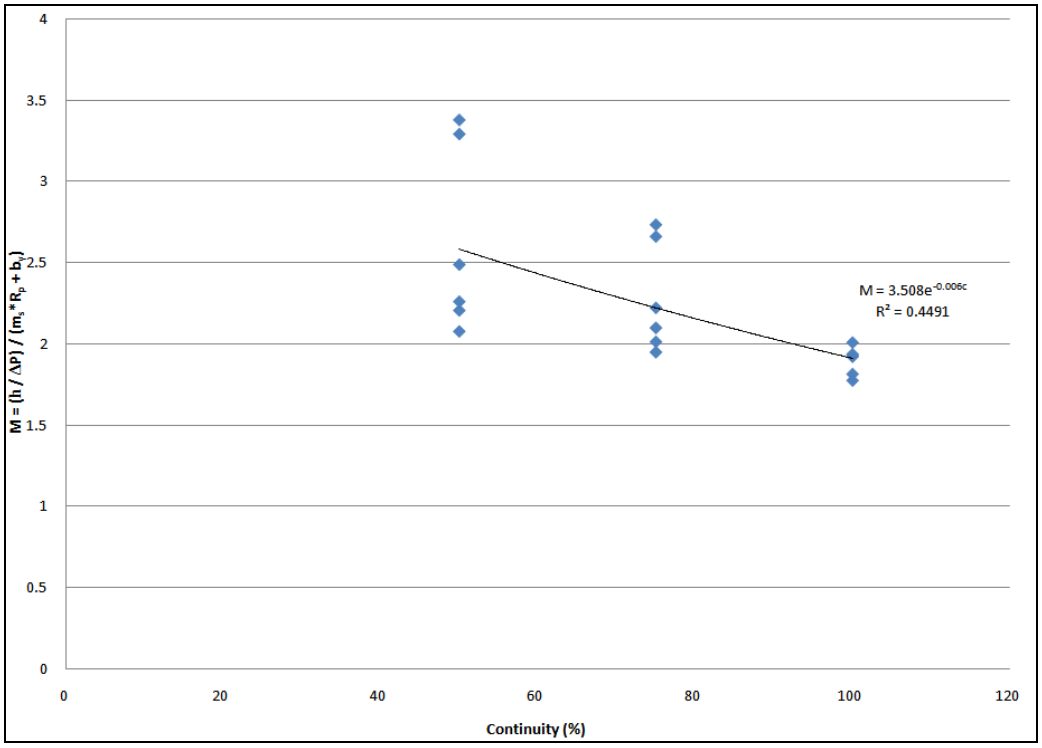

Figure 40. Relationship between *M* and continuity (*c*), with exponential best fit equation.

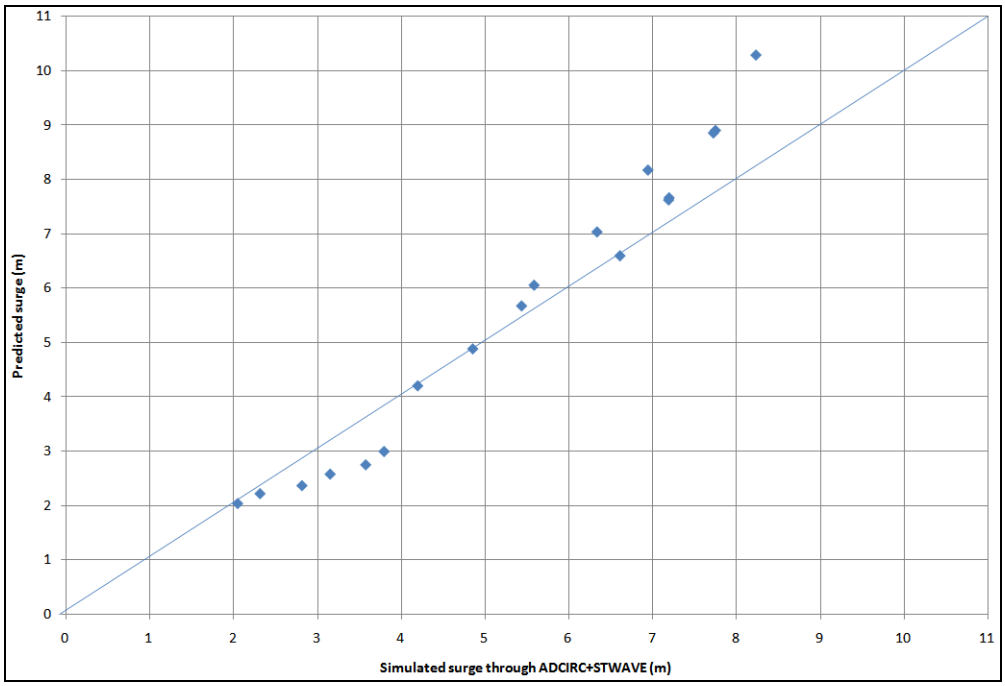

Figure 41. Predicted values of peak water depth based on Equation 4.6 as compared with peak water depth observed through ADCIRC.

4.5 Conclusions

Presented in this section are results based on ADCIRC and STWAVE results investigating wave and surge sensitivity to bottom friction (approximating vegetation), seabed elevation, and continuity of a 20 km by 20 km coastal wetland feature. Percent difference and numeric difference plots provide an illustration of the wetland characteristics' impacts on wave and surge, while relationships based on the Ursell parameter provide a basis for predicting wave height given incident wave characteristics, depth, and bottom friction (Manning's *n*). The empirical formulation predicting wave height are compared against STWAVE simulation results, featuring an R^2 of 0.93 and root mean square error of 0.26 m. Relationships based on findings *Irish et al*. (2008) provide an empirical formulation for predicting storm surge depths given meteorological parameters and wetland characteristics. Each predicted formulation calculated and compared with ADCIRC results. For the empirical relationships predicting peak surge depth, R^2 values range from 0.93 to 0.96, and root mean square errors range from 0.3 to 1.4 m.

5. SUMMARY AND CONCLUSIONS

Computations provided by the ADCIRC and STWAVE numerical models indicate that, given a 20 km by 20 km area of idealized marsh, properties of bottom friction, elevation, and marsh continuity have a definite and wide-ranging effect on peak surge levels and wave heights. Increased bottom friction results in significant decreases in storm surge levels, particularly for weak storms that produce low to moderate levels of storm surge (less than 2.0 m of peak surge). Surge reductions are less pronounced for storms of larger surge potential. Wave heights are similarly dampened by bottom roughness. The lowering of marsh elevation generally induces a decrease in surge levels due to the inversely proportional relationship between surge and total depth. Conversely, decreased marsh elevation results in an increase in peak significant wave height, due to the fact that waves are limited in height by total depth. The segmentation, or reduction of marsh continuity, results in increased coastal surge levels for low to moderate surge potential events, and slight decreases in surge for high surge potential effects. This suggests that a comparable degree of surge protection may be provided by both a continuous and non-continuous marsh, given a hurricane producing extreme amounts of surge. Wave heights are generally increased due to decreased marsh continuity, primarily resulting from wave propagation through marsh channels. However, due to effects of wave refraction, average wave heights within a non-continuous marsh are not increased until the marsh is significantly segmented, at 50% continuity.

Given the need to both restore wetlands and protect increasingly populated areas from hurricane damage, a greater body of research is needed to understand the true capabilities of coastal wetlands for providing protection from storm damage. Topics of recommended future research include:

- Laboratory modeling of artificial and actual wetland vegetation to better understand vegetated flow dynamics and wave damping due to vegetative drag
- Evaluation of the validity of the Manning's *n* value, among other bottom friction coefficients in terms of estimating flow through vegetation canopies
- Field measurements of storm surge and wave dynamics through marsh vegetation
- Use of computational fluid dynamics models to estimate the interactions between wind induced water velocities and flexible vegetation

With increased tax revenues (totaling $1 billion per year) from the Gulf of Mexico Energy Security Act of 2006 going directly to coastal restoration and protection in Louisiana, it is of paramount importance that funding be applied in the most efficient way possible to provide a sustainable storm protection solution. It is the hope of the author that this thesis will reveal general, quantitative relationships between surge and wave response and physical marsh characteristics, ultimately providing information that may be used to optimize a restoration plan within the Mississippi Delta region and other coastal regions in the US in terms of storm protection. Furthermore, while this work

focuses on hurricane impacts, results may also be extended to broader applications, such as surge and wave impacts of extratropical storms. The idealized nature of the modeling domain used in this study provides a basis for applying results to many coastal locations worldwide.

REFERENCES

Akan, A.O. (2006), *Open Channel Hydraulics*, Elsevier Ltd, New York.

Asano, T., Deguchi, H., and N. Kobayashi (1992), Interaction between water waves and vegetation, *Proceedings of the International Conference of Coastal Engineering, 1992*, *3*, 2710-2723.

Asano, T., S. Tsutsui, and T. Sakai (1988), Wave damping characteristics due to seaweed, *Proceedings of the 35th Coastal Engineering Conference in Japan*, 138-142.

Augustin, L.N., Irish, J.L., and P.L. Lynett (in press), Laboratory and numerical studies of wave damping by emergent and near-emergent wetland vegetation, *Coastal Engineering*, accepted September 2008.

Barras, J.A. (2006), Land area changes in coastal Louisiana after the 2005 hurricanes, US Geological Survey, 25 August 2008, <http://www.nwrc.usgs.gov/hurricane/landchange2005/CWPPRA_hurricanepres_10-18-06_vid_final.pdf>

Baustian, J.J., and R.E. Turner (2006), Retoration success of backfilling canals in coastal Louisiana marshes, *Restoration Ecology*, *14*(4), 636-644.

Boyer, M.E. (1997), The effect of long-term marsh management on land-loss rates in coastal Louisiana, *Environmental Management*, *21*(1), 97-104.

Cahoon, D.R., Hensel, P.F., Spencer, T., Reed, D.J., McKee, K.L., and N. Saintilan (2006), Coastal wetland vulnerability to relative sea-level rise: wetland elevation trends and process controls, *Ecological Studies*, *190*, 271-291.

Cardone, V.J., Greenwood, C.V., and J.A. Greenwood (1992), Unified program for the specification of hurricane boundary layer winds over surfaces of specified roughness, Contract Report CERC-92-1, US Army Corps of Engineers, Vicksburg, MS.

Choi, Y., and Y. Wang (2004), Dynamics of carbon sequestration in a coastal wetland using radiocarbon measurements, *Global Biogeochemical Cycles*, *18*(4), 1-12.

Chow, V.T. (1959), *Open Channel Hydraulics*, McGraw-Hill Book Co, New York.

Dalyrmple, R.A., Kirby, J.T., and P.A. Hwang (1984), Wave refraction due to areas of energy dissipation, *Journal of Waterways, Port, Coastal, and Ocean Engineering*, *110*(1), 67-79.

Danard, M.B., and T.S. Murty (1994), Storm surge mitigation through vegetation canopies (1994), *Natural Hazards, 9*, 155-166.

Day, J.W., Britsch, L.D., Hawes, S.R., Shaffer, G.P., Reed, D.J., and D. Cahoon (2000), Pattern and process of land loss in the Mississippi delta: a spatial and temporal analysis of wetland habitat change, *Estuaries*, *23*(4), 425-438.

Day, J.W., Barras, J., Clairain, E., Johnston, J., Justic, D., Kemp, G.P., Ko, J., Lane, R., Mitsch, W.J., Steyer, G., Templet, P., and A. Yañez-Arancibia (2005), Implications of global climatic change and energy cost and availability for the restoration of the Mississippi delta, *Ecological Engineering*, *24*, 253-265.

Day, J.W., Boesch, D.F., Clairain, E.J., Kemp, P.G., Laska, S.B., Mitsch, W.J., Orth, K., Mashriqui, H., Reed, D.J., Shabman, L., Simenstand, C.A., Streever, B.J., Twilley, R.R., Watson, C.C., Wells, J.T., Whigham, D.F. (2007), Restoration of the Mississippi delta: lessons from Hurricanes Katrina and Rita, *Science*, *315*, 1679-1684.

Dean, R.G. (1978), Effects of vegetation on shoreline erosional processes, *Proceedings of the National Symposium on Wetlands, Lake Buena Vista, FL, 1978,* American Water Resources Association, Minneapolis, MN, 415-426.

Dean, R.G., and R.A. Dalyrmple (2002), *Coastal Processes with Engineering Applications*, Cambridge University Press, Cambridge.

Dean, R.G., and C.J. Bender (2006), Static wave setup with emphasis on damping effects by vegetation and bottom friction, *Coastal Engineering*, *53*, 149-156.

Donnelly, J.P., and M.D. Bertness (2001), Rapid shoreward encroachment of salt marsh cordgrass in response to accelerated sea-level rise, *Proceedings of the National Academy of Sciences of the USA*, *98*(25), 14218-14223.

Dubi, A., and A. Torum (1995), Wave damping by kelp vegetation, *Proceedings of the 24th Coastal Engineering Conference*, ASCE, 142-156.

Ebersole, B.A., Resio, D.T., and J.J. Westerink (2007), A community approach to improved prediction and characterization of coastal storm hazards, *Marine Technology Society Journal*, *40*(4), 56-68.

Edwards, K.R., and C.E. Proffitt (2003), Comparison of wetland structural characteristics between created and natural salt marshes in southwest Louisiana, USA, *Wetlands*, *23*(2), 344-356.

FEMA (2008), FEMA: most expensive presidentially-declared disasters, 25 August 2008, <http://www.fema.gov/media/top_disasters.shtm>.

Fritz, H.M., Blount, C., Sokoloski, R., Singleton, J., Fuggle, A., McAdoo, B.G., Moore, A., Grass, C., and T. Banks (2008), Hurricane Katrina storm surge reconnaissance, *Journal of Geotechnical and Geoenvironmental Engineering*, ASCE, *134*(5), 644-656.

Garratt, J.R. (1977), Review of drag coefficients over oceans and continents, *Monthly Weather Review*, *105*, 915-929.

Green, J.C. (2005), Modelling flow resistance in vegetated streams: review and development of new theory, *Hydrological Processes*, *19*, 1245-1259.

Guidroz, W.S., Stone, G.W., and D. Dartez (2006), Hurricane Rita, 2005: assessment of a storm-induced geological event along the southwestern Louisiana coast and adjacent interior marsh, *Gulf Coast Association of Geological Sciences Transactions*, *56*, 229-239.

Hackney, C.T., and T.D. Bishop (1981), A note on the relocation of marsh debris during a storm surge, *Estuarine, Coastal, and Shelf Science*, *12*, 621-624.

Holthuijsen, L.H., Booij, N., and R.C. Ris (1993), A spectral wave model for the coastal zone, *Proceedings of the 2nd International Symposium on Ocean Wave Measurement and Analysis*, 630-641.

Hosokawa, Y., and K. Furukawa (1994), Surface flow and particle settling in a coastal reed field, *Water Science Technology, 29*(4), 45-53.

Houck, O. (2006), Can we save New Orleans?, *Tulane Environmental Law Journal 19*(1), 25 August 2008, <http://kerrn.org/pdf/Houck_CanWeSaveNewOrleans.pdf>.

Irish, J.L., Resio, D.T., and J.J. Ratcliff (2008), The influence of storm size on hurricane surge, *Journal of Physical Oceanography*, *38*(9), 2003-2013.

Jelesnianski, C.P., J. Chen, and W.A. Shaffer (1992), SLOSH: Sea, lake, and overland surges from hurricanes. NOAA Technical Report, NWS 48.

Jensen, R.E., personal communication, Research Hydraulic Engineer, US Army Research and Development Center, Vicksburg, MS, 29 February 2008.

Kadlec, R.H. (1990), Overland flow in wetlands: vegetation resistance, *Journal of Hydraulic Engineering, 116*(5), 691-706

Kazmierczak, R.F. (2001), *Economic Linkages Between Coastal Wetlands and Water Quality: A Review of Value Estimates Reported in the Published Literature*, Natural Resource and Environment Committee, Louisiana State University Agricultural Economics and Agribusiness, Baton Rouge, LA.

Knabb, R.D., Rhome, J.R., and D.P. Brown (2005), *Tropical Cyclone Report: Hurricane Katrina, 23-30 August 2005*, National Hurricane Center, Miami FL.

Kobayashi, N., Raichle, A.W., and T. Asano (1993), Wave attenuation by vegetation, *Journal of Waterway, Port, Coastal, and Ocean Engineering*, *119*(1), 30-48.

Kouwen, N., Li, R., and D.B. Simons (1981), Flow resistance in vegetated waterways, *American Society of Agricultural Engineers*, *81*, 685-690.

LaSalle, M.W. (2008), Recognizing wetlands in the Gulf of Mexico region, *Mississippi State University Extension Service*, 14 September 2008, <http://msucares.com/pubs/publications/p2157.html>.

Laska, S., Wooddell, G., Hagelmann, R., Gramling, R., and M.T. Farris (2005), At risk: the human, community, and infrastructure resources of coastal Louisiana, *Journal of Coastal Research*, *SI*(44), 90-111.

Louisiana Coastal Wetlands Conservation and Restoration Task Force and the Wetlands Conservation and Restoration Authority (1998), Coast 2050: toward a sustainable coastal Louisiana, Louisiana Department of Natural Resources, Baton Rouge, LA.

Luettich, R.A., and J.J. Westerink (1999), Elemental wetting and drying in the ADCIRC hydrodynamic model: upgrades and documentation for ADCIRC Version 34.xx, Contractors Report, Department of the Army, Us Army Corps of Engineers, Coastal Engineering Research Center, Waterways Experiment Station, Vicksburg, MS, 8 p.

Luettich, R., and J. Westerink (2004), Formulation and numerical implementation of the 2D/3D ADCIRC finite element model version 44.XX, 25 Aug 2008, <http://adcirc.org/adcirc_theory_2004_12_08.pdf>.

Martínez, M.L., Intralawan, A., Vázquez, G., Pérez-Maqueo, O., Sutton, P., and R. Landgrave (2007), The coasts of our world: ecological, economic and social importance, *Ecological Economics*, *63*, 254-272.

Mattocks, C., and C. Forbes (2008), A real-time, event-triggered storm surge forecasting system for the state of North Carolina, *Ocean Modeling* (in press).

Mendez, F.G., Losada, I.J., and M.A. Losada (1999), Hydrodynamics induced by wind waves in a vegetation field, *Journal of Geophysical Research*, *104*(C8), 18383-18396.

Miche, M. (1944), Breaking wave motion in water of constant depth, *Ann. Ponts et Chaussees*, *121*, 285-318.

Morton, R.A., Tiling, G., and N.F. Ferina (2003), Causes of hot-spot wetland loss in the Mississippi delta plain, *Environmental Geosciences*, *10*(2), 71-80.

Morton, R.A., Bernier, J.C., and J.A. Barras (2006), Evidence of regional subsidence and associated interior wetland loss induced by hydrocarbon production, Gulf Coast region, USA, *Environmental Geology*, *50*, 261-274.

Neill, C., and R.E. Turner (1987), Backfilling canals to mitigate wetland dredging in Louisiana coastal marshes, *Environmental Management*, *11*(6), 823-836.

Otten, C.J., Bakker, P., and M. Meijer (2006), Reduction of hurricane impact by re-creation of marshlands and barrier islands, *Terra et Aqua*, *105*, 20-31.

Peterson, C.H., Luettich, R.A., Fiorenza, M., and G.A. Skilleter (2004), Attenuation of water flow inside seagrass canopies of differing structure, *Marine Ecology Progress Series*, *268*, 81-92.

Potter, S. (2004), September 8, 1900 (Retrospect), *Weatherwise Sep/Oct 2004*, *57*(5), 20-21.

Reed, S.C. (1991), Constructed wetlands for wastewater treatment, *Biocycle*, *32*, 44-49.

Reid, R.O., and R.E. Whitaker (1976), Wind-driven flow of water influenced by a canopy, *Journal of the Waterways Harbors and Coastal Engineering Division, WW1*, 61-77.

Resio, D. T.., and J.J. Westerink (2008), Modeling the physics of storm surges, *Physics Today*, September 2008, 33-38.

Ris, R.C., and L.H. Holthuijsen (1997), Modeling of current induced wave-blocking in a spectral wave model, *8th International Biennial Conference on Physics of Estuaries and Coastal Seas*, J. Dronkers and M. Scheffers (eds.), 139-144.

Rodgers, J.H., and J.W. Castle (2008), Constructed wetland systems for efficient and effective treatment of contaminated waters for reuse, *Environmental Geosciences*, *15*(1), 1-8.

Rozas, L.P., Caldwell, P., and T.J. Minello (2005), The fishery value of salt marsh restoration projects, *Journal of Coastal Research*, *SI*(40), 37-50.

SMS - Surface Water Modeling System (2002), Surface water modeling system, tutorials version 8.0, Brigham Young University, Environmental Modeling Research Laboratory, Provo, UT.

Smith, J., Sherlock, A., and D. Resio (2001), STWAVE: Steady-State Spectral Wave Model User's Manual for STWAVE, Version 3.0, US Army Corps of Engineers Engineer Research and Development Center, Vicksburg, MS.

Solomon, S., D. Qin, M. Manning, R.B. Alley, T. Berntsen, N.L. Bindoff, Z. Chen, A. Chidthaisong, J.M. Gregory, G.C. Hegerl, M. Heimann, B. Hewitson, B.J. Hoskins, F. Joos, J. Jouzel, V. Krattsov, U. Lohmann, T. Matsuno, M. Molina, N. Nicholls, J. Overpeck, G. Raga, V. Ramaswamy, J. Ren, M. Rusticucci, R. Somerville, T.F. Stocker, P. Whetton, R.A. Wood, and D. Wratt (2007), Technical Summary, *Climate Change 2007: The Physical Science Basis, Contribution of Working Group I to the Fourth Assessment Report of the Intergovernmental Panel on Climate Change*, Cambridge University Press, Cambridge.

Streever, W.J. (2000), Spartina alterniflora marhes on dredged material: a critical review of the ongoing debate over success, *Wetland Ecology and Management, 8*, 295-316.

Stone, G.W., Grymes, J.M., Dingler, J.R., and D.A. Pepper (1997), Overview and significance of hurricanes on the Louisiana Coast, USA, *Journal of Coastal Research*, 13(3), 656-669.

Svendsen, I.A. (2006), *Introduction to Nearshore Hydrodynamics*, World Scientific, Hackensack, NJ.

Tanner, R. (2005), Katrina joins deadliest list, *The Advertiser*, 16 September 2005, 30-31.

Thomas, H., and T.R. Nisbet (2007), An assessment of the impact of floodplain woodland on flood flows, *Water and Environment Journal, 21*, 114-126.

Thompson, E.F., and V.J. Cardone (1996), Practical modeling of hurricane surface wind fields, *Journal of Waterways, Port, and Coastal Engineering*, *122*, 195-205.

Tickner, E.G. (1957), Effect of bottom roughness on wind tide in shallow water, *Technical Memorandum 95*, Beach Erosion Board, US Army Corps of Engineers.

Turner, R.E. (1990), Landscape development and coastal wetland losses in the northern Gulf of Mexico, *American Zoologist, 30*(1), 89-105.

USACE (1961), Interim survey report: Mississippi River delta at and below New Orleans, Louisiana, US Army Corps of Engineers New Orleans District, New Orleans, LA.

US Department of Agriculture (2008), Plant fact sheet: smooth cordgrass, 25 Aug 2008, <http://plants.usda.gov/factsheet/pdf/fs_spal.pdf>.

US Environmental Protection Agency (1987), Saving Louisiana's coastal wetlands: the need for long-term plan of action, EPA #230-02-87-026, 3-28.

US Environmental Protection Agency (a), America's Wetlands: Our Vital Link Between Land and Water, 25 August 2008, <http://www.epa.gov/OWOW/wetlands/vital/toc.html>.

US Environmental Protection Agency (b), Future Climate Change – Future Sea Level Changes, 13 September 2008, <http://epa.gov/climatechange/science/futureslc.html>.

US Geological Survey (2006), USGS Reports Latest Land-water Changes for Southeastern Louisiana, 25 August 2008, <http://www.nwrc.usgs.gov/hurricane/Land%20Water%20Changes%20for%20SE%20LA.pdf>.

US National Oceanic and Atmospheric Administration (2008), Storm surge: a 'rising' concern among coastal residents, *NOAA Magazine Online*, 13 September 2008, <http://www.magazine.noaa.gov/stories/mag178.htm>.

Walton, R., and B.A. Christensen (1980), Friction factors in storm surges over inland areas, *ASCE Journal of the Waterway, Port, Coastal, and Ocean Division*, *106*(WW2), 261-271.

WAMDI Group (1988), The WAM Model – A third generation ocean wave prediction model, *Journal of Physical Oceanography*, *18*, 1775-1810.

Westerink, J.J., Luettich, R.A., Feyen, J.C., Atkinson, J.H., Dawson, C., Roberts, H.J., Powell, M.D., Dunion, J.P., Kubatko, E.J., and H. Pourtaheri (2008), A basin- to channel-scale unstructured grid hurricane storm surge model applied to southern Louisiana, *Monthly Weather Review*, *136*, 833-864.

Zhang, K., Xiao, C., and J. Shen (2008), Comparison of the CEST and SLOSH Models for storm surge flooding, *Journal of Coastal Research*, *24*(2), 489-499.

VITA

Name:	Nicholas Mason Loder
Email Address:	nick.loder@gmail.com
Education:	B.S., Civil Engineering, Clemson University, 2006 M.S., Civil Engineering, Texas A&M University, 2008
Mailing Address:	3136 TAMU College Station, TX 77843-3136